



HUNGARIAN UNIVERSITY OF AGRICULTURE AND LIFE SCIENCES

# Performance analysis of a parabolic trough solar collector

PhD Dissertation

by

Asaad Yasseen Al-Rabeeah

Gödöllő

2023

**Doctoral school**

**Denomination:** Doctoral School of Mechanical Engineering

**Science:** Mechanical Engineering

**Leader:** Prof. Dr. Gábor Kalácska, DSc  
Institute of Technology  
Hungarian University of Agriculture and Life Science, Gödöllő,  
Hungary

**Supervisor:** Prof. Dr. István Farkas, DSc  
Institute of Technology  
Hungarian University of Agriculture and Life Science, Gödöllő,  
Hungary

**Co-Supervisor:** Dr. István Seres, PhD  
Institute of Mathematics and Basic Science  
Hungarian University of Agriculture and Life Science, Gödöllő,  
Hungary

.....  
Affirmation of supervisor

.....  
Affirmation of head of school

## CONTENTS

NOMENCLATURE AND ABBREVIATIONS.....	6
1. INTRODUCTION, OBJECTIVES .....	9
1.1. Introduction .....	9
1.2. Objectives.....	10
2. LITERATURE REVIEW.....	11
2.1. General overview of parabolic trough solar collector system.....	11
2.1.1. <i>Background of parabolic trough solar collector system</i> .....	11
2.1.2. <i>Parabolic trough solar collector systems fundamentals</i> .....	11
2.1.3. <i>Modelling and simulation of parabolic trough solar collector</i> .....	12
2.2. Optical analysis of parabolic trough solar collector system.....	13
2.2.1. <i>Optical analysis of errors</i> .....	15
2.2.2. <i>Ray tracing</i> .....	16
2.3. Heat transfer element for parabolic trough solar collector.....	17
2.4. Enhancement of optical efficiency .....	18
2.4.1. <i>Selective surface coating on the receiver tube</i> .....	18
2.4.1.1. Methods for preparing selective coating.....	19
2.4.1.2. Comparison of data for selective absorber coatings .....	19
2.4.1.3. Thermal stability and lifetime of selective absorber coatings .....	22
2.4.2. <i>Reflective surface</i> .....	23
2.4.3. <i>Absorber tube intercept factor</i> .....	24
2.4.4. <i>Antireflective surface coating on the glass tube</i> .....	24
2.4.5. <i>Incorporating secondary reflectors</i> .....	24
2.4.6. <i>Dual axis tracking and end losses</i> .....	24
2.5. Performance enhancement techniques .....	24
2.5.1. <i>Parabolic trough solar collector receiver with glass envelope</i> .....	25
2.5.2. <i>Passive heat transfer enhancement</i> .....	25
2.5.3. <i>Nanofluid</i> .....	28
2.5.3.1. Mono nanofluids .....	29
2.5.3.2. Hybrid nanofluid.....	32
2.6. Computational fluid dynamics analysis .....	32
2.7. Summary of literature review.....	34
3. MATERIALS AND METHODS.....	35

3.1. Description and experimental set up .....	35
3.1.1. <i>Geometry of parabolic trough solar collector</i> .....	36
3.1.2. <i>Thermal modelling</i> .....	37
3.1.3. <i>Optical modelling</i> .....	38
3.1.4. <i>Heat transfer analysis</i> .....	39
3.2. The components of parabolic trough solar collector system .....	39
3.2.1. <i>Reflector surface</i> .....	40
3.2.2. <i>Absorber tube</i> .....	41
3.2.2.1. Single evacuated absorber tube .....	41
3.2.2.2. Double evacuated absorber tube .....	41
3.2.2.3. Loop evacuated absorber tubes .....	42
3.2.2.4. Double evacuated absorber tube with flat plate .....	42
3.2.3. <i>Glass receiver</i> .....	43
3.2.3.1. Evacuated glass tube .....	43
3.2.3.2. The single glass tube .....	44
3.2.4. <i>Structure of support</i> .....	44
3.2.5. <i>Storage tank</i> .....	45
3.2.6. <i>Silicone pipes</i> .....	45
3.2.7. <i>Solar tracking mechanism</i> .....	45
3.2.8. <i>Cooling system</i> .....	46
3.2.9. <i>Measuring devices</i> .....	46
3.2.9.1. The pyrometer .....	47
3.2.9.2. LUTRON BTM-4208SD data logger .....	47
3.2.9.3. Mass flow rate .....	47
3.2.9.4. Thermocouples .....	47
3.3. Experimental uncertainty analysis .....	48
3.4. Preparations of hybrid nanofluids .....	48
3.4.1. <i>Effect of temperature on thermal conductivity</i> .....	50
3.4.2. <i>Effect of temperature on viscosity</i> .....	52
3.4.3. <i>Measurement of the density and the specific heat</i> .....	54
3.5. Preparations of graphene nanofluids .....	54
3.5.1. <i>Effect of temperature on thermal conductivity</i> .....	55
3.5.2. <i>Effect of temperature on viscosity</i> .....	57
3.5.3. <i>Measurement of the density and the specific Heat</i> .....	58
3.6. Preparing nanocoating .....	59

3.7. Numerical analysis .....	59
3.7.1 Assumptions .....	60
3.7.2. Governing equations.....	60
3.7.3. The receiver tube geometry.....	61
3.7.4. Mesh generation .....	61
3.7.5. Boundary conditions.....	62
3.7.6. Methodology .....	62
3.7.7 Grid independent study.....	62
3.7.8. Model validation.....	63
3.8. Experimental procedure .....	64
4. RESULTS .....	67
4.1. Similarity tests of each collector .....	67
4.2. Effect of reflective surface on parabolic trough solar collector performance.....	67
4.3. Effect of receiver tube coating on parabolic trough solar collector performance.....	71
4.4. Test case hybrid nanofluid .....	75
4.5. Test case graphene nanofluid .....	81
4.6. The receiver geometry.....	87
4.7. New scientific results .....	93
5. CONCLUSIONS AND SUGGESTIONS .....	96
6. SUMMARY .....	97
7. ÖSSZEFOGLALÁS (SUMMARY IN HUNGARIAN).....	98
8. APPENDICES.....	99
A1: Bibliography.....	99
A2: Publications related to the dissertation.....	112
9. ACKNOWLEDGEMENTS .....	114

## NOMENCLATURE AND ABBREVIATIONS

$A_a$	Aperture area of the collector ( $\text{m}^2$ )
$A_{ri}$	Inlet area of the receive tube ( $\text{m}^2$ )
$A_{ro}$	Outer area of the receive tube ( $\text{m}^2$ )
$A_{co}$	Outer cover area ( $\text{m}^2$ )
$C$	Concentration ratio
$cp$	Specific heat capacity ( $\text{kJ kg}^{-1} \text{K}^{-1}$ )
$D_{ri}$	Inner diameter of the receiver tube (m)
$D_{ro}$	Outer diameter of the receiver tube (m)
$D_{ci}$	Inner diameter of the cover tube (m)
$D_{co}$	Outer diameter of the cover tube (m)
$f$	Collector focal distance, m
$h_{out}$	Cover to ambient heat transfer coefficient ( $\text{W m}^{-2} \text{K}^{-1}$ )
$I_b$	Direct beam radiation ( $\text{W m}^{-2}$ )
$K$	Incidence angle, ( $^\circ$ )
$k$	Thermal conductivity ( $\text{W m}^{-1} \text{ }^\circ\text{C}^{-1}$ )
$k_{eff}$	Effective thermal conductivity ( $\text{W m}^{-1} \text{ }^\circ\text{C}^{-1}$ )
$L$	Collector width (m)
$m$	Mass (kg)
$\dot{m}$	Mass flow rate ( $\text{kg s}^{-1}$ )
$Nu$	Nusselt number
$Pr$	Prandtl number
$Q_{loss}$	Thermal losses of the absorber (W)
$Q_s$	Solar radiation intensity on the PTSC aperture ( $\text{W m}^{-2}$ )
$Q_u$	Useful heat power (W)
$Q_{abs}$	Absorbed thermal power (W)
$Q_{conv}$	Convection heat power transfer (W)
$Q_{rad}$	Radiation heat power transfer (W)
$r_r$	Rim radius (m)
$Re$	Reynolds number
$T_{out}$	Outlet temperature of the heat transfer fluid ( $^\circ\text{C}$ )
$T_{in}$	Inlet temperature of the heat transfer fluid ( $^\circ\text{C}$ )
$T_{sky}$	Sky temperature ( $^\circ\text{C}$ )
$T_{ci}$	Inner cover temperature ( $^\circ\text{C}$ )
$T_{ro}$	Outer receiver temperature ( $^\circ\text{C}$ )
$T_{rm}$	Mean temperature of receiver ( $^\circ\text{C}$ )
$T_c$	Cover temperature ( $^\circ\text{C}$ )
$T_{amb}$	Ambient temperature ( $^\circ\text{C}$ )
$T_{htf}$	Temperature of heat transfer fluid, ( $^\circ\text{C}$ )
$T_{ri}$	Inner receiver temperature ( $^\circ\text{C}$ )
$T^*$	heat loss parameter ( $\text{W m}^{-2} \text{ }^\circ\text{C}$ )
$U_L$	Thermal loss coefficient ( $\text{W m}^{-2} \text{K}^{-1}$ )

$V_{wind}$	Ambient air velocity ( $\text{m s}^{-1}$ )
$W$	Collector width (m)
$x$	Coordinate in x -axis (m)
$y$	Coordinate in y -axis (m)

*Greek symbols*

$\Phi_r$	Rim angle, ( $^\circ$ )
$\eta_{th}$	Thermal efficiency
$\sigma$	Stefan Boltzmann constant ( $\text{W m}^{-2} \text{K}^{-4}$ )
$\varepsilon_r$	Receiver emittance
$\varepsilon_c$	Cover emittance
$\eta_o$	Optical efficiency of the collector
$\theta$	Angle of incidence of solar radiations ( $^\circ$ )
$\eta_{opt-max}$	Maximum optical efficiency
$\alpha$	Absorptivity
$\gamma$	Intercept factor
$\tau$	Transmissivity
$\rho$	Reflectivity; density ( $\text{kg m}^{-3}$ )
$\varphi$	Particle concentration (%)
$\mu$	Dynamic viscosity ( $\text{kg m}^{-1} \text{s}^{-1}$ )

*Subscripts*

$a$	Aperture
$amb$	Ambient
$b$	Beam radiation
$c$	Cover
$f$	Fluid
$htf$	Heat transfer fluid
$hnf$	Hybrid nanofluid
$in$	Inlet
$max$	Maximum
$nf$	Nanofluid
$opt$	Optical
$out$	Outlet
$p$	Particle
$ri$	Inner receiver
$r$	Local mirror radius
$ro$	Outer receiver
$s$	Solar
$th$	Thermal
$tot$	Total

*u* Useful

*Abbreviations*

AS	Aluminium sheet
CFD	Computational fluid dynamics
GA	Gum Arabic
HNFs	hybrid nanofluids
HCE	Heat collection element
MC	Matte coating
NC	Nano coating
NFs	Nanofluids
PTSC	Parabolic trough solar collector
TC	Thermal conductivity
TE	Thermal efficiency
TS	Thermal stability
VCs	Volume concentrations



## 1. INTRODUCTION, OBJECTIVES

The research work's background and significance, as well as the main research goals, are discussed in this chapter.

### 1.1. Introduction

Renewable energy sources have become important in recent years because of increasing CO<sub>2</sub> emissions (Al-Rabeeh et al., 2022a; Al-Rabeeh et al., 2022b). Therefore, fossil fuel consumption needs to be reduced because of the harm it causes to the environment, global warming, and climate change. Researchers are focusing on renewable sources such as wind, geothermal, and solar energy. Solar energy is one of the cleanest and most effective when compared with other sources (Al-Oran et al., 2022). Solar energy is used in a wide range of industrial applications, such as the production of hot water and electricity.

The parabolic trough solar collector (PTSC) technology is one of the most reliable technologies in the field of solar thermal (Jebasingh and Herbert, 2016). It is mainly used for power generation (e.g., generating steam, which needs high temperatures) and other technological purposes (Yilmaz et al., 2017; Sandá et al., 2019). The collectors receive direct solar radiation from the sun over a large surface and gather it to the focal point (Al-Rabeeh et al., 2021c). Specifically, PTSC can produce high temperatures (over 400 °C). To investigate the thermal performance of the PTSC, many experimental tests were implemented in keeping with the ASHRAE 93–1986 standard (Chafie et al., 2016). Several parameters have effects on PTSC performance, such as the mass flow rate of the working fluid, ambient temperature, and the incident angle of the solar radiation, which increase and decrease heat losses (Fernández-García et al., 2010).

The PTSC consists of a reflector surface in a parabolic shape that concentrates the solar radiation into a receiver tube that transports a working fluid. Geometric analysis is the most effective method for evaluating PTSCs' optical performance (Mills, 2004). So, thermal efficiency (TE) and radiation heat transfer on solar mirrors in PTSC have been topics of considerable interest. PTSC technologies use mirrors to focus radiation on converting solar energy into thermal energy (Noman et al., 2019). The reflecting surfaces are classified as aluminium or silvered reflectors based on their reflecting layer (Chandrika et al., 2021). Furthermore, how a surface material is deposited, made, and polished greatly affects how reflective it is. In addition, the absorber coating should remain stable structurally and chemically at operating temperature through the focusing of solar radiation (Abdulhamed et al., 2018; Zou et al., 2017). The most widely used selective coatings were cermets used in PTSC heat collection devices. At 400°C, these selective surfaces absorb 0.96 and emit 0.1 ratio of the incoming radiation (Khan and Kleine, 1977).

A fluid flowing inside the tube absorbs the heat energy generated from the focused solar radiation, raising its enthalpy and causing an increase in the temperature of the tube wall (Montesa et al., 2014; Fuqiang et al., 2017). In addition, the design should be accurate to increase thermal efficiency and the material with low weight, high mechanical strength, and high thermal conductivity (TC) is preferable (Wang et al., 2015). TC of the absorber tube material affects the performance of PTSCs by increasing the heat transfer between the working

fluid and the metal (Razmmand et al., 2019). A working fluid is an essential component for enhancing the efficiency of PTSCs. The mixing of nanoparticles with the working fluid is an effective method of increasing the collected thermal energy and the nanofluids' thermophysical properties, such as enthalpy, specific heat capacity, thermal conductivity and density (Akbarzadeh and Valipour, 2018). (Razmmand et al., 2019) used different nanoparticles (mainly made of aluminium, nickel, silver, gold, titanium dioxide, etc.) with water in different concentrations to improve the critical length of heat flux of a PTSC. It could raise the heat transfer coefficient and lead to enhance Thermal conductivity (Ghasemi and Ranjbar, 2017). The thermal efficiency of PTSC depends on the concentration of the volume fraction of nanoparticles in the base fluid.

Proper design and using nanofluid for optimization of heat flux distribution are key matters for enhancing performance of PTSC and improving economic advantages the entire system.

### 1.2. Objectives

According to a survey of the available literature, experimental and numerical work has addressed the effects of several parameters on the performance of the PTSC. To the best of our knowledge, there has been no experimental work on PTSC efficiency enhanced by the preparation and use of graphene- $\text{Fe}_3\text{O}_4$ /water hybrid nanofluids (HNFs) with different concentrations. In addition, silver chrome film is being used as a reflecting surface, as well as a new design of absorber tube. Furthermore, the study of adding graphene and  $\text{Fe}_3\text{O}_4$  nanoparticles to the selective coating. Based on the mentioned above, the lack of reliable experimental investigations for both theoretical and modelling studies is a major issue, the main objectives of the present work are to investigate the following:

- To experimentally determine the thermal conductivity of mono and hybrid nanofluids at different concentrations and temperatures.
- To experimentally study the effect of the viscosity of mono and hybrid nanofluids at different temperatures and concentrations.
- To study the effect of nanofluids as working fluids on the efficiency and operation of the PTSC system.
- To validate the ANSYS simulation models with experimental results that describing the heat and mass transfer processes of the PTSC system at traditional working fluids compared with mono and hybrid nanofluid.
- To experimental analysis and comparison of the efficiency of the PTSC under different receiver tubes and different mass flow rates.
- To study the different selective coatings to enhance PTSC performance.
- To study the effect of two different reflecting surfaces, one made of silver-chrome film and the other of aluminium to enhance the efficiency of the PTSC.

## 2. LITERATURE REVIEW

In this chapter, this study reviews new innovations and technologies on the PTSC and different modifications and assessment techniques applied to them to improve their effectiveness. The effectiveness of the PTSC by researchers has been thoroughly reviewed with regards to approaches, tools, and techniques employed. Recent advancements have been thoroughly investigated in this field. Furthermore, challenges and gaps in the literature were identified, which is considered the reason for initiating this research.

### 2.1. General overview of parabolic trough solar collector system

This section gives an overall look at how the PTSC system works, including its background, fundamentals, and modelling.

#### 2.1.1. Background of parabolic trough solar collector system

In 1883, Captain John Ericsson used a PTSC to work on solar-powered machines for irrigation. However, his experiment on solar engines did not advance to the prototype stage. The invention of the parabolic trough is essential. In 1912, a 45-kW power plant was built in Egypt. The system was composed of five solar collectors and was oriented north-south with a system of mechanical tracking (Abdelhady et al., 2014). The system generated steam that was used to operate water pumps for irrigation. The development of parabolic trough power occurred in the US in the 1970s and in Europe in the 1980s (Price et al., 2002).

PTSCs could produce high temperatures (above 400 °C) to produce industrial process heat. The development was sponsored or conducted by the Sandia National Laboratories in New Mexico. In 1981, the International Energy Agency developed a small solar power system in Tabernas, Spain. In 1982, Luz International Limited (Luz) advanced a parabolic trough collector. In 1985, Luz built eight power plants of PTSCs in California, US. Today, according to the database of the National Renewable Energy Laboratory, over 97 plants are at different stages of development of this parabolic trough-based technology. The design of these power plants is to produce electrical power from steam obtained from natural gases or solar fields. The parabolic trough power plants of Nevada Solar in the US produce 72 MW capacities, and the Martin Solar Plant Centre has 75 MW net capacities. The Andosol plant is the first parabolic trough power plant in Spain. Many plants in Spain have similar operational characteristics (e.g., Andosol with 50 MW and 7.5 h storage energy) and some are under construction (e.g. Vallesol 50 with 50 MW and 7.5 h storage energy) (Noor and Muneer, 2009). The scholars are still trying to improve and increase the parabolic trough power plants efficiency.

#### 2.1.2. Parabolic trough solar collector systems fundamentals

A PTSC system is a technology that concentrates solar energy in a focal line to convert it into thermal energy of the high-temperature medium. It can obtain temperatures of up to 400 °C, depending on the application (Tian and Zhao, 2013). The collector receives the direct solar radiation from the sun over a large surface and focuses on it. The PTSC has a curved reflector or a parabolic mirror for reflecting and concentrating the solar radiation onto specific point or a line.

The mirror is manufactured from different materials to reduce absorption losses, such as low iron glass or aluminium. Many factors are important in the production of collector mirrors; these factors include solar-weighted reflectivity, durability, abrading properties, and cost. The gluing, silvering, and protective coating processes are performed after bending the mirror (Behar et al., 2015). The heat collection element (HCE), also referred to as the receiver, is placed at the focal axis, as shown in Fig. 2.1. The heat transfer fluid circulates through the absorber (Price et al., 2002).

A fluid flowing inside the tube that absorbs the heat energy generated from the focused solar radiation raises its enthalpy and causes an increase in the temperature of the tube wall. PTCs can be used only in direct solar radiation in the collectors, which are not deviated by dust, fumes, or clouds. The absorber tube should be coated by a material of the antireflective layer to minimize the heat losses generated by radiation (Fernández-García et al., 2010). The effectiveness of the solar thermal collector is calculated by measuring the fluid temperature difference between the inlet and the outlet and by the flow rate of the working fluid (Menbari et al., 2017).

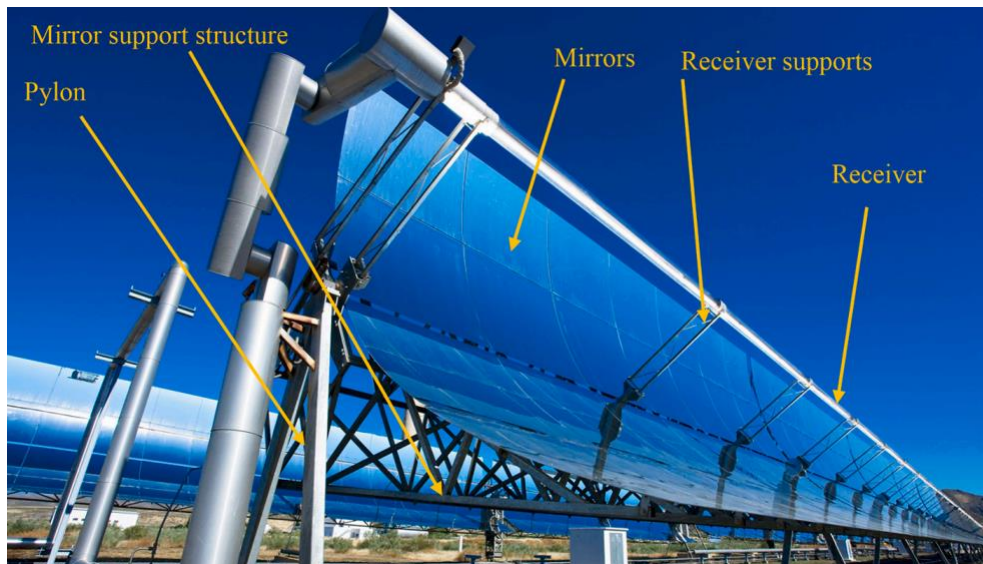


Fig. 2.1. PTSC structure and components (Malan and Kumar, 2021)

### 2.1.3. Modelling and simulation of parabolic trough solar collector

The progress of computing has helped researchers in analysing the system by modelling and simulation. Engineering programs can be used to study the system performance and the effect of several variables with minimum time and low cost (Bellos Korres et al., 2016). Recently, many modelling studies have been performed and have facilitated the development of PTSCs; these studies involved thermal and optical analyses through the modelling and simulation of PTSCs. By modelling the system, the factors can be analysed and handled separately (e.g., temperature and the properties of optical materials). Fig. 2.2 presents the modelling and simulation of PTSCs can be covered as depicted.



Fig. 2.2. Methodology pursued for modelling and simulation of PTSCs (Yılmaz and Mwesigye, 2018)

## 2.2. Optical analysis of parabolic trough solar collector system

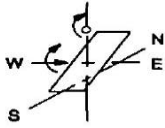
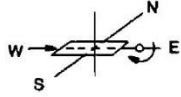
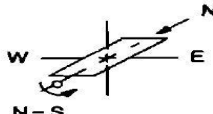
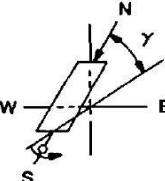
The optical efficiency ( $\eta_o$ ) can be got by the rate of energy absorbed from radiation in the absorber tube and the amount of the energy incident on the aperture of the collector:

$$\eta_o(\theta = 0) = \rho \tau \alpha \gamma, \quad (2.1)$$

where:  $\rho$  - the mirror reflectivity;  $\tau$  - the glass envelope transmittance;  $\alpha$  - the absorptivity of surface coating;  $\gamma$  - the mirror interception factor;  $\theta$  - the incidence angle. The efficiency curves are generally calculated at normal incidence; however, the incidence angle for the tracked collector at a single axis change during the operation. The optical efficiency of PTSCs decreases with incidence angle for several reasons, including the increased width of the solar image on the receiver, the decreased transmission of the glazing, the absorption of the absorber, and the spillover of radiation from troughs of finite length. The effect of the angle of incidence

must depend on the difference in all optical properties. It can be correlated by a modification called the change in the angle of incidence (Bannerot and Guven, 1984). A method of reducing the end loss effect in a short trough collector is to recompense the length of the absorber tube. A different way of calculating end loss is presented in cylindrical troughs. The incidence angle varies depend on the tracking mode was used. It can use the relations for describe the incidence angle, as shown in Table 2.1.

Table 2.1. Incidence factors for the various tracking alternatives (Bannerot and Guven, 1984)

Type	Incidence angle, $\cos\theta$	Remarks
<p>Rotation about two perpendicular axes with continuous adjustment to allow the surface because sun is fully normal to coincide with the tracked" solar beam at all times.</p>  <p style="text-align: center;"><b>2-AXIS TRACKING</b></p>	1	No hourly or seasonal variations in output due fully tracking
<p>Orientation along east-west axis and rotation about E-W axis with continuous adjustment to obtain maximum energy incidence.</p>  <p style="text-align: center;"><b>E-W 1-AXIS TRACKING</b></p>	$(1 - \cos^2\delta \sin^2\omega)^{1/2}$	No appreciable variation in seasonal output but considerable variation in hourly output
<p>Orientation along north- axis and rotation about N-S axis with continuous adjustment to obtain maximum energy incidence.</p>  <p style="text-align: center;"><b>N-S 1-AXIS TRACKING</b></p>	$[(\sin\gamma \sin\delta + \cos\gamma \cos\delta \cos\omega)^2 + \cos^2\delta \sin^2\omega]^{1/2}$	No appreciable variation in hourly output but considerable variation in seasonal output
<p>Orientation along polar axis and is rotation about this axis with continuous adjustment to obtain maximum energy incidence</p>  <p style="text-align: center;"><b>POLAR 1-AXIS TRACKING <math>\gamma = \text{LAT}</math></b></p>	$\cos\delta$	No appreciable variation in hourly output but some variation in seasonal output depending on the latitude of the location

A different way to calculate the end-loss in cylindrical troughs is presented (Edenburn, 1976). The optical design of PTSC is influenced by several factors (Güven and Bannerot, 1986; Günther et al., 2011) including obvious changes in the incidence angle effects and sun's width, mirror construction, materials used in the heat collector element, poor operating, incomplete sun's rays tracking, and the manufacturing defects of PTSC (see the Fig. 2.3) for knowing components of the PTSC that effects on the optical efficiency (Mokheimer et al., 2014).

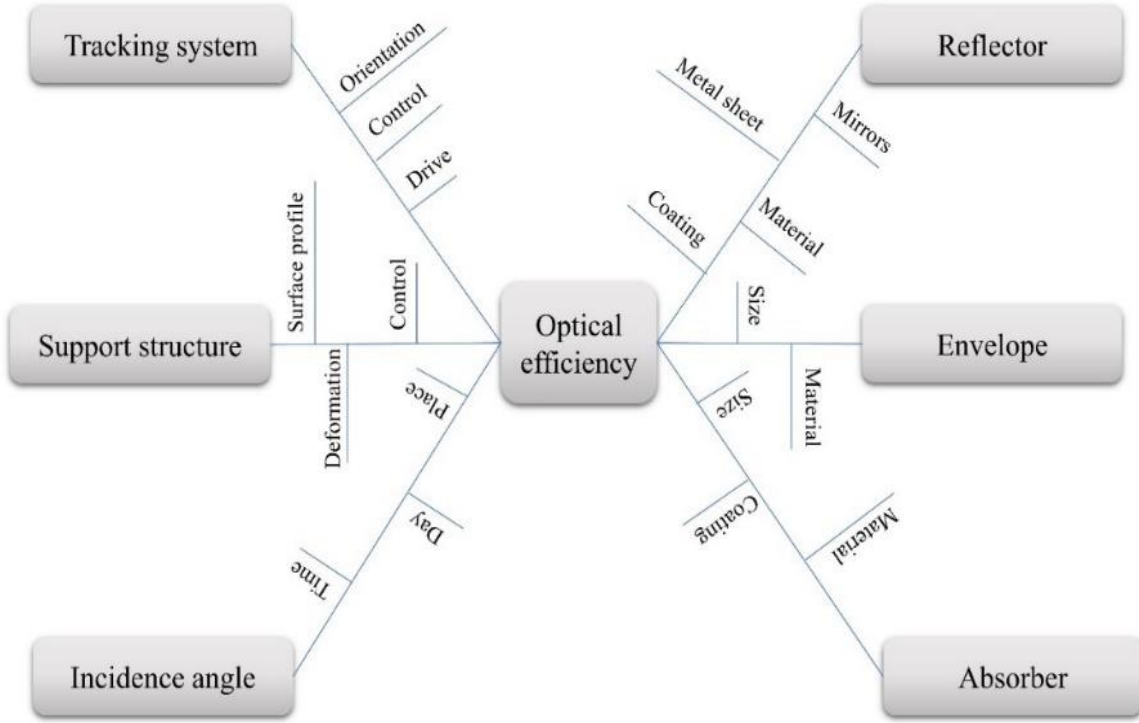


Fig. 2.3. Parameters affecting the optical efficiency (Yılmaz and Mwesigye, 2018)

The next two parts discuss the way in which the analytical and ray tracking approaches for optical errors are perceived and used in the study of PTSCs.

### 2.2.1. Optical analysis of errors

Optical performance is determined by using an analytical approach to obtain the closed intercept factor. A mathematical expression is determined for the intercept factor by Gaussian distribution (Bannerot and Guven, 1984):

$$\gamma_{GUSS} = \int_{-\infty}^{\infty} d\theta f(C\theta) \frac{1}{\sigma_{tot}\sqrt{2}} \exp\left(-\frac{\theta^2}{2\sigma_{tot}^2}\right), \quad (2.2)$$

$$\sigma_{tot} = \left(\sigma_{sun}^2 + \sigma_{mirror}^2 + \sigma_{slop}^2 + \sigma_{tracking}^2 + \sigma_{displacement}^2\right)^{\frac{1}{2}}, \quad (2.3)$$

where:  $\sigma_{tot}$  - total optical error;  $\sigma_{sun}$  - beam intensity error;  $\sigma_{mirror}$  - surface mirror error;  $\sigma_{slop}$  - local slop error;  $\sigma_{tracking}$  - tracking error;  $\sigma_{displacement}$  -displacement error;  $C$ - concentration ratio.

The total optical error  $\sigma_{tot}$  is obtained from this approach by making all errors in a single term (Ehtiwesh et al., 2019). Two groups of optical errors, namely, random, and non-random, are shown in Fig. 2.4.

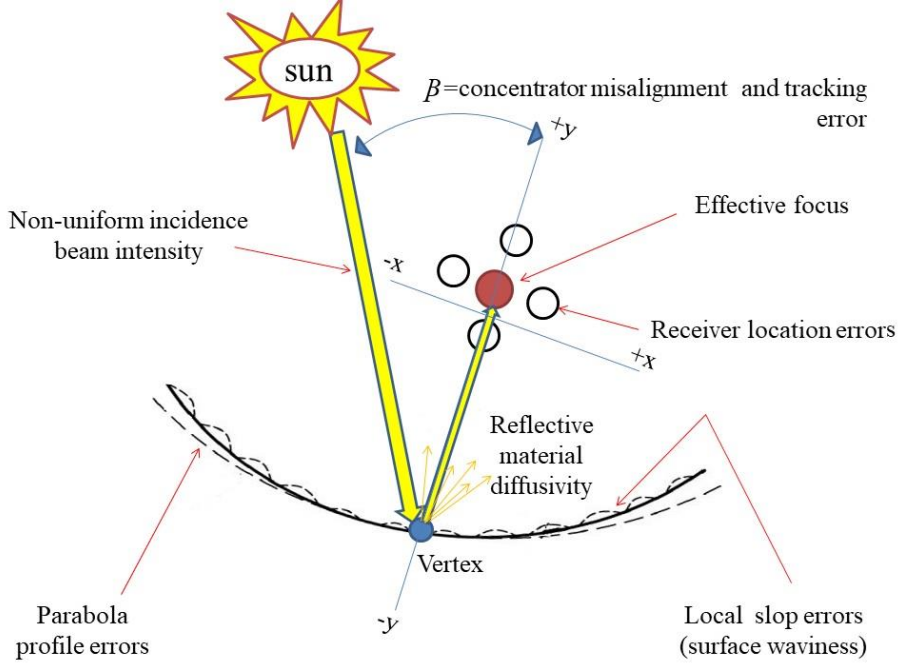


Fig. 2.4. Potential optical error description in PTSCs (Yilmaz et al., 2017)

The intercept factor can be obtained from (Duffie et al., 1985):

$$\gamma = \frac{1 + \cos \varphi_r}{2 \sin \varphi_r} \int_0^{\varphi_r} \left[ \frac{\text{Erf} \left[ \frac{\sin \varphi_r (1 + \cos \varphi) (1 - d^* \sin \varphi) - \pi (1 + \cos \varphi_r)}{\sqrt{2} \pi \sigma^* (1 + \cos \varphi_r)} \right]}{\text{Erf} \left[ \frac{\sin \varphi_r (1 + \cos \varphi) (1 - d^* \sin \varphi) - \pi \beta^* (1 + \cos \varphi_r)}{\sqrt{2} \pi \sigma^* (1 + \cos \varphi_r)} \right]} \right] \frac{d\varphi}{(1 + \cos \varphi)}, \quad (2.4)$$

where:  $E$  - total energy;  $d^*$  - the universal non-random error parameter due to HCE dislocation and mirror profile errors;  $\beta^*$  - the universal non-random error parameter due to angular errors;  $\sigma^*$  - the universal random error parameter.

### 2.2.2. Ray tracing

The ray-tracing technique is used to analyse the optical and optical design/ optimisation performance of PTSCs. It benefits systems that contain many surfaces and Newtonian imaging equations and those in which Gaussian is inappropriate. Ray tracing supplies a massive amount of detailed information for the optical characteristics of the system (Agagna et al., 2018). Computer technology helps reduce the time for optical analyses. Software tools that use the technology of ray tracing include Optical, ASAP, TracePro, SolTrace, and SimulTrough. Using the Monte Carlo ray tracing (MCRT) method in the optical analysis of a PTSC (Benoit et al., 2016). The modelling of propagation of light is tracking the light ray by the optical elements, as shown in Fig. 2.5.



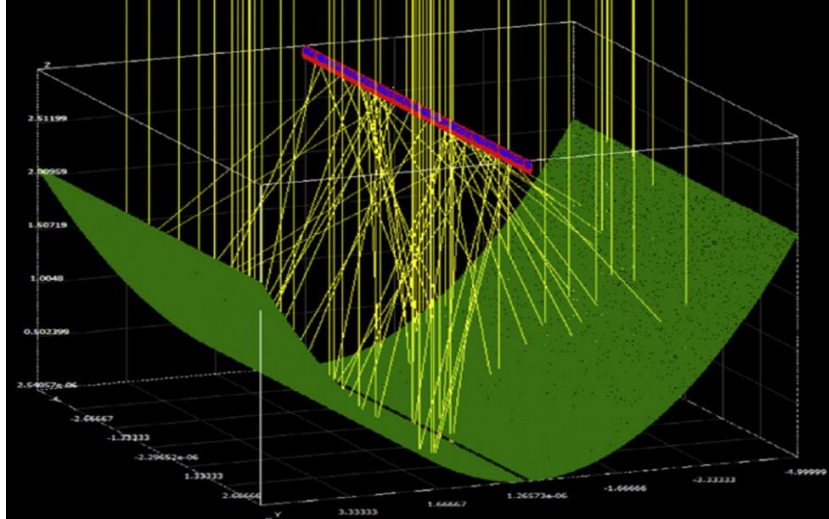


Fig. 2.5. Visualization of the ray-tracing method (Benoit et al., 2016)

### 2.3. Heat transfer element for parabolic trough solar collector

The heat transfer element in PTSC is a major component and contains an absorber tube; it is an essential part that contributes to the proper performance of the system. Solar radiation is focused on the absorber tube, and a heat transfer fluid (e.g., thermal oil, water, and nanoparticle-laden fluid) moves through the tube (Abdulhamed et al., 2018). A schematic of a solar trough parabolic receiver is shown in Fig. 2.6.

The losses are indicated in the cross section of the tube. An evacuated glass envelope covers the absorber tube to reduce heat losses. The fluid flow by forced convection in the absorber tube may be in single or two phases. In this case, the flow process in these systems, the heat transfer coefficients, and the equation to the HCE modelling of heat transfer are much more complex (Cengel, 2011).

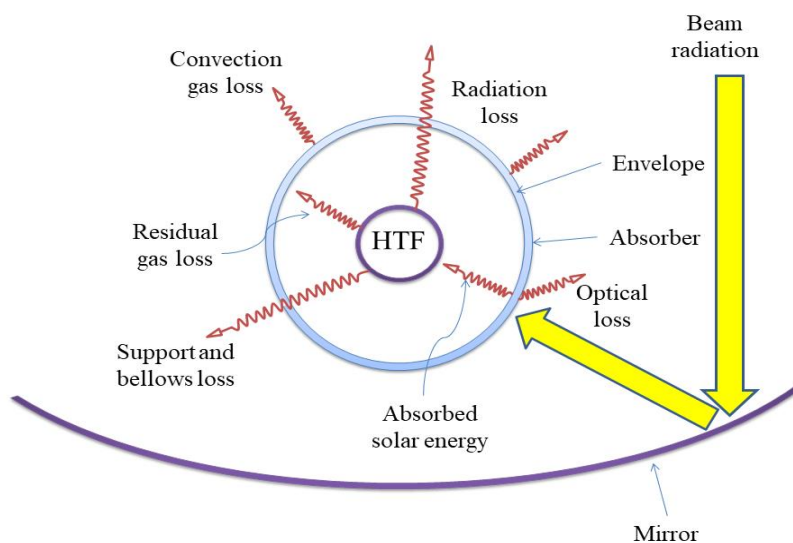


Fig. 2.6. The schematic figure of losses of the solar trough parabolic receiver (Al-Rabeeh et al., 2022b)

## 2.4. Enhancement of optical efficiency

### 2.4.1. Selective surface coating on the receiver tube

Optical efficiency is calculated as the energy ratio of absorbed energy to the energy incident received on the collector's aperture (Hachicha et al., 2013). The coating changes have been improving heat transfer element performance. The HCE output is prone to any difference in the optical properties of the selective coating. Many studies have been conducted to enhance absorption and reduce selective surface emission. The microstructure of the material is influenced by high extremely temperature (Selvakumar and Barshilia, 2012). The coatings should be structurally robust and suitable, safe to handle for extended periods, stable at operating temperatures, environmentally friendly, and relatively inexpensive.

Selective solar absorbers harvest solar energy in the form of heat. The selective solar coating should be structurally and chemically stable at the operational temperature (Selvakumar and Barshilia, 2012). Therefore, the maximum absorption is hard to obtain on a single layer from the coating (Al-Rabeeh et al., 2021c). The spectral selectivity of SSACs may generally be improved by changing the composition of coatings, selecting different materials, or utilising depositing methods (Esposito et al., 2016). On the basis of the mechanisms of absorption and principles of design, five types of selective solar absorbers are defined: (1) intrinsic absorber, (2) semiconductor metal, (3) multilayer interference stacks, (4) cermet, and (5) textured surface (Xu et al., 2020).

The absorption of light depends on many factors, such as the material's electronic structure, wavelengths, and specific surface features including pits, peaks, or voids. Coatings are utilized on glass cover tubes to enhance light transmission in glass (Wang et al., 2019). In general, the glass cover tube coated by anti-reflective coatings have been improved and used in the optical industry to enhance by reducing the reflection. Their characteristics depend on several factors such as composition, shape, wavelength, thickness and temperature (Xin et al., 2013). For example, borosilicate glass tubes improved from 92% to 96% (Manikandan et al., 2019) or more. Thin-film coatings improve collectors' performance by protecting the receiver tube from dirt or corrosion by glass tube cover. Therefore, the glass cover tube reduces convection and corrosion (Zhu Wendelin et al., 2014) (see Fig. 2.7).

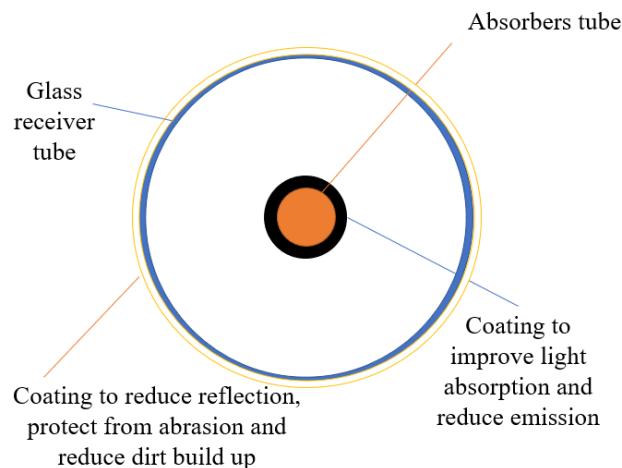


Fig. 2.7. Absorber tubes with a glass cover tube (Atkinson et al., 2015)

Plastics can also be used to improve the performance, reduce operational and maintenance costs, and increase the life of materials in solar collectors (Zhu Kearney et al., 2014). In addition, the solar collector frame should be made from high-entropy alloys because they have superior corrosion resistance, hardness, and intense strength (Krüger et al., 2008).

The next three parts discuss the way in which the methods for preparing selective coatings, the comparison of selective absorber coatings, and thermal stability (TS) are used in the study of PTSCs.

### *2.4.1.1. Methods for preparing selective coating*

Coating preparation is an ageing process that is practiced worldwide for different purposes, such as insulation, thermal barrier, corrosion safety and thermal absorber. This paper will not explain the various coating techniques available and their advantages and disadvantages, as these are discussed in broader literature. To make the tube surface of PTSCs absorbent, certain selective absorptive coatings must be prepared and applied in the system. A solar absorber needs to absorb the radiation whilst minimizing losses to increase the receiver temperature. These coatings are dependent on combinations of metal–metal, metal–ceramic and metal–metal oxide (Bermel et al., 2012). Different types of coatings are prepared using techniques such as physical vapour deposition, thermal chemical coating, spray pyrolysis, electrochemical coating, mechanical coating, and dip coating cathodic and sputtering vacuum deposition and various sputtering techniques. The selection of the deposition technique depends on the requirement of the coating material's specific properties, working conditions and manufacturing cost.

The physical and chemical properties of coatings depend on many factors including substrate structure, layer thickness, cleanliness, purity, substrate temperature, film structure, grain size, void formation and subsequent treatments. The following methods are used to prepare selective coatings (Zhao, 2007; Cao et al., 2014):

- Physical vapor deposition is principally a vaporization coating technique by transferring vapour particle materials to travel directly to the substrate. The whole process is conducted at vacuum conditions by thermal evaporation or electron beam method. For example, a coating material is vaporized by intense thermal from tungsten filament (Fernández-Abia et al., 2013).
- Chemical vapour deposition is a deposition process performed under vacuum conditions to manufacture high-quality, reliable materials with high performance. This process involves a chemical reaction between the materials deposited by halide or an organometallic with other gases to fabricate solid thin films on the substrate surface (Saito et al., 2019).
- Sputtering is a technique that involves the ejection of the coating to the substrate by high-energy particles deposited using bombardment. Inert gas ions have been used to bombard the coating to transmit momentum and energy to the metal substrate (Sharma et al., 2021).

### *2.4.1.2. Comparison of data for selective absorber coatings*

Concentrated solar power plants are currently used for large-scale production in electrical plants to supply approximately 400 MW of power. PTSCs have represented a critical economic

investment and are thus projected to be operational for at least 25 years. Therefore, it is essential to continue maintaining the cost-efficiency of the installation and its high performance rate (Ho et al., 2015; Reoyo-Prats et al., 2019).

The ageing or lifetime mechanisms induced by oxidation, diffusion, grain size change, micro-defects, and optimised ingredients complicate the efforts of scholars to improve the efficiency of solar absorber coatings (Valleti et al., 2016; Kotilainen and Vuoristo, 2016).

In typical PTSCs, the receiver/absorber is essentially one of the main important components of a collector. Therefore, the coating lifetime should be stable to enhance efficiency and reduce maintenance costs (Kotilainen et al., 2016). This is because the coating is in contact with the absorber tube and solar radiation. Moreover, PTSCs can receive about 850 kW/m<sup>2</sup> of heat flux and achieve an outlet working temperature of 600 °C or higher for a fluid receiver (Ho and Iverson, 2014). The coating should be protected from extreme abrasion loss due to environmental conditions (Krüger et al., 2019).

As it is difficult to thoroughly document the exact shape, surface composition, properties, and manufacturing method of absorbers, many mid- and high-temperature solar absorber coatings have been studied (see Table 2.2). The table provides some physical and chemical details for selected transition metal components and compounds and lists various references of compounds as potential absorber coatings.

Table 2.2. Physical and chemical properties of selective absorber coatings

Selective coating	Substrate	method	Absorptivity	Emissivity	Findings	Ref.
AlCrSiN/A lCrSiON/AlC rO	Stainles s steel	Ion plating	0.96	0.14	TS at 600 °C for 600 h in air. Chemically inert, high oxidation resistance and stable microstructure.	(Zou et al., 2016)
CuCr <sub>2</sub> O <sub>4</sub> CuFeMnO <sub>4</sub> Cu <sub>0.5</sub> Cr <sub>1.1</sub> Mn <sub>1.4</sub> O <sub>4</sub>	Copper	Spray- coating	0.972	-	TS at 800 °C for 2000 h in air.	(Rubin et al., 2019)
Al <sub>x</sub> O <sub>y</sub> /Pt/ Al <sub>x</sub> O <sub>y</sub>	Copper	Electr on beam evaporat ion	0.94	0.06	TS at 500 °C for 2 h in air, and 450 °C for 24 h.	(Nuru et al., 2014)
MoSi <sub>3</sub> N <sub>4</sub>	-	Sputte ring	0.926	0.017	TS at 600 °C for in vacum	(Céspe des et al., 2014)
Ni-CrO <sub>x</sub>	Stainles s steel	Sputte ring	0.8	0.14	High spectral selectivity, ranging of solar absorption (0.88 to 0.94) and ranging of thermal emissivity (0.15 to 0.04)	(Teixei ra et al., 2001)

## 2. Literature review

ZrO <sub>x</sub> /ZrC– ZrN/Zr	Stainles s steel	Sputte ring	0.88	0.04	TS at 700°C in vacuum	(Usman i and Dixit, 2016)
ZrO <sub>x</sub> /ZrC– ZrN/Zr	Copper	Sputte ring	0.85	0.1	TS at 600°C in vacuum	(Usman i and Dixit, 2016)
Mo/HfO <sub>x</sub> / Mo/ HfO <sub>2</sub>	Copper	Sputte ring	0.90	0.07	TS at 400 °C for 2h in air, and 600 °C for 2h in vacuum	(Selvak umar et al., 2010)
Mn-Cu- Co-Ox- ZrO <sub>2</sub> /MgF <sub>2</sub>	Stainles s steel	N/A	0.97	0.17	TS at 700 °C for in the air.	(Prasad et al., 2018)
ZrB <sub>2</sub> /Al <sub>2</sub> O <sub>3</sub>	Stainles s steel	sputte ring	0.92	0.11	TS at 600 °C for 100 h in vacuum	(Gao et al., 2019)
W/W <sub>e</sub> Al <sub>2</sub> O <sub>3</sub> / Al <sub>2</sub> O <sub>3</sub>	Stainles s steel	Sputte ring	0.93	0.14	TS at 580°C for 30 days in vacuum	(Anton aia et al., 2010)
SS/Cr/TiAl CrNG/TiAlN /AlSiN/AlSi O	Stainles s steel	Physic al Vapor Depositio n	0.949	0.122	TS at 300 °C for in the air.	(Shiva Prasad et al., 2016)
MnCo <sub>3</sub> O <sub>4</sub>	Inconel 625	Spin coating	0.918 – 0.894	0.87 – 0.88	TS at 600°C for 480h in air.	(Ambro sini et al., 2015)
W/WAlN/ WAlON/Al <sub>2</sub> O <sub>3</sub>	Stainles s steel	Sputte ring	0.958	0.08	High TS and the results show that each layer decreases its refractive index and extinction coefficient from the substrate to surface.	(Dan et al., 2018)
TiAlN/AlO N	Copper	Sputte ring	0.93	0.05	TS at 550 °C for 2h in air, and 800 °C for 2h in vacuum	(Thuné -Boyle et al., 2006)
Al <sub>x</sub> O <sub>y</sub> /Ni/ Al <sub>x</sub> O <sub>y</sub>	Stainles s steel	Sputte ring	0.932	0.038	TS at 400°C for 12h in air	(Tsai et al., 2014)
TiSi <sub>2</sub>	-	Spray coating	0.898	-	TS at 750 °C for 1000h in air	(Wang et al., 2018)
W/CrAlSi N <sub>x</sub> /CrAlSiN xO <sub>y</sub> /SiAlO <sub>x</sub>	Stainles s steel		0.951	0.097	TS at 400°C for 650 h in air.	(AL- Rjoub et al., 2018)
Al <sub>x</sub> O <sub>y</sub> -Pt- Al <sub>x</sub> O <sub>y</sub>	Copper	Electr on beam	0.92	0.1	TS at 550 °C for 2h in air, and 450 °C for 4 h in vacuum	(Nuru et al., 2014)

Mo/HfO <sub>x</sub> / Mo/HfO <sub>2</sub>	Stainless steel	Sputtering	0.9	0.15	TS at 550 °C for 2h in air,	(Selvakumar et al., 2010)
MoSi <sub>2</sub> - Si <sub>3</sub> N <sub>4</sub>	-	Sputtering.	0.88	0.11	TS at 300°C in vacuum.	(Hernández-Pinilla et al., 2016)
CrAlSiN <sub>x</sub> / CrAlSiO <sub>y</sub> N <sub>x</sub>	Stainless steel	Sputtering	0.959	0.097	TS at 600°C for 650 h in a vacuum.	(AL-Rjoub et al., 2019)
W/WSiAl N <sub>x</sub> /WSiAlO <sub>y</sub> N <sub>x</sub> /SiAlO <sub>x</sub>	Stainless steel	Sputtering	0.96	0.096	TS at 450°C for 400 h in air.	(AL-Rjoub et al., 2019)

#### 2.4.1.3. Thermal stability and lifetime of selective absorber coatings

The selective coatings should be thermally stable because they experience rapid and cyclic temperature variations over operation time. High temperature to coating surfaces in air/vacuum can cause surface degradation and oxidation. Hence, TS is a crucial factor to consider (AL-Rjoub et al., 2019). The coating properties should have stable absorptivity and emissivity. Therefore, the coating properties should be investigated during testing and accelerated ageing. Qiu et al. studied the deposition of titanium diboride on stainless steel, which has a strong solar absorptance ( $\alpha = 0.93$ ) and low thermal emittance ( $\varepsilon = 0.11$ ). The tandem absorber coating is characterized by SEM, UV-vis-NIR spectrophotometer, FTIR, XPS, and Micro-Raman methods. The results show that the TS of the SS/TiB<sub>2</sub>/Al<sub>2</sub>O<sub>3</sub> tandem absorber coatings in vacuum was investigated at 400–800 °C for 2 h and 100 h, respectively (Qiu et al., 2019). Palomo et al. examined a MoSi<sub>2</sub>-Si<sub>3</sub>N<sub>4</sub>-based selective coating and showed that the addition of Al<sub>2</sub>O<sub>3</sub> increases TS of the composite even when it is operated continuously for 100 h at 600 °C (Rodríguez-Palomo et al., 2018). By using a magnetron sputtering technique, they deposited a solar selective ZrB<sub>2</sub>/Al<sub>2</sub>O<sub>3</sub> coating on stainless steel. The coating had ( $\alpha = 0.92$ ) and ( $\varepsilon = 0.11$ ). The sample was annealed for 100 h at 500°C and 600°C to test the coating's thermal stability. The results showed that the coating was thermally stable at 500°C (Gao et al., 2019). Magnetron sputtering method was used to prepare a solar selective absorbing coating of NbTiON/SiON on Cu. To achieve high solar selectivity, the new coating's absorptance ( $\alpha = 0.95$ ) and emittance ( $\varepsilon = 0.07$ ) were optimised. The results showed the coating on Cu substrate has steady spectral properties ( $\alpha / \varepsilon$ ) (0.94/0.08) after 40 h at 500°C in vacuum, but reduces at 600°C (Liu et al., 2014). Cheng et al. prepared a Mo-Al<sub>2</sub>O<sub>3</sub> solar selective absorption layer on stainless steel. As seen by AES and SEM with etching depth, the Mo diffuses easily at 400°C, as seen by AES and SEM. Optimizing the deposition conditions resulted in a denser Mo-Al<sub>2</sub>O<sub>3</sub> layer with better TS (Ning et al., 2020). Meng et al. prepared the Cu/Zr<sub>0.3</sub>Al<sub>10.7</sub>N/Zr<sub>0.2</sub>Al<sub>10.8</sub>N/Al<sub>34</sub>O<sub>60</sub>N<sub>6</sub> coating by ion beam deposition. That has ( $\alpha = 0.953$ ) and ( $\varepsilon = 0.079$ ) at 400°C. An annealing test at 400°C in a vacuum shows the deposited coating is thermally stable. The photothermal conversion efficiency decreases from 12.1 to 6.86 at 600°C annealing due to increased emittance (Jian-ping et al., 2018).

As shown above, most present studies on spectrum coatings focus on enhancing optical properties and thermal stability, with little study on evaluating and predicting service life. Researchers should study the factors of accelerated ageing coating performance tests for accuracy, stability, and design. So, investigation of coating applications are required to elucidate the failure mechanism of absorption coatings and establish accelerated ageing, life evaluation, and prediction approaches.

### *2.4.2. Reflective surface*

Aluminium or thin silver coatings are widely used as reflectors for the concentration of solar thermal systems. The reflectivity highly depends on their surface material, which also depends on the deposition, production, and polishing methods (Kennedy, 2007). In general, silver and aluminium have 98% and 88% reflectivity, respectively (McCord et al., 2009). They can be oxidised quickly and effectively by the surrounding environment; therefore, coatings are mostly applied on mirrors to protect the reflective surface from environmental effects such as oxidation and corrosion (Sutter et al., 2015). This is a specific issue with silver mirrors given that silver can be easily tarnished. Silver is applied on the back of the glass to protect it from environmental conditions. To protect silver from mechanical damage and corrosion, a copper layer is typically used on the silver coating due to its smaller standard electrode potential than silver. The reflective surfaces are coated by silver, and then followed layers of copper to increase the quality of the highly polished reflectivity mirror surface 94.5%. The cleaning of mirrors is vital for the efficiency of solar collector assembly (Kennedy and Terwilliger, 2005a). Coatings can help avoid reflector corrosion. However, corrosion persists when the protective layers are penetrated by air or moisture. Losses can be on the order of 10% or more, even using silver and aluminium mirrors (Birch, 2004). Glass mirrors are good reflectors for PTSCs because they have high reflectivity and minimum loss throughout the lifetime. However, glass mirrors are limited by their fragility, weight, and cost-effectiveness. These limitations could be overcome by using mirrors manufactured from polymers because they are lightweight, flexible, and inexpensive. The technological advances in the manufacture of reflectors have developed reflector materials (Khan and Arsalan, 2016). Materials for reflectors are directly deposited, and the structure of the reflector is composed of various layers: topcoat, reflective layer, levelling layer, and substrate. These types of reflectors minimize the requirement for adhesives and lamination (Karas et al., 2018). Silver Teflon reflectors use Teflon, which is an intrinsically weather-proof and non-hygroscopic material with excellent barrier properties. Additionally, Teflon has low surface energy to minimize soil retention resistance. In polymer multilayer reflectors, the material layers are composed of  $\text{Si}_3\text{N}_4$  and Ag–polymer multilayer–Substrate. These reflectors have a high production capacity, reducing production costs (Actin, 2013).

Titanium dioxide ( $\text{TiO}_2$ ) provides photocatalytic properties that can address soiling and cleaning problems related to the concentration of solar energy technology. The photon is excited in the high-level energy of the bandgap of  $\text{TiO}_2$  can catalyse or speed up the organic matter conversion to water and carbon dioxide. This specific property of  $\text{TiO}_2$  is applied in reflectors of PTSCs (Atkinson et al., 2015). Performance loss and surface cleaning cost are two major factors reducing maintenance costs and operation of PTSCs in the long term (Kennedy and Terwilliger, 2005b). For example, reduced solar mirror reflectivity related to soiling will

lead to 8%–12% decreased performance (Zhu Kearney et al., 2014). Addressing cleaning problems is crucial for concentrating solar plants on a large scale due to the low amount of water in desert-type conditions (Brogren et al., 2004). Metallising a suitable and affordable substrate material using polyethylene terephthalate film is one of the most promising methods to minimize the cost of solar mirrors. Then, the reflector's coating by a protective layer in the top for enhancing resistant abrasion and durable (Atkinson et al., 2015).

### *2.4.3. Absorber tube intercept factor*

The intercept factor effects on optical efficiency are determined as part of the ray's incident angle upon the aperture that reaches the receiver for a given incidence angle. The intercept factor is the parameter that embodies the effect of errors. The local slope and profile errors occur during manufacture. Thomas developed a technique to measure the flux distribution around the receiver of PTCs. If the distribution of the flux around the absorber is known, then the intercept factor can be easily calculated (Braham and Harris, 2009).

### *2.4.4. Antireflective surface coating on the glass tube*

In solar applications, borosilicate glass tube should be installed around the absorber should have high transmissometer properties. Selective surface coating on glass increases transmittance from approximately 92% to 96% (Hermoso and Sanz, 2015).

### *2.4.5. Incorporating secondary reflectors*

The essential primary concentrator reflects the solar radiation on the receiver tube either through a mirror or a polished aluminium sheet. The collector that intercepts the radiation flux depends on factors, such as primary focus surface error, rim angle, and rigidity of the structure to withstand wind and self-load, and mechanism tracking accuracy. The spillage or dispersion of high-concentration radiation across the source creates a considerable optical and thus thermal efficiency loss (Wirz et al., 2014).

### *2.4.6. Dual axis tracking and end losses*

The geometrical aspect of the collector determines the optical efficiency and performance, the decrease of the opening area induced by the irregular effect, blocks, shadows, and radiation loss beyond the receiving end. Radiation occurring on the concentrator's edge observe the solar radiation cannot enter to the receiver tube, that called end effect. Xu conducted an optical study of the end loss effect and then proposed a mirror design to enhance TE. The end loss effect is gradually reduced by increased trough length (Xu et al., 2014).

## 2.5. Performance enhancement techniques

Many researchers have studied heat-transfer improvement techniques to enhance the thermal performance of PTSCs and thus increase efficiency. PTSC systems can be improved by changing either its heat collector element properties or optical design. Various heat-transfer enhancement techniques have been used in PTSCs.



### 2.5.1. Parabolic trough solar collector receiver with glass envelope

The materials and dimensions of the absorber tube affect the performance of PTSCs (Cheng et al., 2014). The performance of the collector increases with that of the glass cover tube. The glass cover tube reduces convective heat losses and enhances the performance of the PTSC system by improving the greenhouse effect between the glass and the tube (Li and Wang, 2006). Having a top glass cover increases instant efficiency by 45.56%–62.60% and total efficiency by 10% (Xu et al., 2014). Kasaeian (Kasaeian et al., 2015) designed and manufactured a small prototype model of PTSCs to investigate methods for enhancing the performance of PTCs. The system was compared with different receiver tubes to improve the optical, thermal, and heat transfer of the PTSCs: vacuumed steel tube with black paint, black chrome coated copper tube, copper-vacuumed black chrome coated copper tube, and black chrome coated copper tube with non-evacuated glass cover tube. The test of the different receiver's tube used MWCNT/oil nanofluids (NFs) in 0.2% and 0.3% volume fraction. The best results were obtained in the vacuumed receiver, and the efficiency improved by 11% higher than the non-evacuated tube. The maximum optical and thermal efficiency of the vacuum copper receiver system was found to be 61% and 68%, respectively, due to a high absorption rate of 0.98%.

### 2.5.2. Passive heat transfer enhancement

Many researchers studied the collector improving by passive convective for increasing the heat transfer in the absorber tube. Inserts are utilised within the absorber tube to improve collector TE, such as regularly spaced, straight twisted, helically twisted, twisted perforated tapes, protrusions, dimples, wire loops, longitudinal strips, and insert butterfly strings. The novel design focuses on enhancing optical efficiency by increasing absorbed radiation or decreasing collector heat loss. Using varied inserts disturbs the usual flow pattern of heat transfer fluid, causing turbulence. The thermodynamic, fluid friction, and heat transfer performance increase as width ratio increases and the twist ratio decreases.

A significant decrease in the generation of entropy is achieved at a low Reynolds number at twist ratio and decreased width ratios, while the ideal Reynolds number increases. Considerable increase in heat transfer performance of about 169%, a reduction in absorber tube's circumferential temperature difference up to 68% and an increase in TE up to 10% over a receiver with a plain absorber tube (Mwesigye et al., 2013).


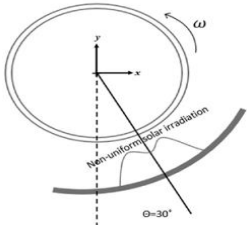
Various porous receiver geometries have been considered for the performance estimate of PTSCs. Thermal analysis of receiver tubes was performed for various geometric parameters, such as thickness and ratio of fin aspect and porosity, for varying heat flux conditions. The porous fins inserted to the tubular receiver of the STC enhanced the heat transfer compared with the solid longitudinal fins (Reddy et al., 2008). Porous circular, triangular, square, and trapezoidal inserts, and the heat losses in all porous inserts were found to be approximately the same (Verma, 2017).

A helically finned is utilised in internal tubes for the design of PTSCs. Many factors, such as thermal loss, pressure loss, thermal fatigue, and thermomechanical stress, affect the

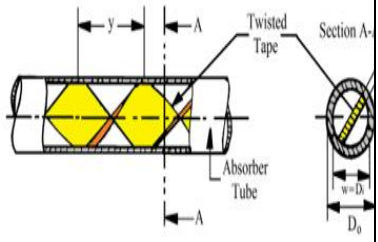
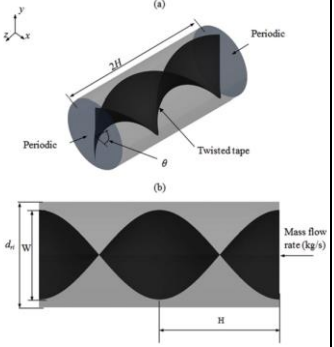
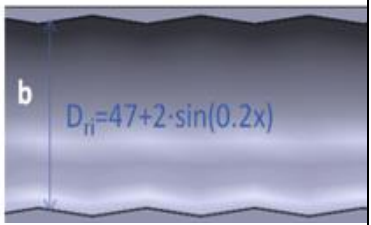
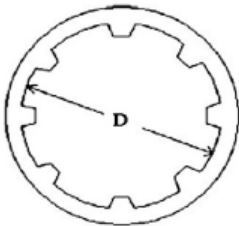

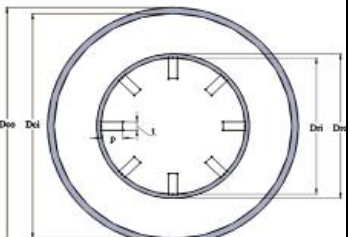
performance of PTSCs (Manikandan et al., 2019). The results show that the parasitic losses associated with the pressure losses in the tube increase with the number of fins and its helix angle. Although the thermal losses and temperature gradients are reduced, the energetic and TE of the collector increase (Muñoz and Abánades, 2011).

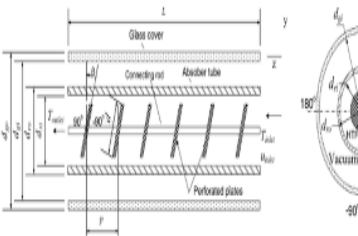

Bader studied the heat transfer analysis of the cylindrical air-based cavity-receiver tube. The receiver efficiency ranged from 45% to 29%. At summer solstice solar noon, the HTF inlet temperature was 120 °C, and the HTF outlet temperature ranged from 250 °C to 450 °C. The loss of solar radiation on the absorber tube is equal to one third by spillage (Bader et al., 2015). The heat loss between two paired horizontal cylinder receivers was studied in conduction and convection in absorber tube from a half-isolated annulus. The application of fibreglass insulation to the half of the annulus away from the parabolic trough increases the reduction of convection heat losses by an average of approximately 25% relative to traditional receivers (Al-Ansary and Zeitoun, 2011). Demagh studied the possibility of establishing a S-curved/sinusoidal receiver tube in PTCs. The PTSC was replaced with a traditional straight absorber, whose designed S-curved/sinusoidal and heat flux density distribution varies on the axial and the azimuthal directions. The heat flux density was distributed on a large surface (Demagh et al., 2015). Xiao designed a tube absorber by a V-cavity on PTSCs. The optical efficiency of the absorber improved with reduced aperture distance and increased depth-to-width ratio (Xiao et al., 2014). Table 2.3 explains some of these studies. On the other hand, several drawbacks in this way, such as increased parasite loads associated with increased pressure loss, noise, and additional manufacturing costs, exist.

Table 2.3. Summary of insert types used to enhance TE of PTSC

Insert type	Method	Working fluid	Model	Thermal eff. (%)	Ref.
Metal foam	EXP	Cu/water		14	(Heyhat et al., 2020)
Rotating tube	CFD	Al <sub>2</sub> O <sub>3</sub> /therminol-VP 1		15	(Norouzi et al., 2020)

2. Literature review

Twisted tape	Model	Water		10	(Jaramillo et al., 2016)
Wall-detached twisted tape	CFD	Syltherm 800		27	(Mwesigye et al., 2016)
Converging-diverging absorber	CFD	Thermal oil		4.55	(Bell os Tzivani dis et al., 2016)
Helical fins	CFD	Syltherm 800		3	(Muñoz and Abánades, 2011)
Longitudinal fins	CFD	Syltherm 800		1.4	(Bell os et al., 2017)
Longitudinal fins	CFD	Syltherm 800		1.27	(Bell os et al., 2017)

Perforated plate	CFD	Syltherm 800		8	(Mwesigye et al., 2014)
Porous discs	EXP	Water		7	(Reddy et al., 2015)

### 2.5.3. Nanofluid

Nanofluid is a term used to describe a fluid in which nanometre-sized particles are suspended with normal scales of 1–100 nm in length (Rehan et al., 2018). Nanoparticles in liquids are suspended to improve TC and heat transfer efficiency of basic liquids. The thermal conductivities of particulate content are typically higher in magnitude, particularly at low volume levels, compared with that of specific fluids, such as water, ethylene glycol, light oils, and NFs (Mebarek-Oudina et al., 2020).

They can dramatically improve the host fluid TE and thermophysical characteristics of PTSCs (O. Al-Oran and Lezsovits, 2020). In the simulations, two major groups emerge: (1) the single-phase modelling that considers the mixture of nanoparticle and base fluid as a single-phase mixture with stable properties and (2) the two-phase modelling that separately considers the properties and behaviour of the nanoparticle from that of the base fluid (Otabeh Al-Oran and Lezsovits, 2020). In Fig. 2.8 shows the common nanoparticles and the base fluids utilized for preparing NFs.

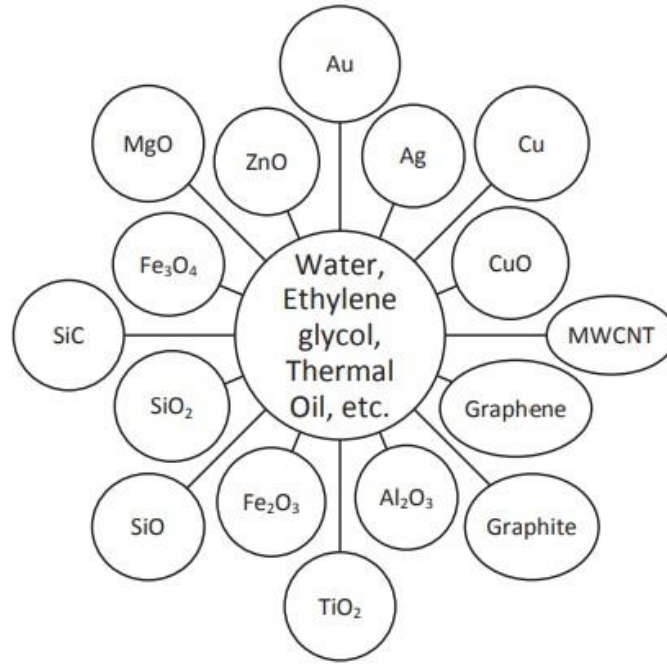


Fig. 2.8. Common nanoparticles and base fluids used in NFs for solar energy applications (Sahin et al., 2020)

The pressure drop increases with the increase in the volume concentration of nanoparticles in the base fluid. When the Reynolds number increases, the pressure drop increases sharply. The pressure drop is a function of the fluid's thermophysical properties and velocity of inlet fluid in the absorber tube (Kakaç and Pramuanjaroenkij, 2016). The force of inter nanoparticles is highly influenced by the concentration of the nanoparticles. The force profiles are influenced by many factors, such as time, size, shape, surfactant concentration and humidity. In more concentrated of nanoparticles increasingly begin to accumulate, swarm, precipitate out of the solution, and adsorb on surfaces (Safaei et al., 2016). For example, synthetic oils have a temperature of  $>400\text{ }^{\circ}\text{C}$ , whereas molten salts reach up to  $600\text{ }^{\circ}\text{C}$ . By contrast, it is anti-freezing systems due their temperature of solidification about  $220\text{ }^{\circ}\text{C}$  (Akbulut et al., 2007).

### 2.5.3.1. Mono nanofluids

A single kind of nanoparticle is suspended with a fluid. In a study, the modelling and simulation of synthesised NFs should predict the thermophysical properties to ensure acceptable results. The thermophysical properties for any nanoparticle and fluid become new properties of density, viscosity, specific heat capacity and TC (Potenza et al., 2017)

Three main parameters involved in calculating the heat transfer rate of the nanofluid are heat capacity, viscosity, and thermal conductivity, which may differ from those of the original pure fluid. The heat transfer analysis of the direct absorption receiver system (see Fig. 2.9) under 2D steady state conditions by the energy balance equation:

$$\frac{1}{r} \frac{\partial}{\partial r} \left( k r \frac{\partial T}{\partial r} \right) - \frac{r q_r}{r dr} = \rho c_p U \frac{\partial T}{\partial x} \quad (2.5)$$

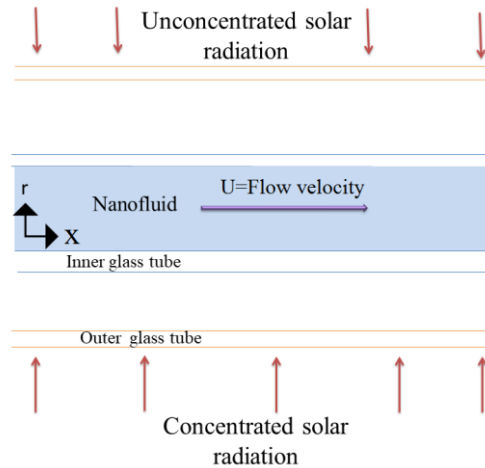


Fig. 2.9. Section view of the direct absorption receiver system (Zaaoumi et al., 2021)

The nanofluid's TC depends on the nanofluid's viscosity and TC of the base liquid and solid particles, as well as the mass, specific heat and volume fraction of the nanoparticles. The heat transfer performance is enhanced by the nanofluid consequent to increasing the properties of the base fluid. The convection heat transfer coefficient is improved due to the increase in volume fraction. The pressure drop increases with the increase in nanofluid density and viscosity (Xuan et al., 2003). Table 2.4 shows the effects of various NFs on the performance of PTSCs.

Table 2.4 Effect of various NFs on the performance of PTSCs

Ref.	NF/basefluid	VC (%)	Effect on the Performance
(Okonkwo et al., 2018)	BH-SiO/water TiO <sub>2</sub> /water	3% 3%	TE is improved by 0.073%, and the coefficient of heat transfer is 138%. The TE is improved by 0.073%, and the coefficient of heat transfer is 128%.
(Cocchia et al., 2016)	Al <sub>2</sub> O <sub>3</sub> /water SiO <sub>2</sub> /water TiO <sub>2</sub> /water ZnO/water Al <sub>2</sub> O <sub>3</sub> /water Au/ water	(5, 10, 20)% (1, 5, 25) % (1,10,20,35) % % (1, 5, 10) % (0.1, 1, 2) % (0.01) %	At low concentrations, only Au, TiO <sub>2</sub> , ZnO and Al <sub>2</sub> O <sub>3</sub> NFs pose minimal changes compared with water use; however, increasing nanoparticles concentration does not appear to have any benefit with respect to water. At high temperatures, the viscosity decreases, and the TC increases
(Mwesigye and Meyer, 2017)	Cu/Therminol VP-1 Ag/TherminolVP-1 Al <sub>2</sub> O <sub>3</sub> -Therminol VP-1	less than 10%	TE for Ag-TherminolVP-1, Cu -TherminolVP-1 and Al <sub>2</sub> O <sub>3</sub> TherminolVP-1 NFs improved by 13.9%, 12.5% and 7.2%, respectively. TC increased, the efficiency of exergy improved, and performance of heat transfer improved.

## 2. Literature review

(Toppi n- Hector and Singh, 2016)	Graphene/Therminol VP-1,	0.02%	Graphene has higher solar absorption than nanoparticles in the aluminium particle. DARS can transfer heat at 265.
	Al/Therminol VP-1	0.09%	
(Bellos and Tzivani dis, 2017)	Al <sub>2</sub> O <sub>3</sub> /Syltherm 800 CuO /Syltherm 800 TiO <sub>2</sub> / Syltherm 800 Cu/ Syltherm 800	-	NFs boost system efficiency and achieve an increase of up to 1.75% relative to pure thermal oil operations. Moreover, Al <sub>2</sub> O <sub>3</sub> and CuO must be used at higher concentrations compared with TiO <sub>2</sub> and Cu.
(Dimens, 2014)	Cu/water	0.02%	Adding of Cu/water significantly improves its absorption characteristics and optical and TE and leads to higher outlet temperatures.
(Mohammad Zadeh et al., 2015)	Al <sub>2</sub> O <sub>3</sub> / synthetic oil	0.02% 0.04%	The presence of nanoparticles increases the coefficient of heat transfer of the working fluid in the absorber tube.
(Kasaeian et al., 2017)	Silica/ ethylene glycol Carbon/ ethylene glycol	0.4%	TC increases TE by adding solid nanoparticles; for MWCNT and nanosilica, the optimal volume fraction is 0.5% and 0.4%, respectively.
(Ferraro et al., 2016)	Al <sub>2</sub> O <sub>3</sub> /synthetic oil	0.5%	The thermal performance and overall efficiency improved slightly with the use of Al <sub>2</sub> O <sub>3</sub> –synthetic oil. The essential advantage of using NFs is reducing the pumping power.
(Subramani et al., 2018)	TiO <sub>2</sub> /water OLE-TiO <sub>2</sub> /water BH-SiO <sub>2</sub> /water	2% 3% 3%	The coefficient of convective heat transfer with TiO <sub>2</sub> /water nanoparticle was increased up to 22.76%, and the maximum efficiency improvement in the PTSC was 8.66% higher than that of the water-based collector.
(Razmand et al., 2019)	Au /water Al /water Ni/water Ag /water TiO <sub>2</sub> /water	2%	By adding different concentrations of nanoparticles, particularly for Au–water and Al–water NFs in a volume concentration of 2%, the measured values are respectively 2.7 and 2.3 times that for pure water; the critical heat flux is significantly improved.
(Heyhat et al., 2020)	CuO/water	0.01% 0.05% 0.1%	Maximum TE improvements are achieved by adding CuO nanoparticles to pure water with 0.01%, 0.05% and 0.1% volume fraction; the results were 3.23, 3.6 and 3.82 times that of pure water.
	Fe <sub>3</sub> O <sub>4</sub>		Enhancing the Reynolds number increases the convective heat transfer coefficient. The results show

(Malek an et al., 2019)	CuO/Therminol 66	4%	that Fe <sub>3</sub> O <sub>4</sub> nanoparticles have great TC from CuO particles under the magnetic field.
(Khakrah et al., 2018)	Al <sub>2</sub> O <sub>3</sub> /synthetic	(1-5) %	The addition of 5% of Al <sub>2</sub> O <sub>3</sub> /synthetic nanoparticles improves the efficiency of relative exergy by about 19%. The exergy efficiencies decrease when wind speeds increase from 5 m/s to 10 m/s.
(Khan et al., 2020)	CuO / water CuO /oil Al <sub>2</sub> O <sub>3</sub> / water Al <sub>2</sub> O <sub>3</sub> /oil	1% 3% 5%	At low enthalpy, water performs better than oil as a base fluid. The performance of the base fluid is increased by adding nanoparticle to the oil. As a nanoparticle, CuO has more effect on the energy and energy efficiency of the system than Al <sub>2</sub> O <sub>3</sub> because its heat conductivity and density are higher.
(Rehan et al., 2018)	Al <sub>2</sub> O <sub>3</sub> /water	0.2 % 0.5% 0.3%	At 2 l/min, the maximum thermal efficiencies obtained with Al <sub>2</sub> O <sub>3</sub> and Fe <sub>2</sub> O <sub>3</sub> NFs are 13% and 11% higher, respectively
(Bretado de los Rios et al., 2018)	Al <sub>2</sub> O <sub>3</sub> /water	1% 3%	At 1% and 3% volume concentration, the maximum efficiency obtained 57.7% and 57.7%, respectively. The thermal performance depends on the incident angle.
(Alsaady et al., 2019)	Fe <sub>2</sub> O <sub>3</sub> /water	0.05	The PTSC efficiency reaches a maximum, which is 25% higher than the traditional.
(Ajay and Kunda n, 2016)	CuO/water SiO <sub>2</sub> /water	0.01%	When 0.01% concentration of CuO/water and SiO <sub>2</sub> /water of the parabolic solar collector, performance is increased by around 7.64% and 6.68% per cent, respectively

### 2.5.3.2. Hybrid nanofluid

Hybrid nanofluid is a new type of nanofluid that is made by dispersing two (or more) different nanoparticles into a working fluid (Al-Rabeeh et al., 2022). HNFs have better thermal performance fluids and thermophysical properties than convectional working fluids such as ethylene glycol, oil, water, and NFs with mono nanoparticles (Subramani et al., 2018).

## 2.6. Computational fluid dynamics analysis

For the numerical modelling of the fluid flow (laminar or turbulent) inside the tube of PTSCs, computational fluid dynamics (CFD) is used to analyse the HCE's overall thermal hydraulic efficiency. The CFD modelling method includes continuity and momentum numerical solutions and energy balance equations. To predict PTSC output correctly during a CFD study, actual boundary conditions must be used. The key to these boundary conditions is the heat flux



on the absorber tube of the HCE. In the study, this heat flux is typically the leading thermal boundary state [38]. Details of studies conducted with CFD are summarised in Table 2.5.

Table 2.5 Summary of traditional PTSC CFD-analysis

Ref.	Type of Study	Findings
(Eck et al., 2010)	Ansys	The difference in the heat flux has a major effect on deciding the overall circumferential HCE temperature.
(Patil Kale et al., 2014)	Fluent	With an increase in the nonuniformity of HCE distribution, heat loss decreases. When the angle of the incidence decreases, heat loss decreases. Therefore, the rate of heat loss gradually decreases in accordance with radius ratio (RR) (i.e., relationship between the inner radius and the outer radius of the absorber envelope), which decreases, thus reaching the minimum amount for RR=1,375 if the heat transferred starts after that critical value only through conduction and convection.
(Patil Panse et al., 2014)	Fluent	The critical of RR is less for large-diameter absorber diameters. For a given HCE, the critical RR is independent of the HCE temperature and outer wind velocity in the weather. In the space of the non-evacuated HCE, the contrast of heat transfer losses in individual and variable temperature in a tube in cases is 1.5%. The RR and wind speed in the evacuated HCE have marginal effects on the thermal losses.
(Bellos and Tzivanidis, 2017)	Fluent	Rising heat transfer at high mass flow rates means the absorber outlet has a high capacity for thermal energy. As the losses in convection rise by wind speeds around the collector, the temperature in the outlet decreases. Therefore, the circumferential temperature gradient is nearly even for the absorber tube of copper material compared with one-steel material.
(He et al., 2011)	Fluent /MCRT-code	The heat flux distribution becomes gentler as the concentration ratio increases, the angle span of the region decreases, and the absorber's shadow effect becomes less powerful. Increasing the concentration rate can also increase the HTF temperature. Increasing the angle of the rim reduces as much heat as possible. When the angle of the rim is small, the glass cover reflects many rays; the temperature elevation is much lower.
(Mokheimer et al., 2014)	Fluent	When the HTF is steam in different process settings, the thermal stress inside the tube is great. Moreover, highly effective solar radiation that focuses on the absorber tube and the high steam temperature contributes to high heat transfer gradients with comparable levels of steam mass flow.
(Mwesigye et al., 2013)	Ansys Fluent /SolTrace	When the angle of rim increases, the gradient of the circumferential temperature on the surface of the absorber is reduced. The reduction in the peak temperature of the absorber is low as the angle of the rim is greater than 80°. Bejan number, a measure in which irreversibility between heat transfer and irreversibility in fluid friction is dominant. As well as increases with a reduction of the rim angle and temperature of HTF and increase the ratio of concentration.
(Li et al., 2016)	Ansys Fluent	The Nusselt number variance is smaller than that of the nonuniform heat transfer flux under uniform heat transfer flux. With the solar elevation angle, the resistance to flow increases. When the number of Grashof increases and the number of Nusselt increases rapidly with the angle of solar elevation then starts to decrease slowly at the increase of higher Grashof numbers and low oh the solar elevation angles.
(Agagna et al., 2017)	MCRT-code/Ansys Fluent	Increased errors in tracking decrease TE. The thermal output is decreased from 70.64% to 9.41% by raising the error of tracking from 0 mrad to 20 mrad.

### **2.7. Summary of literature review**

The depletion of fossil fuels and the associated global warming problem have led our society to focus on using clean energy sources. Solar energy is the oldest form of energy, and it is used for many applications, like heating water in factories and making electricity. Solar energy sources produce no greenhouse gases and are constantly available, making them the best choice for the future. Concentrated solar power has become one of the most preferred energy sources for medium- and high-temperature applications.

PTSC is a type of solar technology that converts solar radiation into thermal energy for industrial and commercial processes. A significant amount of theoretical and numerical research has been conducted in recent years to evaluate and improve the performance of solar parabolic trough collectors. This analysis methodologically holds tremendous knowledge of current and past studies to evaluate the optical and thermal efficiency of PTSC, modelling methods, and future improvements suggested on behalf of the solar collector design for parabolic troughs. Analytical and ray-tracing optical modelling methods are used. According to the research analysis, surface reflectance is critical to TE of PTSC. In addition, different types of coating materials are studied for reflectors and absorber tubes to protect and improve the solar collector's optical efficiency. The optical efficiency depends on material properties such as mirror reflectance, glass cover transmittance, receiver absorption -emitting, intercept factor, geometry factor, and incidence angle. And therefore, the high TE of PTSC depends on selecting an appropriate design of the receiver and the selective coating. It also examines and discusses CFD models used to investigate the physics of solar parabolic trough collectors.

Finally, the studies on the performance and enhancement of PTSCs are examined and presented separately, including novel designs, enhancement of passive heat transfer, and laden flows of nanoparticles inside the absorber tube. A review of these works was presented, as well as an evaluation of other work to improve the optical and TE of PTSC. Based on the research analysis, it is possible to conclude that the present study has the goal of addressing the knowledge gap. Therefore, the current study has been carried out both experimentally and theoretically focused on parametric evaluation of PTSC design, including solar reflecting surface, absorber coating, novel design of receiver tube, and nanofluid.

### 3. MATERIALS AND METHODS

This chapter presents the materials, design, fabrication, techniques, nanofluid preparation, and processes employed in the current research and includes the scientific methods of measurement and a description of test systems to accomplish the set research aims.

#### 3.1. Description and experimental set up

The novel PTSC was designed, fabricated, and tested at the Hungarian University of Agriculture and Life Sciences (MATE) (former Szent Istvan University), Gödöllő city, Hungary, during July and August 2021 and 2022. The geographical location of the city is  $47^{\circ} 35' 39''$  N and  $19^{\circ} 21' 59''$  E as shown in Fig. 3.1.

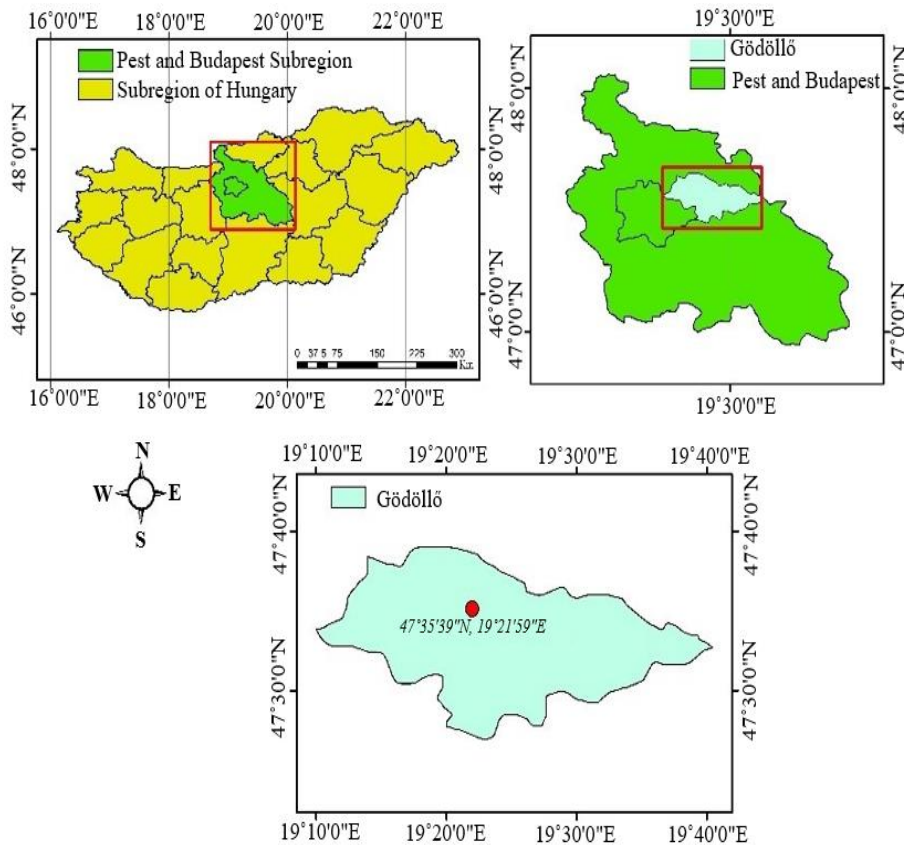


Fig. 3.1. Study area and location of Gödöllő

The PTSC consists mainly of two parts: the reflector surface and the receiver tube. Depending on the focus point, the reflecting surface was formed in a parabolic shape. The reflecting surface consists of polished aluminium sheets or polished mirrors. Solar radiation reflects on the receiver tube, which is held at the focus point. The trough is aligned at the east-west axis or north-south axis, and the sun tracks the sunlight directly onto the surface collector. The fluid passes through the absorber tube and receives thermal energy from the solar radiation. To improve TE of parabolic collectors, the design should be more precise. In addition, there are several other parameters that influence the PTSC efficiency, such as the reflector material used and the receiver tube, the mass flow rate, the heat removal factor, the coefficient of heat transfer, and the working fluid. The design parameters of a PTSC are classified into two main categories, including the following:

- Geometric Parameters
- Functional Parameters

Geometric parameters include the width and length of the aperture, focal length, rim angle, receiver diameter, glass diameter, and the ratio of concentration. Functional parameters are typically including the instantaneous TE, overall thermal efficiency, optical efficiency, and thermal loss of the receiver. A mathematical model of the parabola is shown in Fig. 3.2, considering the coordinate system.

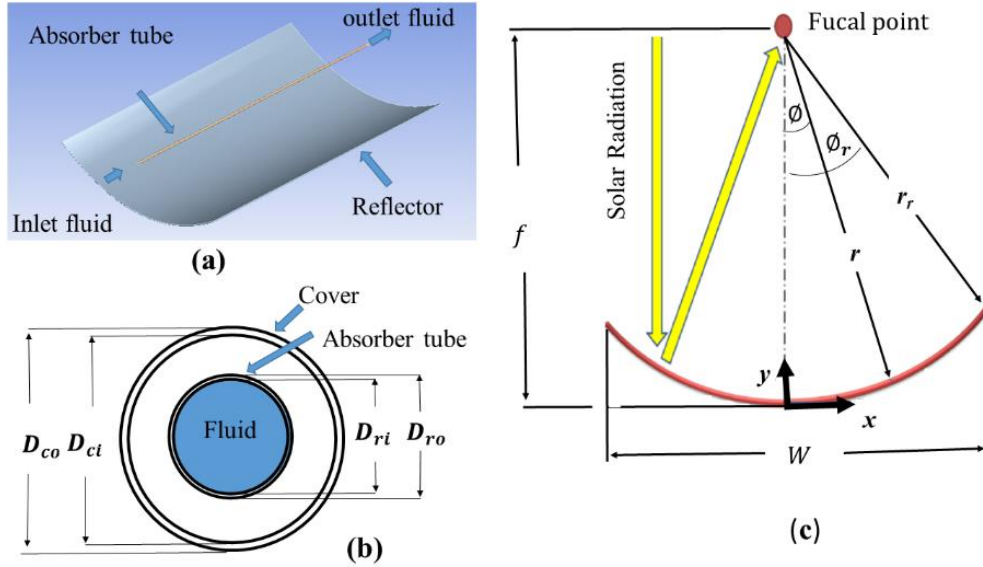


Fig. 3.2. (a) Schematic of a typical PTSC (b) Absorber tube with cover (c) Parabolic concentrator

### 3.1.1. Geometry of parabolic trough solar collector

Two similar prototype PTSCs were made and tested in Gödöllő city at the Hungarian University of Agriculture and Life Sciences, Solar Energy Laboratory. A software called Parabolic Calculator-2 was used to design the prototype of PTSC, as shown in Fig. 3.3. Moreover, the information is checked by the parabolic equations of mathematics, which are described as follows:

$$y = \frac{x^2}{4f}. \quad (3.1)$$

The rim angle ( $\phi_r$ ) can be calculated as follows:

$$\phi_r = \arctan \left[ \frac{8\left(\frac{f}{W}\right)}{16\left(\frac{f}{W}\right)^2 - 1} \right]. \quad (3.2)$$

The local mirror radius for any point of the parabolic reflector is calculated as follows (Collares et al., 1991):

$$r_r = \frac{2f}{1 + \cos \phi}, \quad (3.3)$$

which gives the rim radius  $r_r$  when the angle  $\phi = \phi_r$  as:

$$r_r = \frac{2f}{1+\cos\varphi}. \quad (3.4)$$

The total collector aperture can be determined by multiplying the width (W) by the length (L). The equation for this is as follows:

$$A_a = W L. \quad (3.5)$$

Moreover, the absorber surface of the outside surface of the receiver tube can be calculated as follows:

$$A_{ro} = \pi D_{ro} L. \quad (3.6)$$

The concentration ratio is calculated by dividing the area of the collector aperture by the area of the absorber:

$$C = \frac{A_a}{A_{ro}}. \quad (3.7)$$

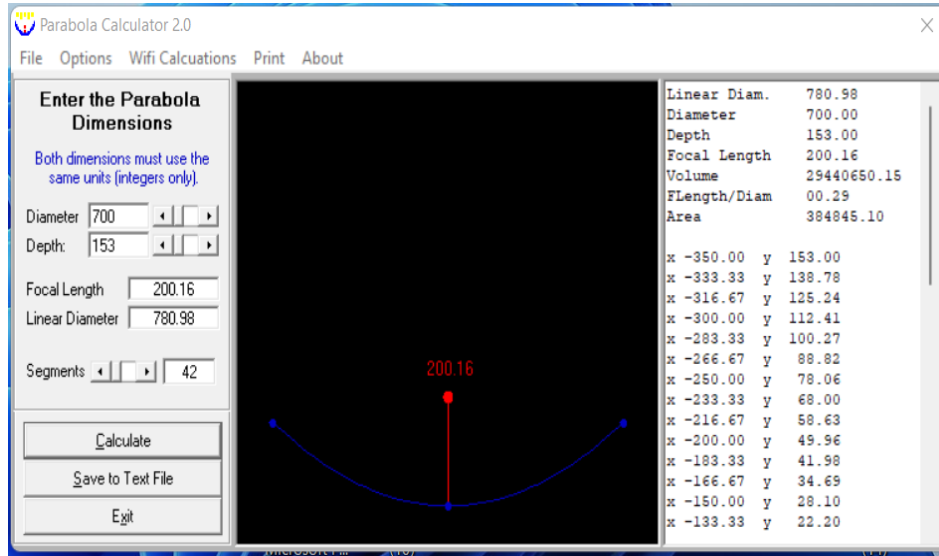


Fig. 3.3 Parabolic Calculator-2 software

### 3.1.2. Thermal modelling

The useful heat from the PTSC can be calculated based on the difference in the temperature of fluid that flows through the receiver tube, according to the following equation (Bellos and Tzivanidis, 2019):

$$Q_u = \dot{m} c_p (T_{out} - T_{in}). \quad (3.8)$$

The solar irradiation on the collector aperture ( $Q_s$ ) can be calculated by multiplying the aperture area by the direct beam solar irradiation as follows (Bellos and Tzivanidis, 2018):

$$Q_s = A_a I_b. \quad (3.9)$$

The thermal efficiency of PTSC is calculated by the ratio of useful heat to available direct beam radiation:

$$\eta_{th} = \frac{Q_u}{Q_s}. \quad (3.10)$$

The thermal efficiency of PTSC can be calculated using this equation as a linear equation (Duffie et al., 1985):

$$\eta_{th} = a + bT^* \quad (3.11)$$

where (a) is the absorbed energy parameter, and calculated as follows:

$$a = F_r \eta_o, \quad (3.12)$$

where (b) is the parameter for the removal of energy (slope):

$$b = -\frac{F_r U_L}{C}, \quad (3.13)$$

where ( $T^*$ ) is the heat loss parameter:

$$T^* = \left( \frac{T_{in} - T_{amb}}{I_b} \right). \quad (3.14)$$

$F_r$  represents the ratio of the actual useful energy to the maximum useful gain.

The optical efficiency of a PTSC is the ratio of energy absorbed by the receiver to that collected by the aperture. The following formula is used to obtain get the PTSC's optical efficiency.

$$\eta_o = \rho \tau \alpha \gamma. \quad (3.15)$$

The following is a formula for determining the Reynolds number:

$$Re = \frac{4 \dot{m}}{\pi D_i \mu}. \quad (3.16)$$

The absorber tube thermal power loss is calculated as:

$$Q_{loss} = A_{ro} U_L (T_{rm} - T_{amb}). \quad (3.17)$$

The thermal losses of the absorber tube to the cover are essentially radiation losses and calculated as follows:

$$Q_{loss} = A_{ro} \sigma \frac{T_{rm}^2 - T_c^2}{\frac{1}{\epsilon_r} + \frac{1 - \epsilon_c}{\epsilon_c} \times \frac{A_{ri}}{A_{co}}}. \quad (3.18)$$

Under steady-state conditions, it is assumed that the cover and absorber have the same thermal losses to the ambient. Thermal losses from the cover to the surrounding environment occur as a result of radiation and convection:

$$Q_{loss} = A_{ro} \sigma \epsilon_c (T_c^2 - T_{sky}^2) + A_{co} h_{out} (T_{rm} - T_{amb}). \quad (3.19)$$

Heat transfer coefficient ( $h_{out}$ ) and sky temperature ( $T_{sky}$ ) are given by (Qiu et al., 2017):

$$h_{out} = 4 V_{wind}^{0.58} D_{co}^{-0.42}, \quad (3.20)$$

$$T_{sky} = 0.0552 T_{amb}^{1.5}. \quad (3.21)$$

### 3.1.3. Optical modelling

The energy balance equation can express the absorbed solar radiation ( $Q_{abs}$ ) as thermal losses and useful heat, as follows:

$$Q_{\text{abs}} = Q_u + Q_{\text{loss}}. \quad (3.22)$$

The absorbed solar energy depends on the solar collector optical efficiency and the solar irradiation:

$$Q_{\text{abs}} = \eta_{\text{opt}} Q_s. \quad (3.23)$$

The solar radiation incidence angle affects optical efficiency and is expressed as:

$$\eta_{\text{opt}}(\theta) = K(\theta) \eta_{\text{opt-max}}. \quad (3.24)$$

The incidence angle modifier is:

$$K(\theta) = \cos(\theta) - \frac{f}{L} \left( 1 + \frac{W^2}{48f^2} \right) \sin(\theta). \quad (3.25)$$

### 3.1.4. Heat transfer analysis

Convective heat rate for unit length inside the absorber tube between the heat transfer fluid and the absorber can be calculated as:

$$Q_{\text{conv}} = \pi D_{\text{ri}} h_{\text{htf}} (T_{\text{ri}} - T_{\text{htf}}), \quad (3.26)$$

The heat transfer coefficient ( $h_{\text{htf}}$ ) can be calculated as:

$$h_{\text{htf}} = \frac{\text{Nu } k}{D_{\text{ri}}}, \quad (3.27)$$

For laminar flow:  $\text{Nu} = 4.36$ ,

and for turbulent flow:

$$\text{Nu} = 0.023 \text{Re}^{0.8} \text{Pr}^{0.4}. \quad (3.28)$$

Convective heat rate in the annulus and free molecular convection heat rate for unit length in the annulus can be calculated as (Cengel and Ghajar, 2011):

$$Q_{\text{conv}} = \frac{2\pi k_{\text{eff}}}{\ln(D_{\text{ci}} - D_{\text{ro}})} (T_{\text{ro}} - T_{\text{ci}}). \quad (3.29)$$

The radiative heat transfer rate for unit length from the outside wall of the absorber to the inner wall of the glass cover can be calculated as:

$$Q_{\text{rad}} = \frac{\sigma \pi D_{\text{oa}} (T_{\text{ro}}^4 - T_{\text{ri}}^4)}{\frac{1}{\varepsilon_a} + \frac{(1 - \varepsilon_c) D_{\text{ro}}}{\varepsilon_c D_{\text{ri}}}}. \quad (3.30)$$

Convective heat rate for unit length over the glass envelope:

$$Q_{\text{conv}} = \pi D_{\text{co}} h (T_{\text{co}} - T_{\text{amb}}). \quad (3.31)$$

Radiative heat rate for unit of length from the glass envelope can be calculated as:

$$Q_{\text{rad}} = \pi D_{\text{co}} \varepsilon (T_{\text{co}}^4 - T_{\text{sky}}^4). \quad (3.32)$$

## 3.2. The components of parabolic trough solar collector system

The main components of PTSC are as follow:

#### 3.2.1. Reflector surface

The parabola curve was drawn by the SolidWorks program, and then a CNC machine was used to cut the wood pieces as a parabola curve. The CNC machine is perfect for cutting all of the wood pieces to the same dimensions with minimal errors, and these wood pieces were then fixed to the structure as shown in Fig. 3.4. An aluminium sheet is fixed on the parabola curve, concerning the wood pieces curve. The aluminium sheets have many advantages, including high flexibility, resistance to different weather conditions, very high reflectivity, configuration, and ease of installation, as shown in Fig. 3.5. In addition, a silver chrome film (SCF) (shown in Fig. 3.6) was fixed on aluminium sheets to increase the amount of reflected solar radiation.



Fig. 3.4. Reflector surface structure



Fig. 3.5. Aluminium sheets reflective surface



Fig. 3.6. silver chrome reflective film



#### 3.2.2. Absorber tube

The material used as an absorber tube has effects on the heat transfer between the metal and fluid, thus affecting the performance. In this research, copper has been used in receiver tube material due to its high mechanical strength, low self-weight, and corrosion-resistant properties. Furthermore, copper is readily available material for receiver tubes. The experiment set-up is used for four different cases, as follows:

##### 3.2.2.1. Single evacuated absorber tube

The single copper tube has an inner and outer diameter of 10 and 12 mm, respectively. It was painted with a matte black coating since matte coatings have a high absorptivity of up to 0.95. Then it was inserted into a glass tube with an inner diameter of 54.4 mm. After that, the ends of the glass tube were sealed at both ends by thermal silicone material. Moreover, a vacuum pump was used to void the air inside the glass tube to reduce the heat loss, as shown in Fig. 3.7.

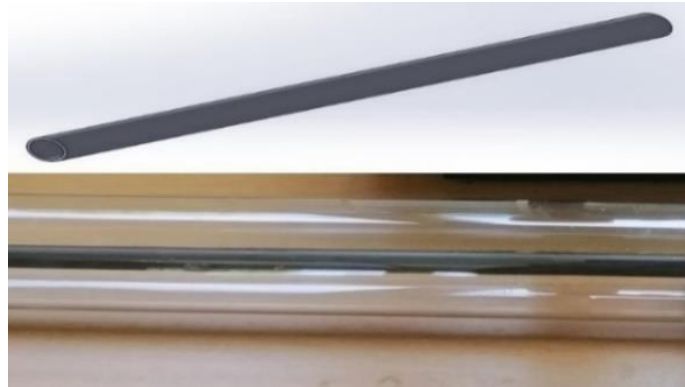


Fig. 3.7. single copper tube with evacuated glass tube

##### 3.2.2.2. Double evacuated absorber tube

The copper tubes have been formed into a U-shape and welded together on one side, while their other side's ends are separate, as shown in Fig. 3.8. The copper tube has an inner and an outer diameter of 7.5 and 8 mm, respectively. Then, it was inserted into a vacuum glass tube, where the evacuated glass tube has one end open and the other closed, with an inner diameter of 43 mm and an outer diameter of 58 mm.

In addition, the fibreglass bung was put at the open end of the glass evacuated tube and tightly rolled around the two copper tubes to seal the open end and prevent heat flow from it. Furthermore, Teflon thin material is used at both ends of the tube to prevent contact between the copper tube and the inside surface of the glass tube.



Fig. 3.8. Double evacuated absorber tube

#### 3.2.2.3. Loop evacuated absorber tubes

A new design was made for the copper tube to increase the heat exposed to the tube by increasing the length of the tube. It has been formed into a loop and welded together on one side, while the other side ends were kept separated, as shown in Fig. 3.9. The copper tube has an inner and an outer diameter of 7.5 and 8 mm, respectively. Then, it was inserted into a vacuum glass tube, where the evacuated glass tube has one end open and the other closed, with an inner diameter of 43 mm and an outer diameter of 58 mm. In addition, the fibreglass bung was put at the open end of the glass evacuated tube and tightly rolled around the two copper tubes to seal the open end and prevent heat flow from the open end. Furthermore, Teflon material is used at both ends of the tube to prevent the contact between the copper tube and the inside surface of the glass tube.



Fig. 3.9. Loop evacuated absorber tube

#### 3.2.2.4. Double evacuated absorber tube with flat plate

A new design was made for the copper tube to increase the area exposed to solar radiation. The copper tubes have been formed into a U shape and welded together on one side, while their other side ends are separate. The copper tube has an inner and an outer diameter of 7.5 and 8 mm, respectively. A flat plate was welded to a tube with dimensions of 1, 40, and 1700 mm

(thickness, width, and length), where the welding was done along the tube so that the contact was complete with the tube and the heat transfer occurs by conduction without any gap between them. Then, it was inserted into a glass tube with an inner diameter of 54.4 mm. The ends of the glass tube were sealed at both ends with thermal silicone material. Moreover, a vacuum pump was used to remove the air inside the glass tube to reduce the heat loss, as shown in Fig. 3.10.

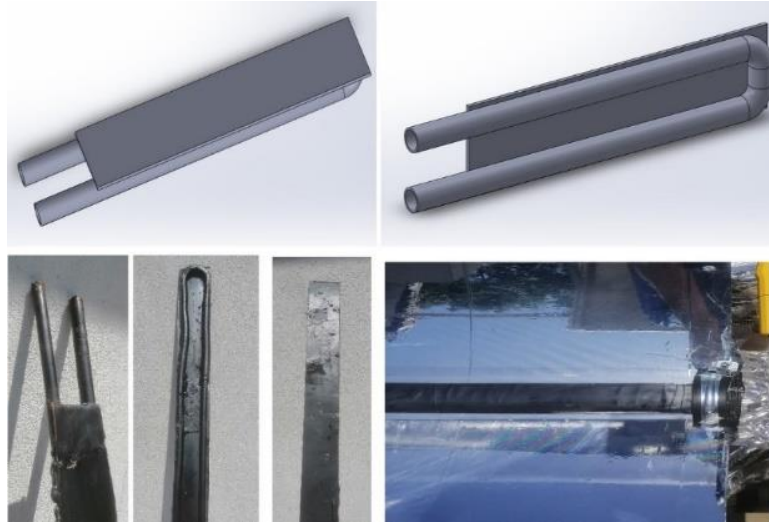


Fig. 3.10. Double evacuated absorber tube with flat plate

#### 3.2.3. Glass receiver

Two types of glass tubes were used according to the appropriate design of the copper tube, as follows:

##### 3.2.3.1. Evacuated glass tube

Evacuated glass tubes are made up of two glass tubes. The outer diameter, which is 58 mm, allows solar radiation passing through, and the inner diameter, which is 43 mm, is coated with CU/SS/AL-N/AL selective absorber coating material. The air is removed from the space between the two glass tubes help to absorb solar radiation and converting it into heat. The glass has a thickness of 1.6 mm and length of 1800 mm, as in Fig. 3.11.

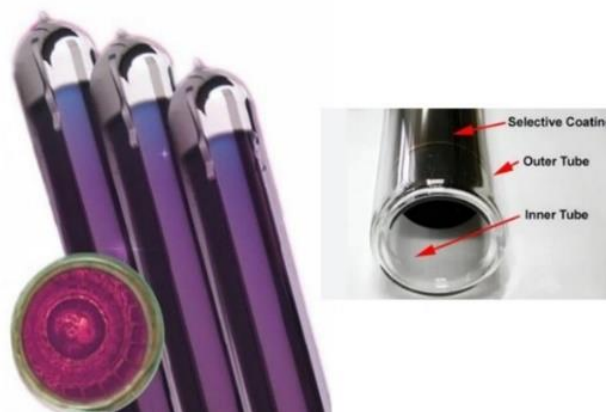


Fig. 3.11. Evacuated glass tube

#### 3.2.3.2. *The single glass tube*

The single glass tube has an outer diameter of 58 mm. The ends of the glass tube were sealed at both ends with thermal silicone material. Moreover, a vacuum pump was used to remove the air inside the glass tube to reduce the heat loss, as shown in Fig. 3.12.



Fig. 3.12. Single glass tube

#### 3.2.4. *Structure of support*

The PTSC structure is made of iron and dimensions of 60 mm by 40 mm with a thickness of 2 mm. The iron is very strong to withstand wind loads and stress loads. A piece of wood in a parabola shape is used to connect the structure and reflective surface, as shown in Fig. 3.13. since wood is very easy to shape into a parabolic curve, which reduces the error caused by design and fabrication.



Fig. 3.13. Support structure

#### 3.2.5. Storage tank

Two storage tanks of 25-liter capacity were used to be filled with the working fluid. Each one was well thermally insulated by soflon form and covered with aluminium foil to avoid the heat losses of thermal energy from tank surface, as shown in Fig. 3.14.



Fig. 3.14. Storage tank

#### 3.2.6. Silicone pipes

Flexible silicone pipes were used to connect the absorber tubes, pump, cooling system, and storage tank all together. The silicone pipes are a very suitable choice due to its properties such as corrosion resistance, weather reactions, and chemical reactions. Furthermore, the silicon pipes have been covered by rubber insulation pipes and aluminium foil to reduce the heat losses to the atmosphere.

#### 3.2.7. Solar tracking mechanism

A manual tracking mechanism is used in this prototype as it is easy and cheaper than an electrically controlled one.

In addition, it achieves the same results as automatic tracking. Automatic tracking is expensive, as well as it needs motor and gear mechanism. Fig. 3.15. shows the mechanism with the required angle. In this research, one axis for tracking is adopted, with east-west alignment and the system rotating with the required angle every 10 minutes manually.



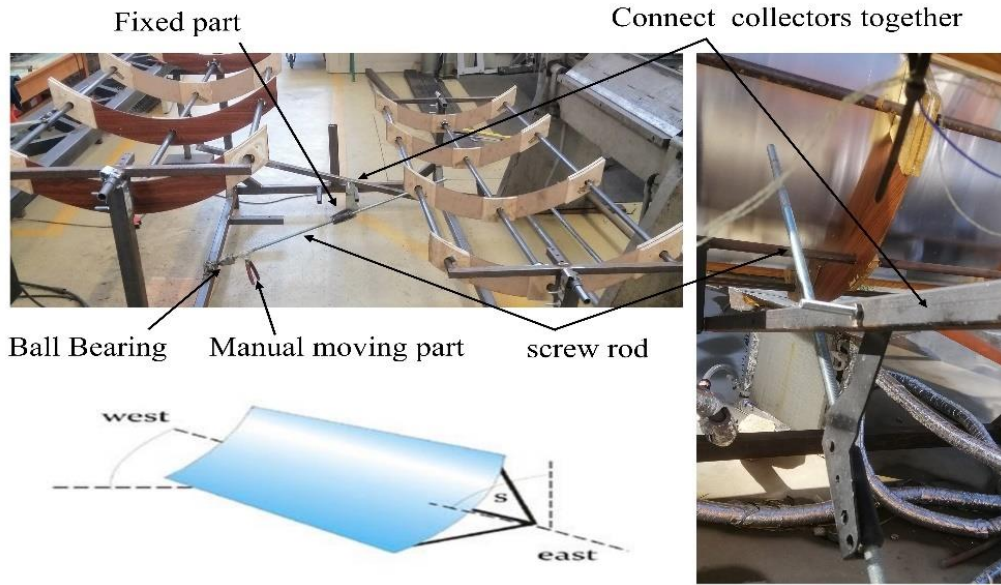


Fig. 3.15. Tracking mechanism

### 3.2.8. Cooling system

The cooling system is a heat exchanger used for cooling the working fluid, placed between the collector and the storage tank. Furthermore, fins were welded on the surface of pipes to increase heat dissipation by increasing the contact area, and an axial fan is used to force air to move around the pipe to cool it; thus, cooling the working fluid, as shown in Fig. 3.16.

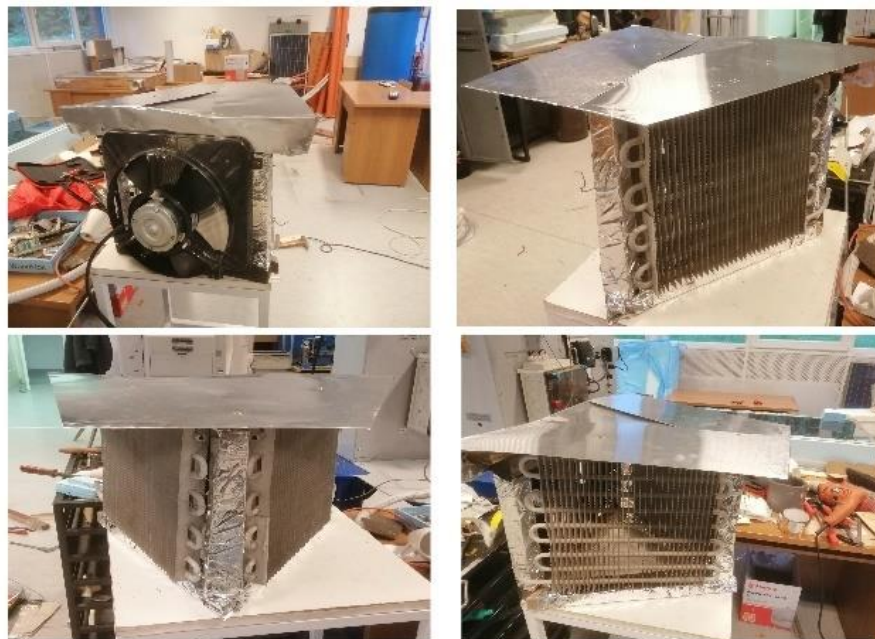


Fig. 3.16. Cooling system

### 3.2.9. Measuring devices

The devices used for measuring and recording the data are described as follows:

#### 3.2.9.1. *The pyrometer*

A Fluke FLK-IRR1-SOL Solar Irradiance Meter is used to measure the solar radiation coming from the sun. The device measures the amount of radiation in  $\text{W/m}^2$  with a measuring range of 100 to 1400  $\text{W/m}^2$ . This device can measure several parameters, such as solar irradiance, tilt angle, and temperature. Fig. 3.17 shows the device used in this experiment.



Fig. 3.17 Fluke FLK-IRR1-SOL solar irradiance meter

#### 3.2.9.2. *LUTRON BTM-4208SD data logger*

A digital thermometer with a LUTRON BTM 4208SD data logger of 12- digital channels was used to measure fluid temperature, having an accuracy of 0.4 °C. The data is saved to an SD card, and the data is saved in Excel. Fig. 3.18 shows the device used in this experiment.



Fig. 3.18. LUTRON BTM 4208SD data logger

#### 3.2.9.3 *Mass flow rate*

The amount of mass flow rate was measured by Omega rotameter device, which connected to the circuit in the direction of working fluid flow before the PTSC inlets. For a guaranteed mass flow rate with no error, a measuring jar with a 1000-ml capacity was used, measuring the time required to fill a finite quantity of the jar by working fluid.

#### 3.2.9.4. *Thermocouples*

Type-K thermocouples are used to measure the temperatures at the inlet and outlet positions in the PTSC. This type can measure temperatures ranging from -200 °C to 1250 °C. The thermocouples are fixed in the specified place using a special silicon fitting.

### 3.3. Experimental uncertainty analysis

For error analysis, we should evaluate the errors that are caused by experimental research, such as TE. The following formula is used to calculate the amount of uncertainty in TE. Table 3.1 shows the uncertainty associated with the involved parameters. Table 3.2 presents the uncertainty of the TE for each case.

$$\eta_{th} = \frac{\dot{m}c_p(T_{out}-T_{in})}{A_a I_b}. \quad (3.33)$$

$$\frac{\delta\eta_{th}}{\eta_{th}} = \sqrt{\left(\frac{\delta\dot{m}}{\dot{m}}\right)^2 + \left(\frac{\delta(T_{out}-T_{in})}{(T_{out}-T_{in})}\right)^2 + \left(\frac{\delta A_a}{A_a}\right)^2 + \left(\frac{\delta I_b}{I_b}\right)^2}. \quad (3.34)$$

Table 3.1. Measurement uncertainties

Variable	Uncertainty (%)
Flow meter	$\mp 0.08333$ L/min
Temperature	$\mp 0.1$ °C
Aperture area	$\mp 0.001$ m <sup>2</sup>
Solar Irradiance	$\mp 1$ W/m <sup>2</sup>

Table 3.2. Uncertainty for each case

Test	Uncertainty
The single-evacuated absorber tube	1.8%
Double-evacuated absorber tube	2.0%
Loop evacuated absorber tubes	2.3%
Double evacuated absorber tube with flat plate	2.6%

### 3.4. Preparations of hybrid nanofluids

NFs used in this study were prepared using a two-step method. The two-step process is the most economical way to produce NFs in large quantities. A digital scale with an accuracy of 1 mg, an ultrasonic vibrator, and a stirrer were utilised. Four volume concentrations (VCs) of HNFs were prepared: 0.01%, 0.05%, 0.1%, and 0.2% NFs. The properties of graphene and Fe<sub>3</sub>O<sub>4</sub> nanoparticles are shown in Tables 3.3 and 3.4. The nanofluid (NF) was prepared using a mixing ratio of 1:1 graphene to Fe<sub>3</sub>O<sub>4</sub> nanoparticles with water as the base fluid and adding Gum Arabic (GA) surfactant. The structural properties of graphene and Fe<sub>3</sub>O<sub>4</sub> nanoparticles were analysed by X-ray diffraction, as shown in Fig. 3.19. The NFs (graphene, Fe<sub>3</sub>O<sub>4</sub> and water) were placed in a beaker (200 mL) and stirred for 1 hour, followed by 2.5 h of ultrasonic mixing to break down agglomeration between particles and produce uniform dispersion in the base fluid to create a stable NF. A fungilab viscometer was used to measure the viscosity of the samples. The viscosity was measured at five temperatures ranging from 20 °C to 60 °C. The TC of NFs was measured using transient hotwires.



### 3. Materials and methods

Table 3.3. Properties of graphene nanoparticles

Parameter	Value
Purity	99.5+%
Colour	Black
Average Particle Diameter	15 $\mu\text{m}$
Thickness	6–8 nm
Bulk density	0.05–1.0 $\text{g}/\text{cm}^3$
SSA	120–150 $\text{m}^2/\text{g}$
Morphology	Platelet
True density	2.25 $\text{g}/\text{cm}^3$

Table 3.4. Properties of  $\text{Fe}_3\text{O}_4$  nanoparticles

Parameter	Value
Purity	98+%
Colour	Dark brown
APS	20–30 nm
Bulk density	0.84 $\text{g}/\text{cm}^3$
SSA	40–60 $\text{m}^2/\text{g}$
Morphology	Spherical
True density	4.8–5.1 $\text{g}/\text{cm}^3$

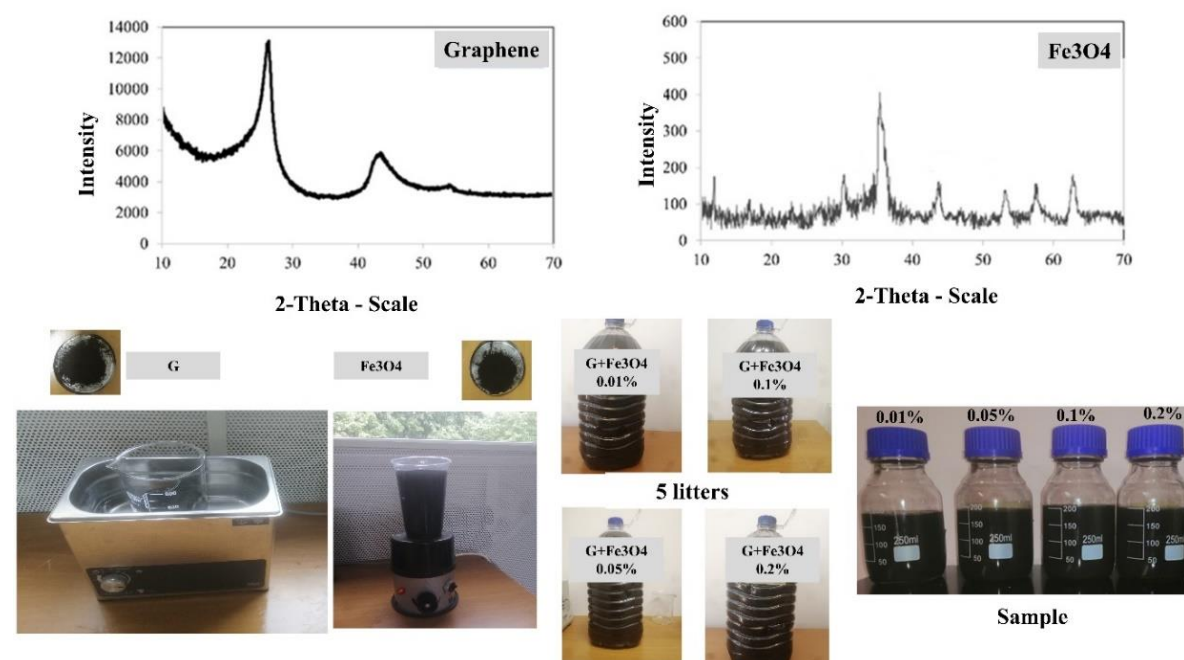


Fig. 3.19. XRD analysis and HNF photo

This method is highly precise and was developed by various authors and presented in 1931 to calculate absolute TC (Okonkwo et al., 2020). TC of graphene–  $\text{Fe}_3\text{O}_4$ /water was measured

using the KD2 Pro thermal properties analyzer (Decagon Devices, Inc., USA), as shown in Fig. 3.20. Numerous authors have utilised this method and obtained good results for NFs (Al-Oran et al., 2020) (Estellé et al., 2015). The device contains a single-needle sensor and a readout unit that should be placed into the medium (fluid sample) to be measured. The 1.27 mm thermal probe has a heating element and a thermoresistor. The probe should be placed vertically into the sample fluid. The data were obtained by simultaneously heating the probe and monitoring its temperature change. Thermal sensors sense temperature changes and microprocessors store them. TC was measured at five different temperatures ranging from 20 °C to 60 °C with a 10 °C interval between each temperature. Five temperature measurements were obtained for each VC with a constant time interval of 15–20 min. The results were recorded for the average value of the temperature. All samples were stable, and no sedimentation has been detected in the samples for an extended period of time prior to the experiments.



Fig. 3.20. KD2 Pro device

The volume concentration is evaluated from the following relation in percentage of HNFs using the equations:

$$\phi\% = \frac{\frac{m_{np1}}{\rho_{np1}} + \frac{m_{np2}}{\rho_{np2}}}{\left(\frac{m_{np1}}{\rho_{np1}} + \frac{m_{np2}}{\rho_{np2}}\right) + \frac{m_{bf}}{\rho_{bf}}} 100. \quad (3.35)$$

#### 3.4.1. Effect of temperature on thermal conductivity

The experimental investigation of the TC variations of graphene–Fe<sub>3</sub>O<sub>4</sub>/water (1:1) was presented. The tests were carried out at five different temperatures ranging from 20 °C to 60 °C with VCs ranging from 0.01% to 0.2%. According to the experimental results (Sarbolookzadeh Harandi et al., 2016), the thermal conductivity ratio (TCR) and thermal conductivity enhancement (TCE) are defined in as follows:

$$TCR = \frac{k_{nf}}{k_{bf}} \quad (3.36)$$

$$TCE(\%) = \frac{k_{nf} - k_{bf}}{k_{bf}} 100 \quad (3.37)$$

where  $k_{nf}$  is the TC of base fluid, while  $k_{bf}$  is the TC of NFs.

Fig. 3.21 a shows that the TC of NF increases with particle concentrations and temperatures. The TC of the 0.2% HNF was evaluated at 20 °C and was observed to be 0.625 W/m K, which is 4.87% higher than the TC of the base fluid (0.596 W/m K). Similarly, the TC of the 0.2% HNF was evaluated at 60 °C and was observed to be 0.731 W/m K, which is 14.4% higher than the TC of the base fluid (0.639 W/m K). The TC rises as a result of micro convection and Brownian motion of particles in base fluid. The effects of the change in temperature on TC are significant at higher VCs. Fig. 3.21 b shows the changes in TC as a function of temperature at various VCs. Moreover, under constant VC, TC increases with increasing temperature. Fig. 3.22 shows the variation of the TCR of HNF versus VC and temperature.

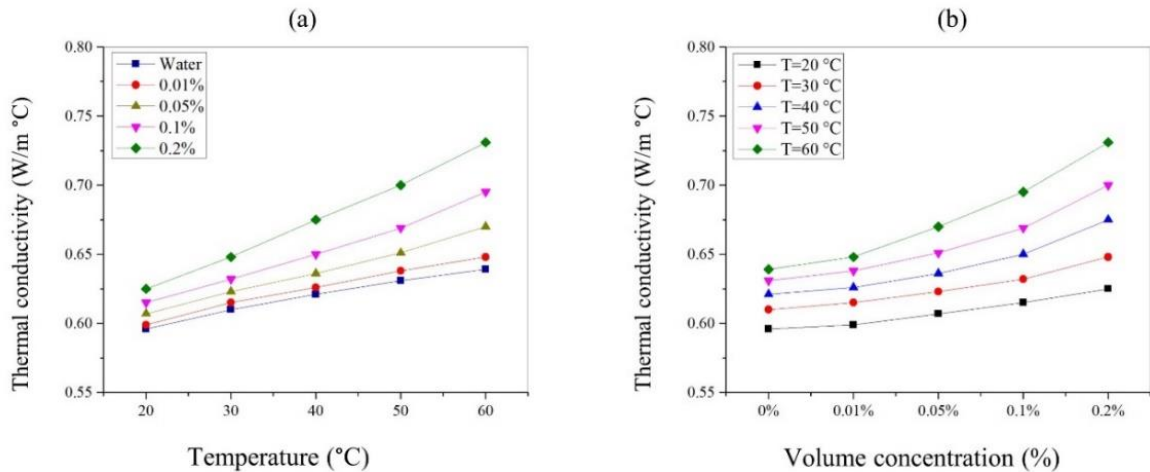


Fig. 3.21. TC of HNF with (a) VCs at different temperatures, (b) Different temperatures at various VCs

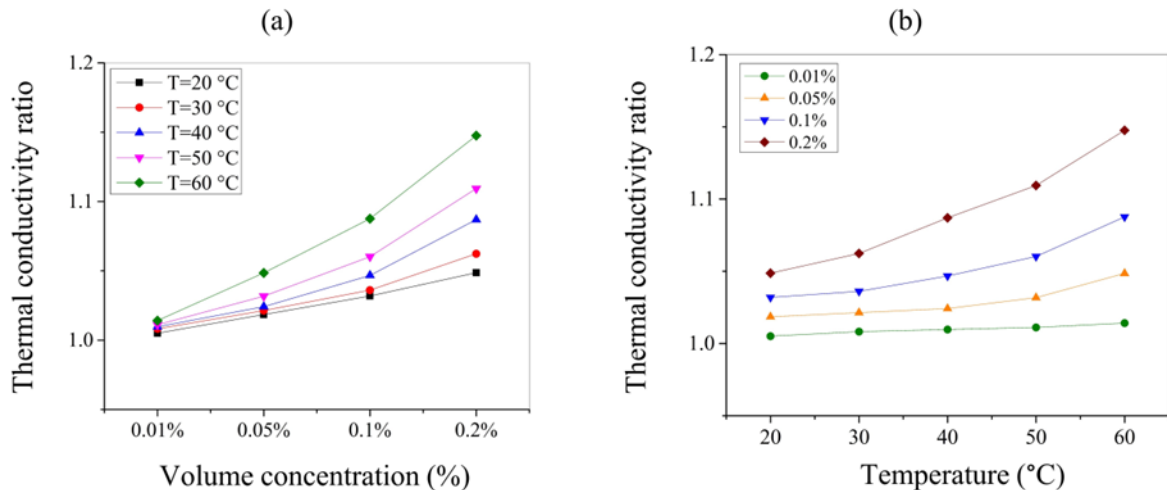


Fig. 3.22. TCR of HNF with (a) different temperatures at various VCs (b) VC at different temperatures

Moreover, the change in TCR with VC is greater at higher temperatures. In addition, the effect of temperature on TCR is more obvious at greater VC. For better understanding, Fig. 3.23 display the TCE with temperature and VC. Based on these figures, TC increases by over 14.4% at 0.2% VC and 60 °C. The increase in TC is caused by kinetic energy and Brownian motion

and the increase in interactions between nanoparticle additives. Temperature increased the collisions between molecules and suspended particles in the base fluid, thus enhancing TC.

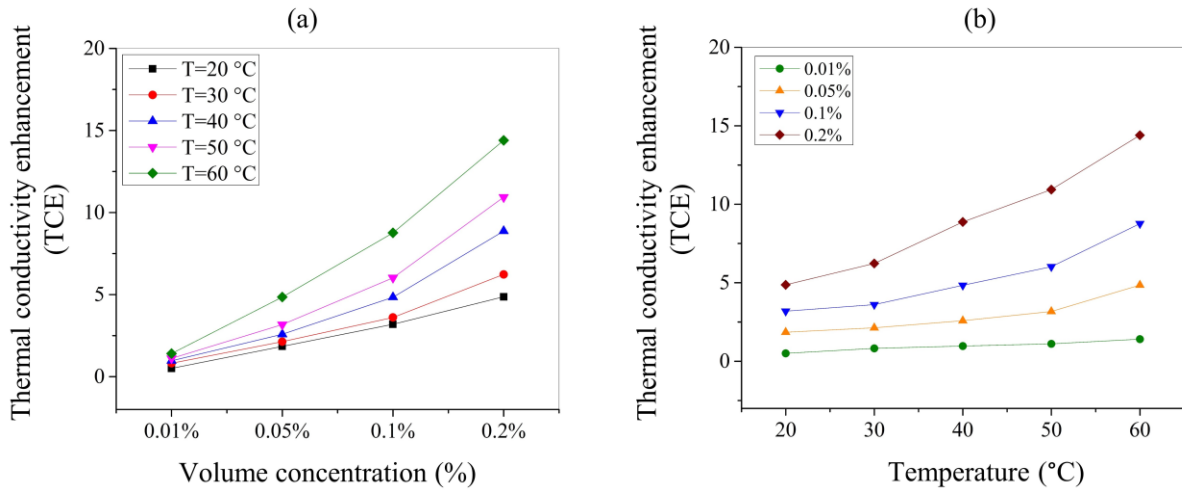


Fig. 3.23. TCE of HNF with (a) VC (b) Temperature

Experimental results showed that TC was improved by increasing the VC and temperature. Moreover, at higher temperatures, the variations in TCR with VC were more than at lower temperatures. Therefore, based on the new experimental data obtained in this work, an empirical correlation was obtained to predict the TC of the presently available HNF. Fig. 3.24 shows the TCR between the current experimental results and the correlation at different temperatures and VC, with  $R^2=0.9791$ .

$$TCR = 0.9994 + 0.05436 \varphi + 0.00012 T - 0.4568 \varphi^2 + 0.01178 \varphi T. \quad (3.38)$$

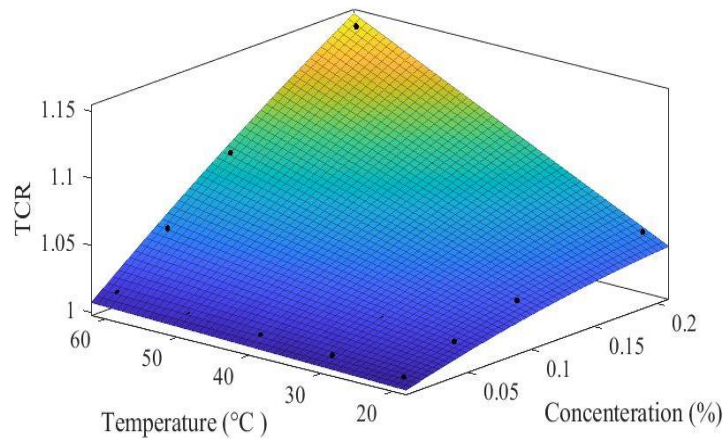


Fig. 3.24. TCR comparisons for different temperatures and VC

### 3.4.2 Effect of temperature on viscosity

HNF viscosity was measured using a Fungilab viscometer for a temperature range of 20 to 60 °C. The variations in HNF viscosity as a function of nanoparticle volume concentration and temperature are represented in Fig. 3.25. The viscosity of the NF decreased when the temperature was increased from 20 °C to 60 °C at the constant VC. At =0.2%, the viscosity decreased by 58.35%, from 0.99 mP.s to 0.412 mP.s, while the temperature increased from

20 °C to 60 °C. Increases in temperature reduce viscosity due to decreased adhesion forces and Brownian motion. However, the NF viscosity increased as the number of suspended particles increased.

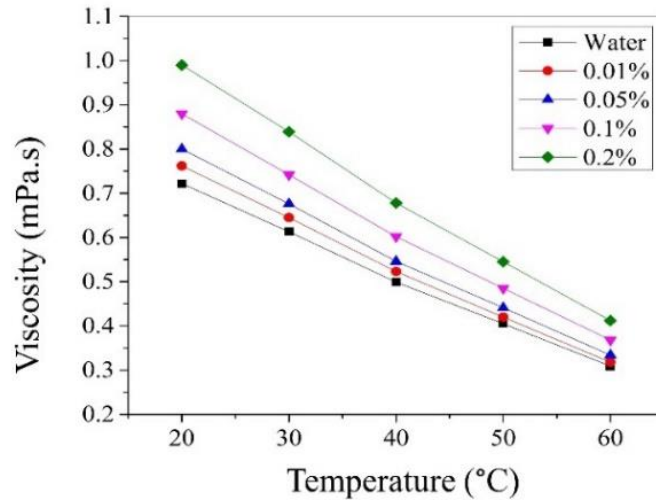


Fig. 3.25. The viscosity at different temperatures and VCs

At  $\varphi=0.1\%$ , the temperature increased from 20 °C to 60 °C, while the viscosity decreased by 58.1% from 0.88 mP.s to 0.368 mP.s. At  $\varphi=0.05\%$ , the temperature increased from 20 °C to 60 °C, while the viscosity decreased by 58.2% from 0.8 mP.s to 0.334 mP.s. At  $\varphi=0.01\%$ , the temperature increases from 20 °C to 60 °C, while the viscosity decreased by 58% from 0.726 mP.s to 0.318 mP.s. The decrease in viscosity caused by the increased temperature can be attributed to adhesion forces, intermolecular distance and Brownian motion. To understand the viscosity variations at different temperatures, we determined the NF RV by using Eq. (3.39) at different temperatures as follows:

$$RV = \left[ \frac{\mu_{nf}}{\mu_{bf}} \right], \tag{3.39}$$

where  $\mu_{bf}$  is the viscosity of base fluid, and  $\mu_{nf}$  is the viscosity of NF.

Fig. 3.26 shows the RV of the HNF at various temperatures and the VC of nanoparticles.

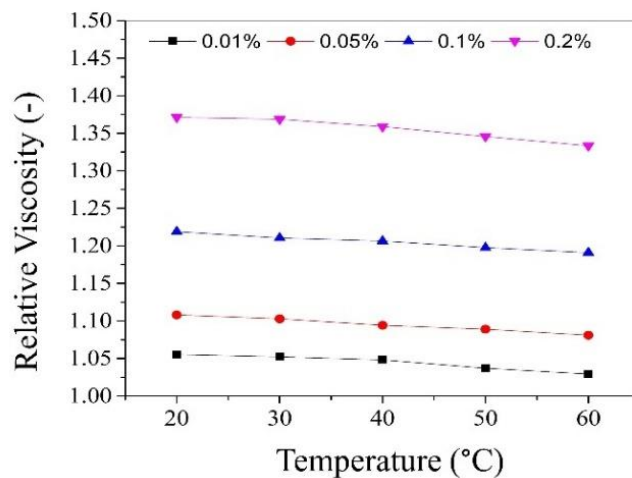


Fig. 3.26. RV at different temperatures and VCs



Fig. 3.27 shows the experimental results obtained for relative viscosity and plotted using the MATLAB curve fitting tool. Further, a new proposed correlation was obtained to measure the relative viscosity at differing VCs and temperatures, as shown in Eq. (3.40), with  $R^2=0.99$ .

$$RV = 1.044 + 1.889 \varphi - 0.0006066 T - 0.6786 \varphi^2 - 0.001685 \varphi T. \quad (3.40)$$

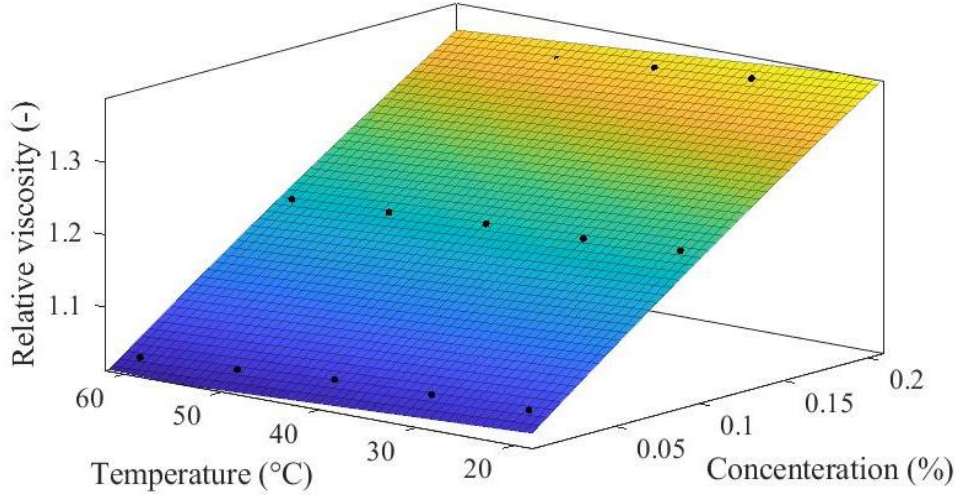


Fig. 3.27. RV at different temperatures and VC

### 3.4.3. Measurement of the density and the specific heat

NFs demonstrated enhanced the thermophysical properties of working fluid. In our research, the density, and the specific heat of HNFs have been calculated by mathematical equations and shown as follows:

$$\varphi_{\text{tot}} = \varphi_1 + \varphi_2, \quad (3.41)$$

$$\rho_{\text{hnf}} = \rho_f(1 - \varphi_{\text{tot}}) + \rho_{p1}\varphi_1 + \rho_{p2}\varphi_2. \quad (3.42)$$

$$c_{p,\text{hnf}} = \frac{\rho_f c_{p,f}(1 - \varphi_{\text{tot}}) + \rho_{p1} c_{p,p1} \varphi_1 + \rho_{p2} c_{p,p2} \varphi_2}{\rho_{\text{hnf}}}. \quad (3.43)$$

### 3.5. Preparations of graphene nanofluids

The graphene NFs were prepared by dispersing graphene nanoparticles in water with Gum Arabic surfactant. The two-step method, which is the most efficient and effective technique for producing NFs, was used. The solution was stirred for 1 hour, followed by 2 hours of ultrasonication. No sedimentation of particles was observed for 30 days. Four VCs were prepared: 0.01%, 0.05%, 0.1%, and 0.2% NFs. Table 3 shows the physical properties of G nanoparticles. Fig. 3.28 shows the XRD analysis Preparations of graphene NFs.

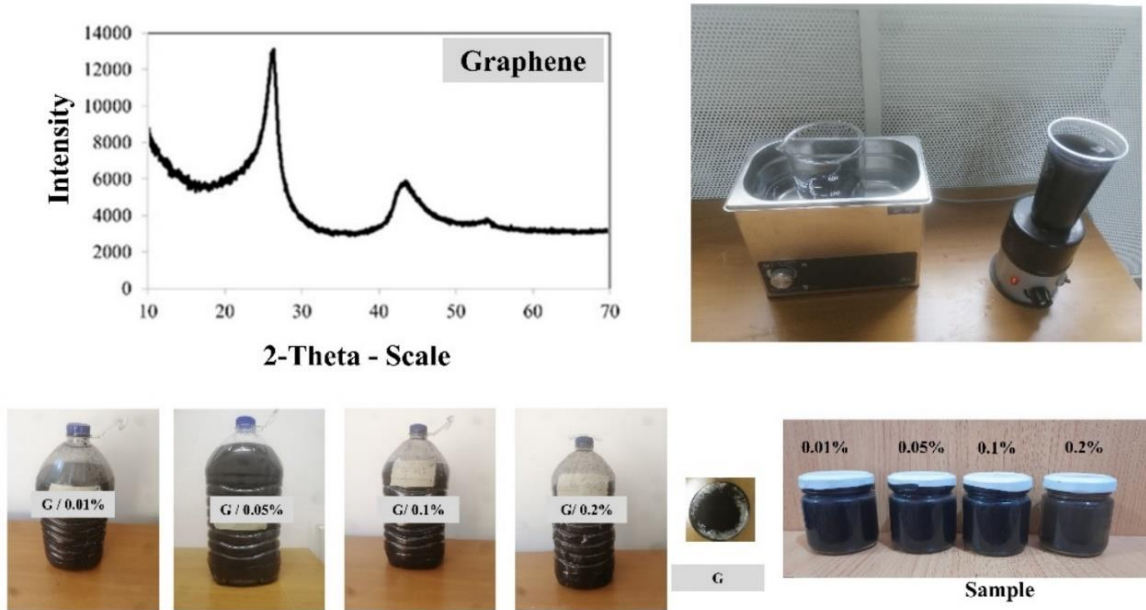


Fig. 3.28. XRD analysis and graphene nanofluid photo

### 3.5.1. Effect of temperature on thermal conductivity

The KD2 Pro thermal properties analyser (Decagon Devices, Inc., USA) was used to measure the TC. The KS-1 sensor needle, made of stainless steel with a 60 mm length and 1.3 mm diameter, closely matches an infinite line heat source, which causes the lowest sample disturbances during measurements.

TC was measured at five different temperatures ranging from 20 to 60 °C with a 10 °C tolerance. For each volume concentration, five temperature readings were taken every 15–20 minutes.

Fig. 3.29 shows that the TC of NF increases with particle concentrations and temperatures. TC of the 0.2% HNF was evaluated at 20 °C and was observed to be 0.66 W/m K, which is 10.7% higher than the TC of the base fluid (0.596 W/m K). Similarly, the TC of the 0.2% HNF was evaluated at 60 °C and was observed to be 0.75 W/m K, which is 17% higher than the TC of the base fluid (0.639 W/m K). The TC rises as a result of micro convection and Brownian motion of particles and base fluid.

Fig. 3.30 shows the variation of the TCR of HNF versus VC and temperature.

For better understanding, Fig. 3.31 display the TCE with temperature and VC. Based on these figures, TC increases by over 17% at 0.2% VCs and 60 °C.

### 3. Materials and methods

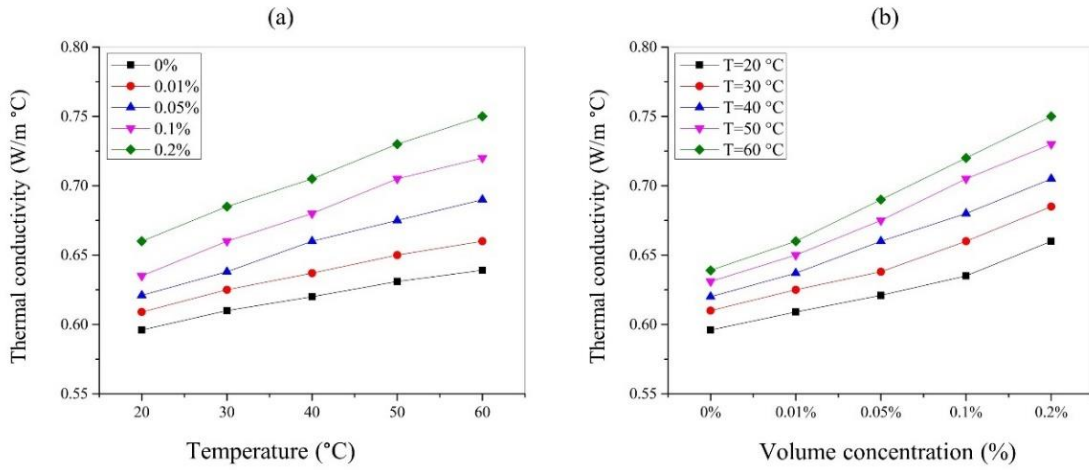


Fig. 3.29. TC of NF with (a) VCs at different temperatures, (b) Different temperatures at various VCs

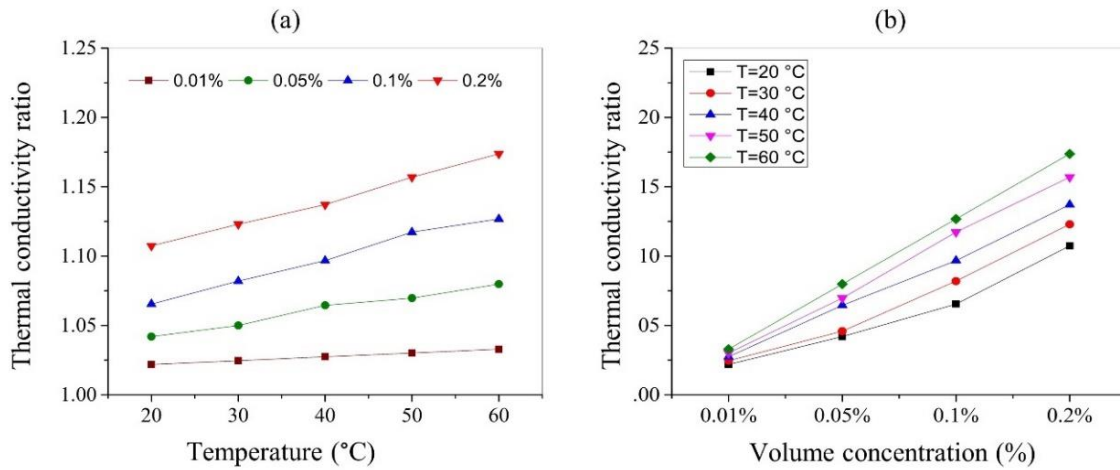


Fig. 3.30. TCR of NF with (a) different temperatures at various VCs (b) VC at different temperatures

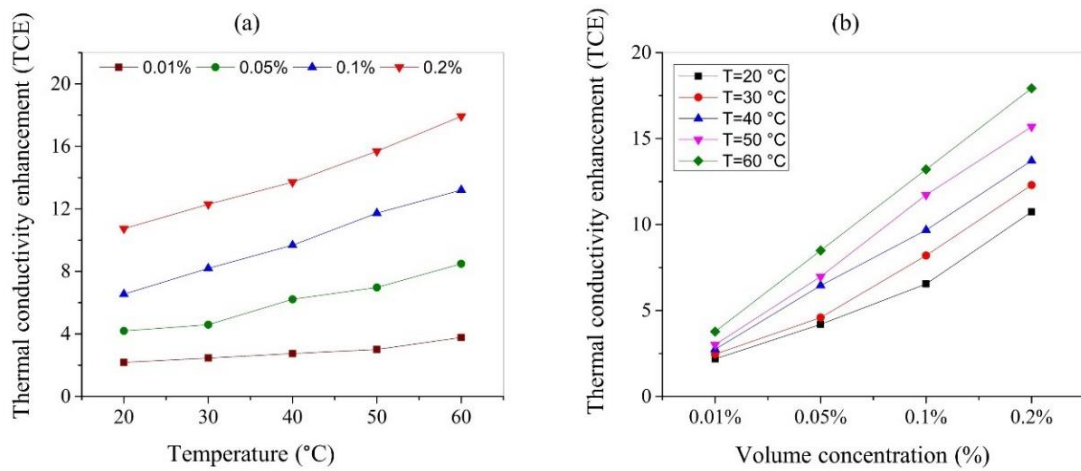


Fig. 3.31. TCE of NF with (a) VC (b) Temperature



Fig. 3.32. shows a comparison between the experimental results obtained and the proposed Eq. (3.44), with  $R^2=0.9881$ .

$$TCR = 0.9965 + 0.7082\phi + 0.0005184T - 1.835\phi^2 + 0.006788\phi T \quad (3.44)$$

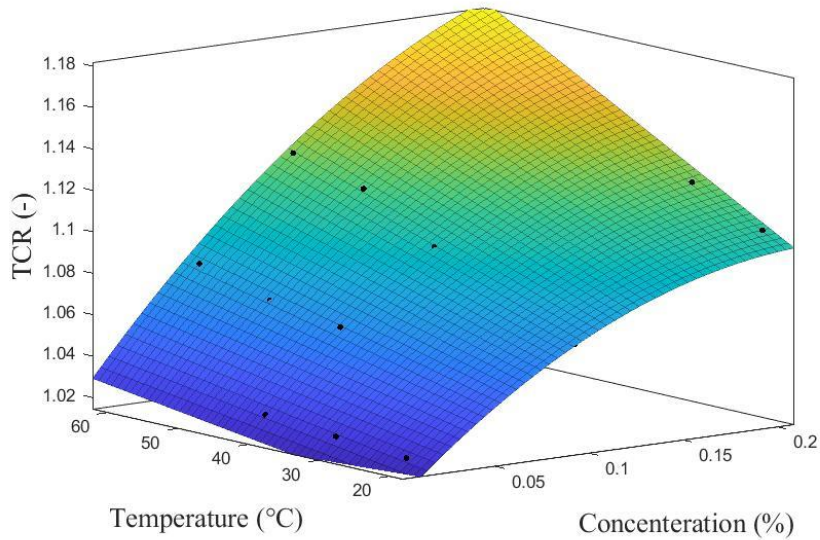


Fig. 3.32. TCR comparisons for different temperatures and VC

### 3.5.2. Effect of temperature on viscosity

NF viscosity was measured using a Fungilab viscometer for a temperature range of 20 to 60°C. The variations in NF viscosity as a function of nanoparticle volume concentration and temperature are represented in Fig. 3.33. The viscosity of the NF decreased when the temperature was increased from 20 °C to 60 °C at the constant VC. At =0.2%, the viscosity decreased by 59%, from 0.95 mP.s to 0.39 mP.s, while the temperature increased from 20 °C to 60 °C. Fig. 3.34 shows the RV of the graphene nanofluid at various temperatures and the VC of nanoparticles. Increases in temperature reduce viscosity due to decreased adhesion forces and Brownian motion.

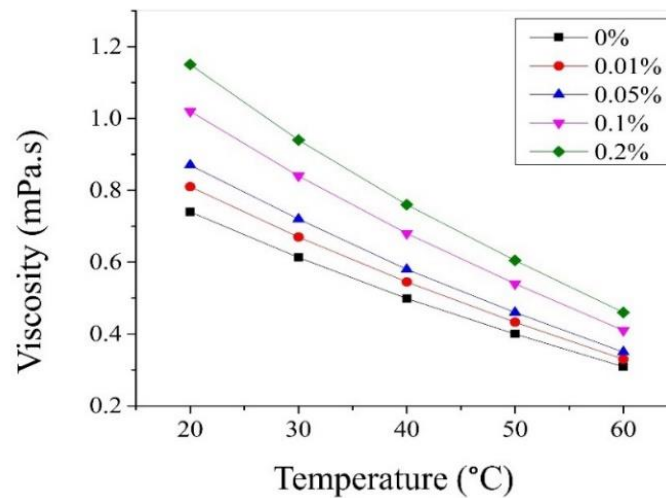


Fig. 3.33. The viscosity at different temperatures and VCs

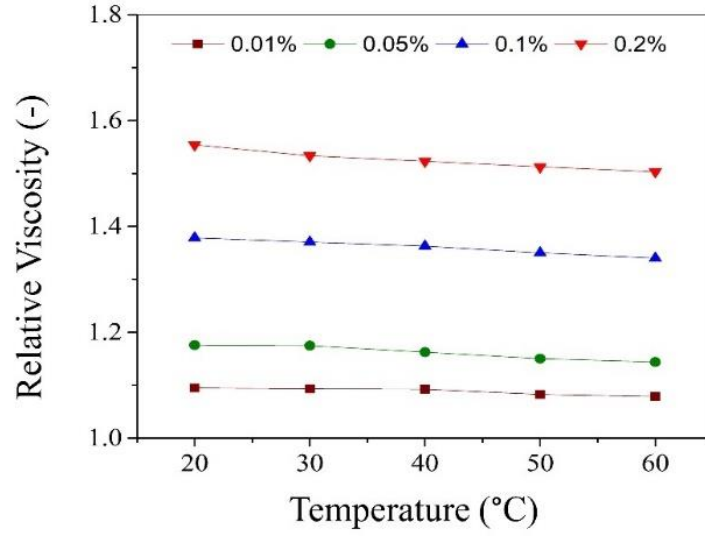


Fig. 3.34. RV at different temperatures and VCs.

Fig. 3.35 shows the experimental results obtained for relative viscosity and plotted using the MATLAB curve fitting tool. Further, a new proposed correlation was obtained to measure the relative viscosity at differing VCs and temperatures, as shown in Eq. (3.45), with  $R^2=0.9744$ .

$$RV = 1.059 + 3.647 \varphi - 0.0005436 T - 5.19 \varphi^2 - 0.003709 \varphi T. \quad (3.45)$$

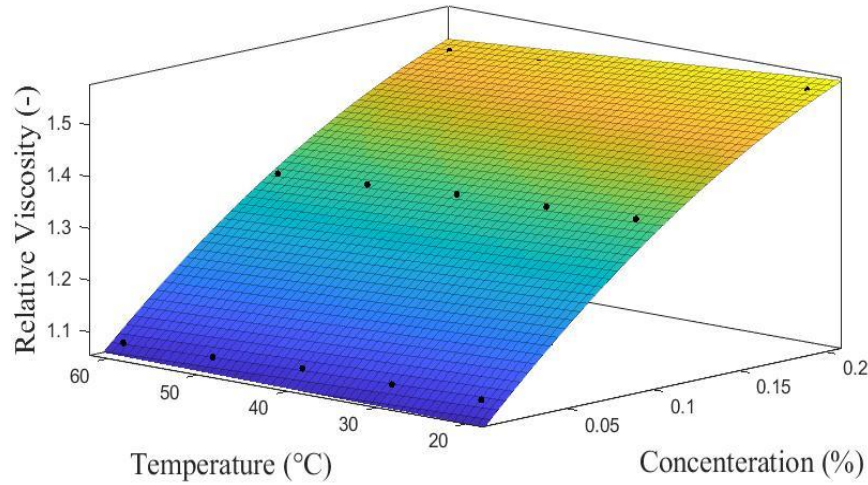


Fig. 3.35. RV at different temperatures and VC

### 3.5.3. Measurement of the density and the specific Heat

In this study, the density and specific heat of nanofluid have been calculated by mathematical equations. Graphene nanoparticles are mixed with water at different volume concentrations. The density and specific heat are given by the following:

$$\rho_{nf} = \rho_f(1 - \varphi) + \rho_p \varphi, \quad (3.46)$$

$$c_{p,nf} = \frac{\rho_{nf} c_{p,f}(1-\varphi) + \rho_p c_{p,p} \varphi}{\rho_{nf}}. \quad (3.47)$$

### 3.6. Preparing nanocoating

Matte acrylic coating is used in many solar applications due to its good absorbency of solar radiation and high heat resistance. Therefore, the iron oxide and graphene nanoparticles were added to the matte acrylic coating to enhance the absorption of solar radiation because of their dark black colour. The matte acrylic coating was emptied from the can to study its physical properties. Then, the coating fluid is put in a container of known volume and weight to measure the coating's density by dividing the weight by the volume. The volume concentration is evaluated according to Eq. (3.35) to determine the concentration of nanoparticles that should be added to equal 0.2% by volume concentration.

Nanoparticles of graphene- $\text{Fe}_3\text{O}_4$ /acrylic, which was used as the mixture's base fluid, were mixed in a 1:1 ratio to make the nanocoating. The fluid coating was put in a beaker (250 mL) and stirred for 0.5 hours. After that, it was mixed with ultrasonic waves for 0.5 hours to break up particles that were sticking together and spread them out evenly in the base fluid to make a stable nanocoating. For the coating to be uniform on the surface of the tube, we used the spraying method. An inlet was made in the coating can fill it with nanocoating and compressed air at 5 bar, and to achieve this air pressure, we used the tool used to fill car tyres and weld them to the can, as shown in Fig. 3.36.



Fig. 3.36. Mixing nanocoating and spray tool

### 3.7. Numerical analysis

Ansys Fluent 2020 software is used to develop and analyse the three-dimensional CFD thermal model of the single receiver tube. The heat flux value is considered uniform on the receiver tube's surface. Fig. 3.37 shows the simulation procedure that develops a CFD model.

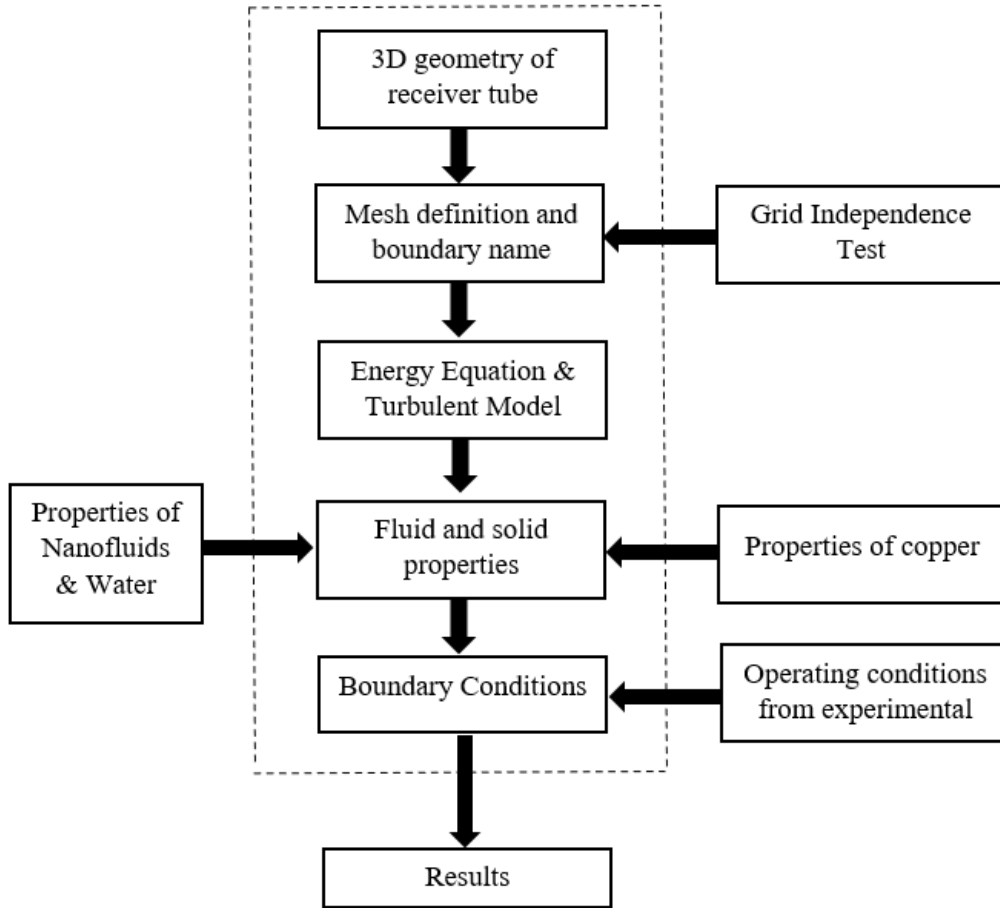


Fig. 3.37. Flow diagram for ANSYS Fluent simulation procedure

### 3.7.1 Assumptions

The following assumptions have been taken into consideration in the numerical analysis:

- In receiver tube numerical analysis with uniform heat flow, the outer surface has two parts.
- The heat transfer fluid used was water and nanofluid.
- Three-dimensional steady flow was adopted.
- Newtonian fluid.
- Incompressible fluid.
- Turbulent flow.

### 3.7.2. Governing equations

CFD is used in the numerical modelling of PTSCs, and the fluid flow may be laminar or turbulent for PTSCs. The CFD is also used to investigate the thermal-hydraulic performance of the HCE in general.

Continuity equation:

$$\frac{\partial \rho}{\partial t} + \nabla(\rho \vec{v}) = 0. \quad (3.48)$$

Momentum equation:

$$\frac{\partial}{\partial t}(\rho \vec{u}) + \nabla \cdot (\rho \vec{u} \vec{u}) = \nabla P + \nabla \cdot (\bar{\tau}) + \rho \vec{g}, \quad (3.49)$$

where:  $P$  is the pressure,  $\bar{\tau}$  is the stress tensor and  $\rightarrow \rho \vec{g}$  is the gravitational body force for unit volume. The stress tensor is given by:

$$\bar{\tau} = \mu[(\nabla \vec{u} + \nabla \vec{u}^T) - \frac{2}{3} \nabla \cdot \vec{u} I]. \quad (3.50)$$

Energy equation:

$$\frac{\partial}{\partial t}(\rho E) + \nabla \cdot (\vec{u} (\rho E + P)) = \nabla \cdot (k_{eff} \nabla T - \sum_j h_j J_j + (\bar{\tau}_{eff} \vec{u})) + S_h, \quad (3.51)$$

where:  $k_{eff}$  represents the effective thermal conductivity.

To accurately predict the performance of the PTSC during a CFD analysis, actual boundary conditions ought to be used. The crucial one among these boundary conditions is the heat flux on the HCE's absorber tube, which is usually the main thermal boundary condition in the analysis (Ravi Kumar and Reddy, 2009) (Muñoz and Abánades, 2011).

### 3.7.3. The receiver tube geometry

The top surface of the absorber tube receives direct solar irradiation, while the bottom of the tube surface, which faces the collector, receives concentrated radiation. It can be observed that the receiver tube receives different amounts of radiation between the upper and lower surfaces. As a result, the receiver tube's outer surface should be divided into two parts in order to apply a constant heat flux in each part. In addition, the receiver tube of the PTSC is symmetric on its vertical axis. For numerical modelling, only a half-section of the receiver tube is considered, as shown in Fig. 3.38.

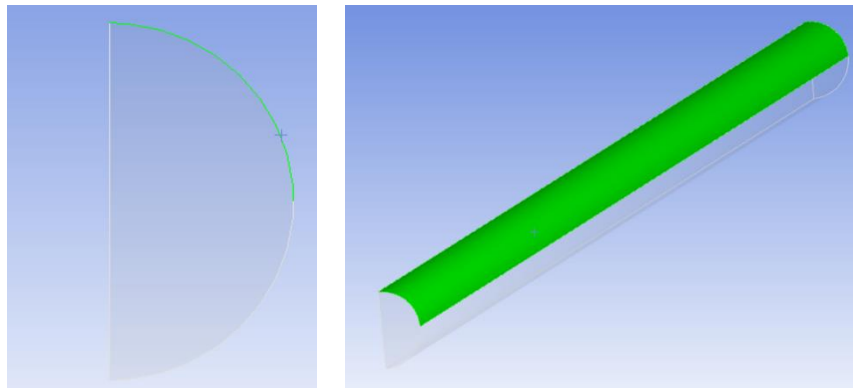


Fig. 3.38. the receiver tube Geometry

### 3.7.4. Mesh generation

Unstructured grids are in general successful for complex geometries. The receiver geometry is drawn in ANSYS, and the mesh of solid geometry is three-dimensional. The inlet and outlet sides used triangular mesh, and the volume mesh was a combination of triangular and tetragonal mesh. In this study, the number of mesh elements is (1208277), as seen in Fig. 3.39. ANSYS Fluent generates the solution using the finite volume method.

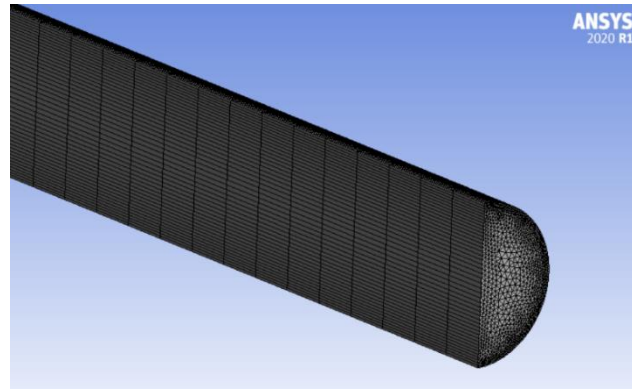


Fig. 3.39. Grid generation for PTSC receiver tube

### 3.7.5. Boundary conditions

The inlet temperature and mass flow rate of the working fluid at the receiver tube were measured during experiments and used as boundary conditions. The tube wall of the test section is subjected to a uniform heat flux, which varies depending on the receiver tube's circumference. The direct solar radiation on the tube was taken on the upper surface of the receiver tube. Whereas on the lower surface, the radiation multiplied by the concentration was taken with consideration of the effect of reflectance of collector. In addition, the inlet velocity is specified depending on Reynold's number of working fluid. The experiment is performed from 10:00 h to 15:00 h. The boundary condition names are listed in Table 3.5.

Table 3.5. Boundary name of receiver tube

Boundary name	condition
Inlet	Mass flow rate and inlet temperature
Outlet	Zero pressure gradient
Upper tube surface	Effective solar radiation
Lower tube surface	Uniform effective concentrated heat flux

### 3.7.6. Methodology

ANSYS Fluent generates the solution using the finite volume method. The RNG  $k$ - $\epsilon$  model with standard wall functions is used for the forced convection simulation in the tube. In the second-order upwind scheme, numerical solutions are obtained by solving energy equations for momentum, turbulent kinetic energy, turbulent dissipation rate and temperature. For pressure-velocity coupling, the SIMPLE algorithm is used to find a solution.

### 3.7.7 Grid independent study

In Fig. 3.37, the generated grids for the specified collector geometry can be seen. Six different grid configurations were examined to make sure that the numerical results were correct. The outcomes of the examination are displayed in Table 3.6. The errors for each variable are checked in the table, and very small changes in Nusselt number, especially after a mesh number of 1208277, are observed. Therefore, the best number of meshes was found to be 1208277 for more accurate and faster results.

Table 3.6. Grid-independent testing results

Case system	Grid element	Nu	Deviation (%)
Case 1	208089	33.7285	15.4333
Case 2	573804	39.8839	13.3435
Case 3	909468	46.0253	7.98675
Case 4	1153845	50.0203	6.22337
Case 5	1208277	53.3398	0.48723
Case 6	1560384	53.6013	Baseline

3.7.8. Model validation

Several Nusselt numbers and friction factor correlations were applied to validate the numerical model results. Heat transfer and fluid friction were validated. Water was used in all the correlations presented in Fig. 3.40: the Gnielinski (Cengel and Ghajar, 2011) given by Eq. (3.52), the Dittus–Boelter (Cengel and Ghajar, 2011) given by Eq. (3.53), the Pak–Cho (Pak and Cho, 1998) given by Eq. (3.54) and the Notter–Rouse (Notter and Sleicher, 1972) given by Eq. (3.55). The maximum deviation of the Nusselt number from the Pak–Cho, Dittus–Boelter, Notter–Rouse and Gnielinski correlations are 0.75%, 3.99%, 5.29%, and 9.66%, respectively.

$$Nu = \frac{\left(\frac{f}{8}\right)(Re-1000)Pr}{1+12.7\left(\frac{f}{8}\right)^{0.5}\left(\frac{3}{Pr^2-1}\right)}, \quad (3.52)$$

for  $3 \times 10^3 \leq Re \leq 5 \times 10^6$  and  $0.5 \leq Pr \leq 2000$ .

$$Nu = 0.023Re^{0.8}Pr^{0.4}. \quad (3.53)$$

$$Nu = 0.021Re^{0.8}Pr^{0.5}. \quad (3.54)$$

$$Nu = 5 + 0.01Re^{0.856}Pr^{0.347}. \quad (3.55)$$

The friction factor ( $f$ ) of water is compared in Fig. 3.41 to the correlations provided by Blasius (Blasius, 1913) by Eq. (3.56) and Petukhov (Petukhov, 1970) by Eq. (3.57). The maximum deviations of the friction factor from the Gnielinski and Blasius correlations were 3.76% and 4.33%, respectively, which is calculated using the following formula:

$$f = (0.79 \ln Re - 1.64)^{-2}, \quad (3.56)$$

For  $4 \times 10^3 \leq Re \leq 1 \times 10^5$

$$f = 0.316Re^{-0.25}. \quad (3.57)$$

In addition, the correlation inaccuracy in industrial applications is allowed to be 20% (Cheng et al., 2012), (Huang et al., 2017). Therefore, the results of the current study agree with the presented correlations.



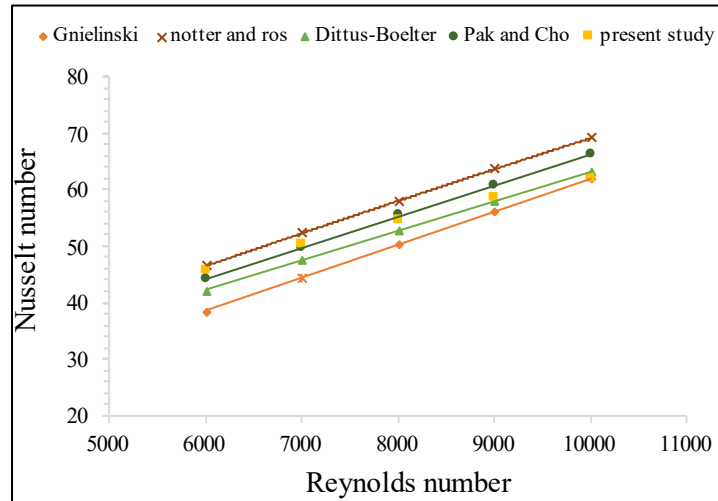


Fig. 3.40. Nu no. validation of W using literature correlation

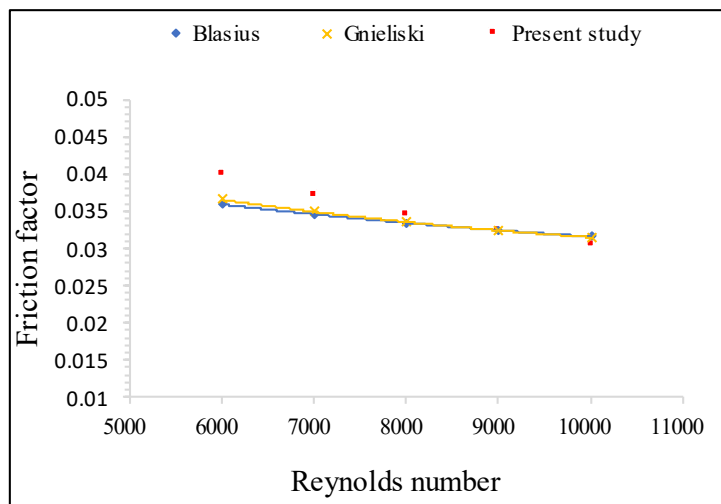


Fig. 3.41. Friction factor validation of W using literature correlation

### 3.8. Experimental procedure

Two similar PTSC were made and tested in Gödöllő city at the Hungarian University of Agriculture and Life Sciences, Hungary, in summer, 2022. Table 3.7 presents the model parameters and dimensions of the PTSC systems. Besides, Fig. 3.42 presents the hydraulic cycle that was used in the process of analysing the thermal efficiency of the PTSC system. Fig. 3.43 presents the experimental work done, which is the same as the ANSYS model.

Steps that were taken during the experiment include the following:

Step 1: The dust particles were removed from the absorber tube and reflector surface, as well as the collector was positioned in the direction of the sun no less than 30 mins before starting the experiment. The tank was filled with water, mono and HNFs.

Step 2: The reflector was set as indicated by the sun's position. The pump was switched ON about 20 mins before recording the first reading.



### 3. Materials and methods

Step 3: The system was operated at 9.30 am and the recording was taken from 10:00 a.m. to 15:00 p.m. every 10 min.

Step 4: The period between every reading was 10 mins. Therefore, the flow rate was at a steady state. Also, the heat transfer remained constant to make sure correct reading was recorded.

Step 5: Four different mass flow rates were recorded for the receiver tube.

Table 3.7 Specifications of the PTSC

Parameters	Specifications
Collector Length	1700 mm
Collector width	70 mm
Aperture area	1.19 m <sup>2</sup>
Rim angle	82°
Focal distance	20.5 mm
Outer diameter of glass cover tube	58 mm
Inner diameter of glass cover tube	43 mm
Outer diameter copper tube (single absorber tube)	12 mm
Inner diameter copper tube (single absorber tube)	10 mm
Outer diameter copper tube (Double absorber tube)	8 mm
Inner diameter copper tube (Double absorber tube)	7.5 mm
Outer diameter copper tube (Loop absorber tubes)	8 mm
Inner diameter copper tube (Loop absorber tubes)	7.5 mm
Outer diameter copper tube (Double absorber tube with flat plate)	8 mm
Inner diameter copper tube (Double absorber tube with flat plate)	7.5 mm
Tank	20 litter
Pump	375 W
Concentration ratio <sup>1</sup> (evacuated glass tube)	5.180
Concentration ratio <sup>2</sup> (single absorber tube)	18.568
Working Fluid	Nanofluids and Water
Thermocouple sensor	To measure temperature
Reflectance ( $\rho_c$ ) AS	80%
Reflectance ( $\rho_c$ ) SCF	99%
Absorptance ( $\alpha$ )	95%
Transmittance ( $\tau$ )	95%
Intercept factor ( $\gamma$ )	90%
Optical efficiency $\eta_o$ (SCF)	80.4%
Optical efficiency $\eta_o$ (AS)	64.98%
Sun Tracker	Single axis
flow rates	30 L/h, 60 L/hr, 90L/h, 120 L/h

### 3. Materials and methods

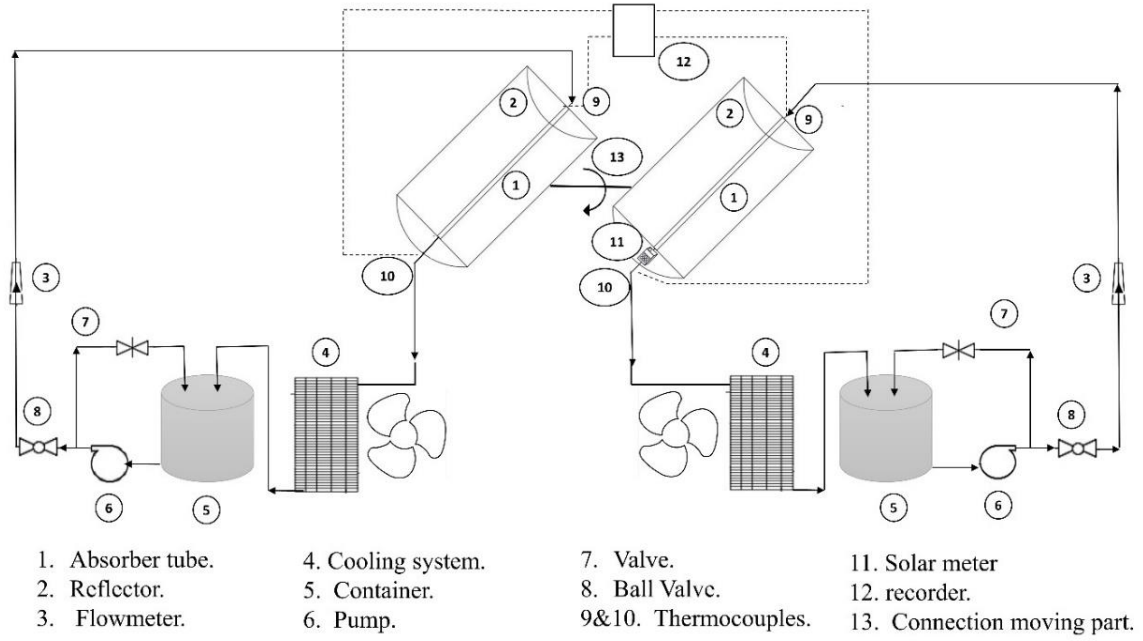


Fig. 3.42. Model demonstration

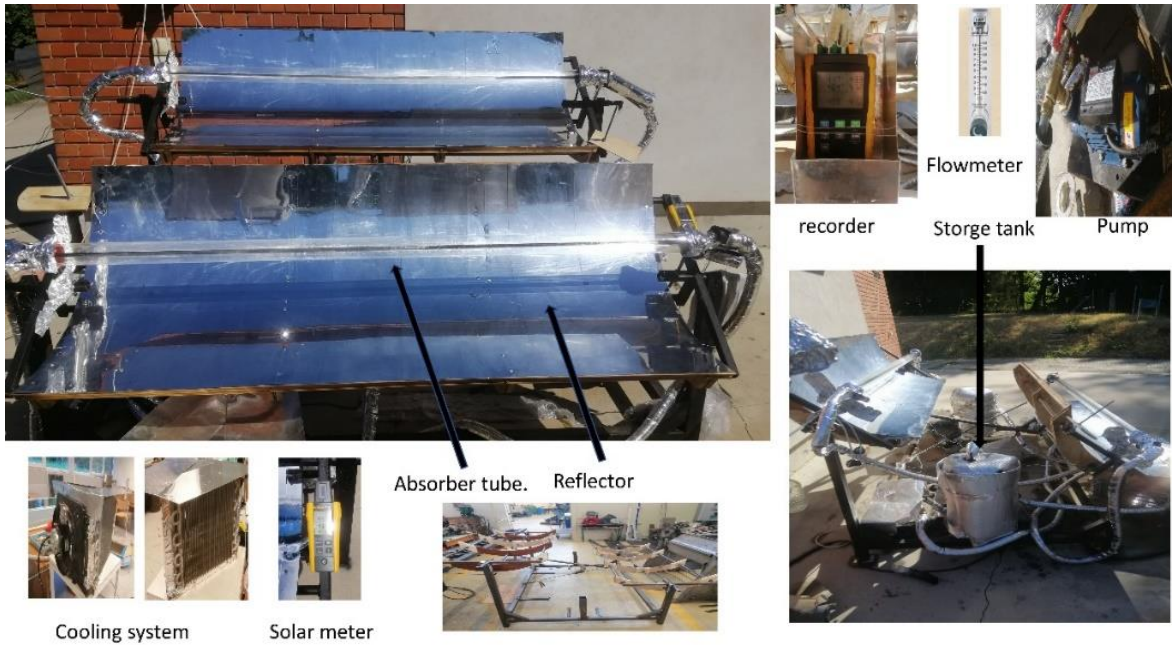


Fig. 3.43. Experimental setup

## 4. RESULTS

The performance of PTSC was investigated using theoretical and experimental observations, and the results, together with commentaries that highlight the novel scientific findings, are presented in this chapter. There are four main sections in this chapter: effects of reflecting surfaces; nano-coatings; mono and hybrid nanofluids; and novel designs of receiver tubes.

### 4.1. Similarity tests of each collector

The objective of this study is to design, develop, evaluate, and compare two identical PTSCs to decrease production costs and time. In the beginning, similarity tests of the two collectors were carried out using the aluminium reflective surface for each one to ensure that the two collectors worked with the same performance under the same conditions. The mass flow rate of 90 L/h was used to pass through the absorber tube. The experiments were carried out at the solar lab of the Hungarian University of Agriculture and Life Sciences from around 10:00 a.m. to 15:00 p.m. in the summer of 2022. The results showed that the average efficiencies of the upper and lower collectors were 21.382% and 21.436%, respectively. According to the test results, the average TE between collectors did not exceed 0.3%. According to experience, the two collectors work with performances close to each other.

### 4.2. Effect of reflective surface on parabolic trough solar collector performance

The PTSC consists of a reflector surface in a parabolic shape that concentrates the solar radiation into a receiver tube that transports a working fluid. Aluminium is a high-reflectance material and the most common material used in solar reflectors. This study focuses on the effect of a refractive surface on the performance and efficiency of the PTSC. Two PTSC collectors with different reflecting surfaces were created: one from silver chrome film (SCF) and the other from Aluminium sheet (AS). In addition, all collectors used water as the base fluid. To determine which is better for applications, one uses AS and the other uses SCF in the PTSC. Furthermore, the comparison is made with different mass flow rates (30 L/h, 60 L/h, 90 L/h, and 120 L/h) with an evacuated glass tube in a U shape. The evacuated glass receiver comprises two borosilicate glass pipes, one open and the other closed. Thus, the absorbed solar radiation was converted to heat and then transmitted to the copper tube, where the heat was then transferred to the fluid. The experiments were done at the Hungarian University of Agriculture and Life Sciences from 10:00 to 15:00 on July 22. Fig. 4.1 shows the experimental data collected on solar radiation and temperatures (ambient, inlet, and outlet temperatures). Further, the temperature difference decreased as the flow rate through the absorber tube increased.

The heat removal factor is represented by the ratio of the actual to the maximum heat transfer through the PTSC. The heat removal factor of water increased as the mass flow rate increased, as shown in Fig. 4.2. Thus, the amount of heat removal factor obtained for SCF is equal to 58.5%, 54.5%, 50.1%, and 43.1% for 120, 90, 60, and 30 L/h mass flow rates, respectively. Moreover, the amount of heat removal factor obtained for AS was 46%, 35.4%, 28.9%, and 24.9% for 120, 90, 60, and 30 L/h mass flow rates, respectively. Table 4.1 presents the thermal efficiency equations, and their heat removal factors for SCF and AS with different mass flow rates.

## 4. Results

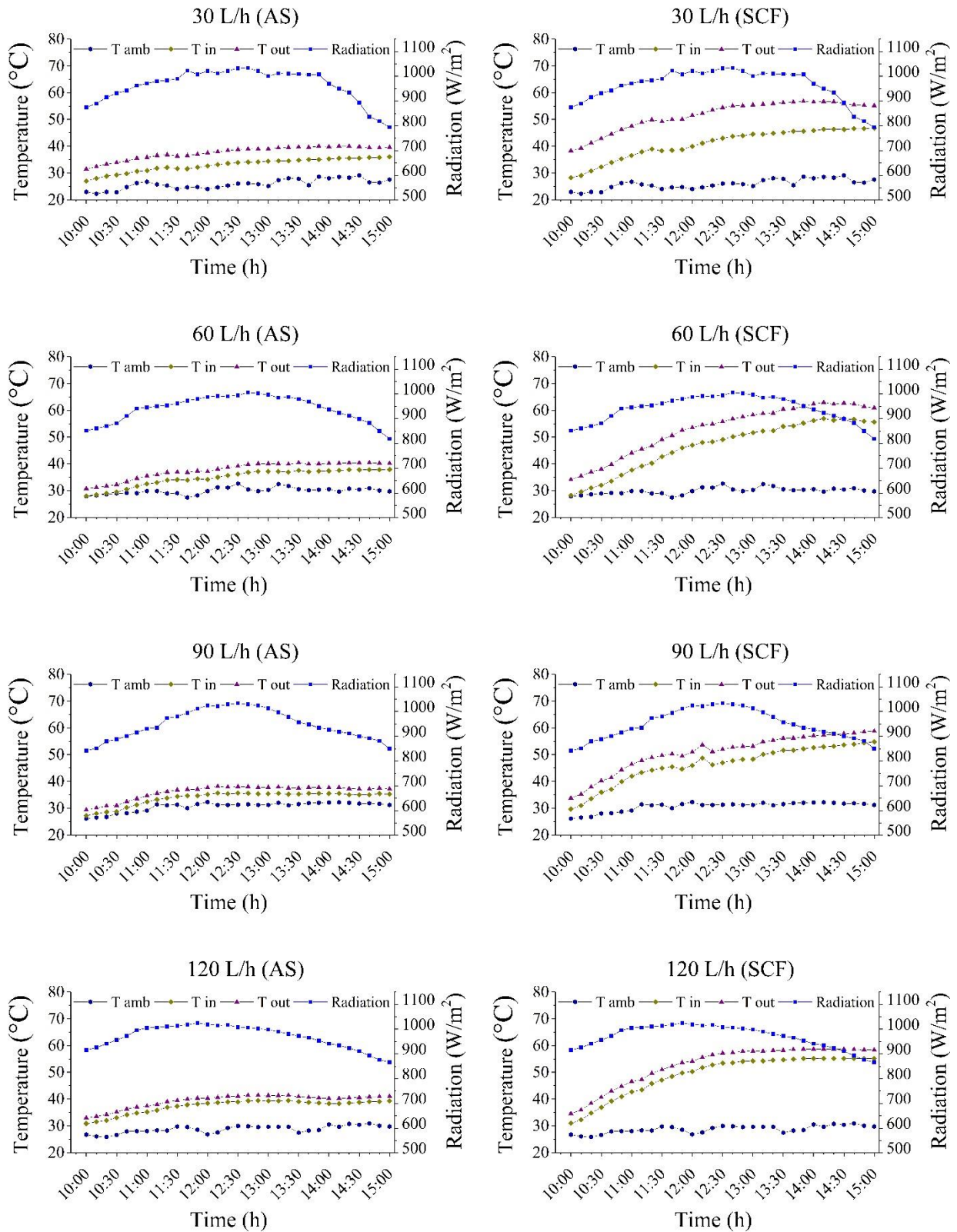


Fig. 4.1. Solar direct irradiance, ambient temperature, inlet temperature, and outlet temperature for SCF and AS

#### 4. Results

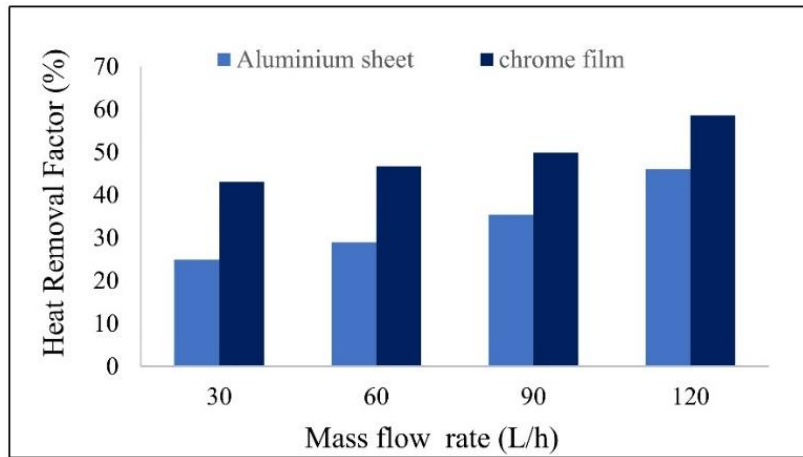


Fig. 4.2. Heat removal factor for SCF and AS

Table 4.1. Model equations of PTSC efficiency for SCF and AS at different mass flow rates

Mass Flow Rate (L/h)	Equation of efficiency	R <sup>2</sup>	F <sub>r</sub>
30 (Al)	$\eta_{th} = 16.174 - 282.89 \left( \frac{T_{in} - T_{amb}}{I_b} \right)$	0.9472	24.9
30 (SCF)	$\eta_{th} = 34.700 - 141.660 \left( \frac{T_{in} - T_{amb}}{I_b} \right)$	0.9665	43.1
60 (Al)	$\eta_{th} = 18.836 - 217.57 \left( \frac{T_{in} - T_{amb}}{I_b} \right)$	0.9518	28.9
60 (SCF)	$\eta_{th} = 40.301 - 65.42 \left( \frac{T_{in} - T_{amb}}{I_b} \right)$	0.99	50.1
90 (Al)	$\eta_{th} = 23.035 - 493.54 \left( \frac{T_{in} - T_{amb}}{I_b} \right)$	0.9635	35.4
90 (SCF)	$\eta_{th} = 43.859 - 105.36 \left( \frac{T_{in} - T_{amb}}{I_b} \right)$	0.9646	54.5
120 (Al)	$\eta_{th} = 29.907 - 618.56 \left( \frac{T_{in} - T_{amb}}{I_b} \right)$	0.9627	46
120 (SCF)	$\eta_{th} = 47.110 - 130.97 \left( \frac{T_{in} - T_{amb}}{I_b} \right)$	0.9326	58.5

The useful heat from the PTSC can be calculated using Eq. (3.8) based on the temperature difference in the fluid that flows through the receiver tube. At the beginning of the experiment, the useful heat gain is low as the solar radiation is low, then increased as time passed until reaching the peak values at noon; after that, it starts to decrease. Therefore, the solar irradiation rate affects the energy collected. In addition, the useful heat gain increased with an increased mass flow rate. Fig. 4.3 shows the useful energy with time in all AS cases, while Fig. 4.4 shows the useful energy with time in all SCF cases.

## 4. Results

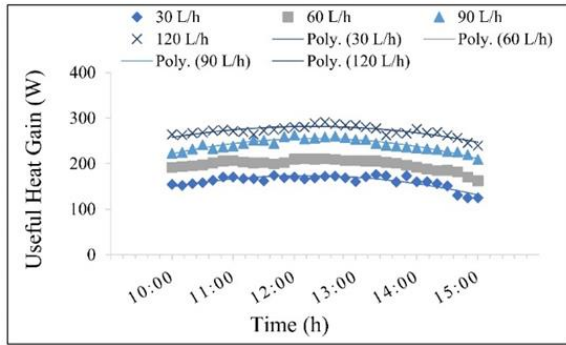


Fig. 4.3. Useful heat gain for AS

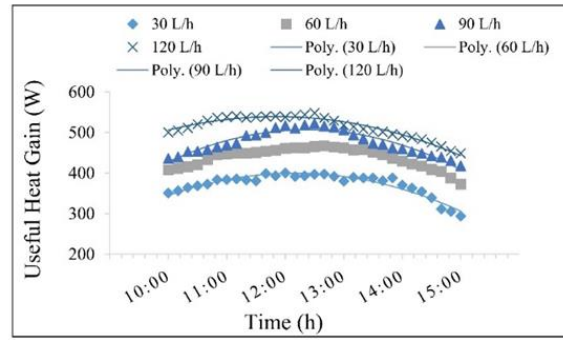


Fig. 4.4. Useful heat gain for SCF

The experiments were carried out at four mass flow rates ranging from 30 to 120 L/h. The collector's efficiency for each mass flow rate is presented as a function of  $T^*$ . Fig. 4.5 compares aluminium sheets' thermal efficiencies with different flow rates. Obviously, TE values obtained have increased as the mass flow rate increased. According to the experimental results, the maximum TE with AS was obtained at 120 L/h, 90 L/h, 60 L/h, and 30 L/h mass flow rates, reaching 27%, 22.84%, 18.9%, and 14.86%, respectively. Fig. 4.6 presents the thermal efficiencies obtained using SCF with different flow rates as a function of  $T^*$ . the maximum TE with SCF was obtained for 120, 90, 60, and 30 L/h mass flow rates and reached 46.84%, 43.49%, 40.26%, and 33.68%, respectively. According to the results, the thermal performance of the PTSC using SCF is better than AS

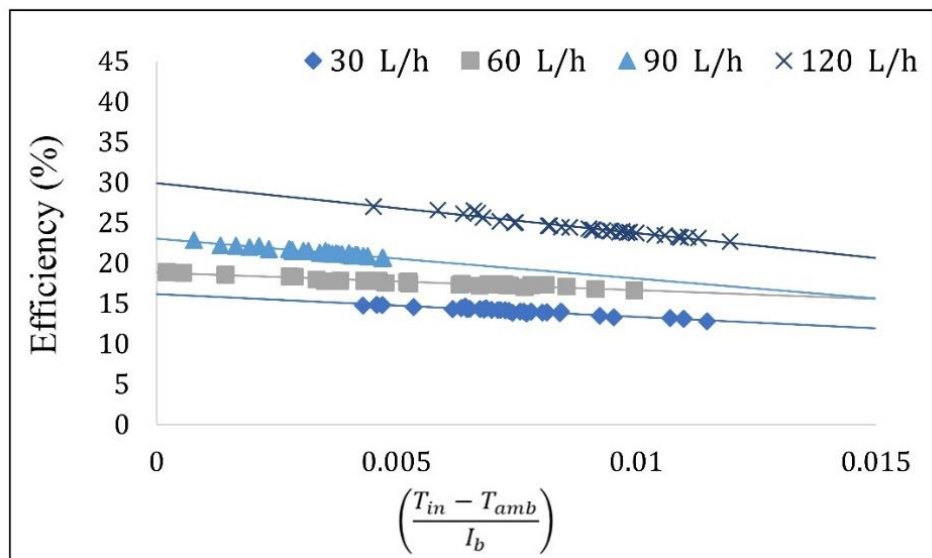


Fig. 4.5. TE and heat loss parameter( $T^*$ ) at different mass flow rates of AS



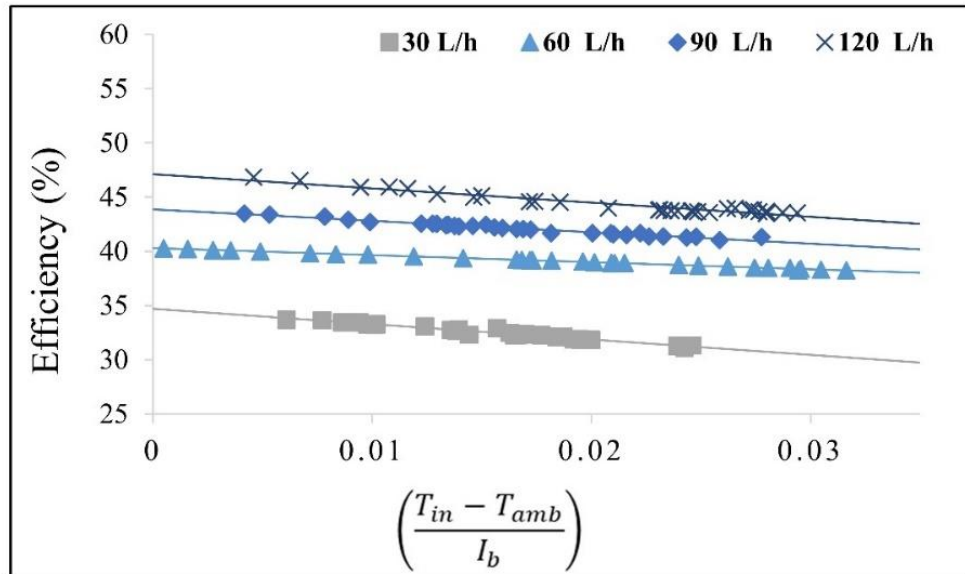


Fig. 4.6. TE and the heat loss parameter at different mass flow rates of SCF

### 4.3. Effect of receiver tube coating on parabolic trough solar collector performance

In typical PTSCs, the receiver is essentially one of the main and most important components of the collector. Therefore, the coating lifetime should be stable to enhance efficiency and reduce maintenance costs. Coatings are used to enhance the performance of absorbers in terms of quality, efficiency, maintenance, and cost. The coatings are differed as there are no uniformly perfect materials for various applications, working conditions, and materials. This study focuses on the effect of a receiver tube coating on the performance and efficiency of the PTSC.

Therefore, the coating method must be chosen based on the application area, availability, and cost criteria. Spray coating is a reliable method for getting good properties, highly adhesive coatings, and anticorrosive coatings over the copper tube. The sputtering coating method has a certain significance for depositing films on the substrate and is an economical and environmentally friendly method. Two PTSCs with different coatings were created: one with a nanocoating (NC) and the other with a matte coating (MC). In addition, the PTSC comparison is made with different mass flow rates (30, 60, 90, and 120 L/h). The nanocoating was prepared as described in the Materials and Methods chapter, and a single evacuated absorber tube was used in the experiment.

The experiments were done at the Hungarian University of Agriculture and Life Sciences from 10:00 to 15:00 on July 22. Fig. 4.7 shows the experimental data collected on solar radiation and temperatures (ambient, inlet, and outlet temperatures). Further, the temperature difference decreased as the flow rate through the absorber tube increased.

## 4. Results

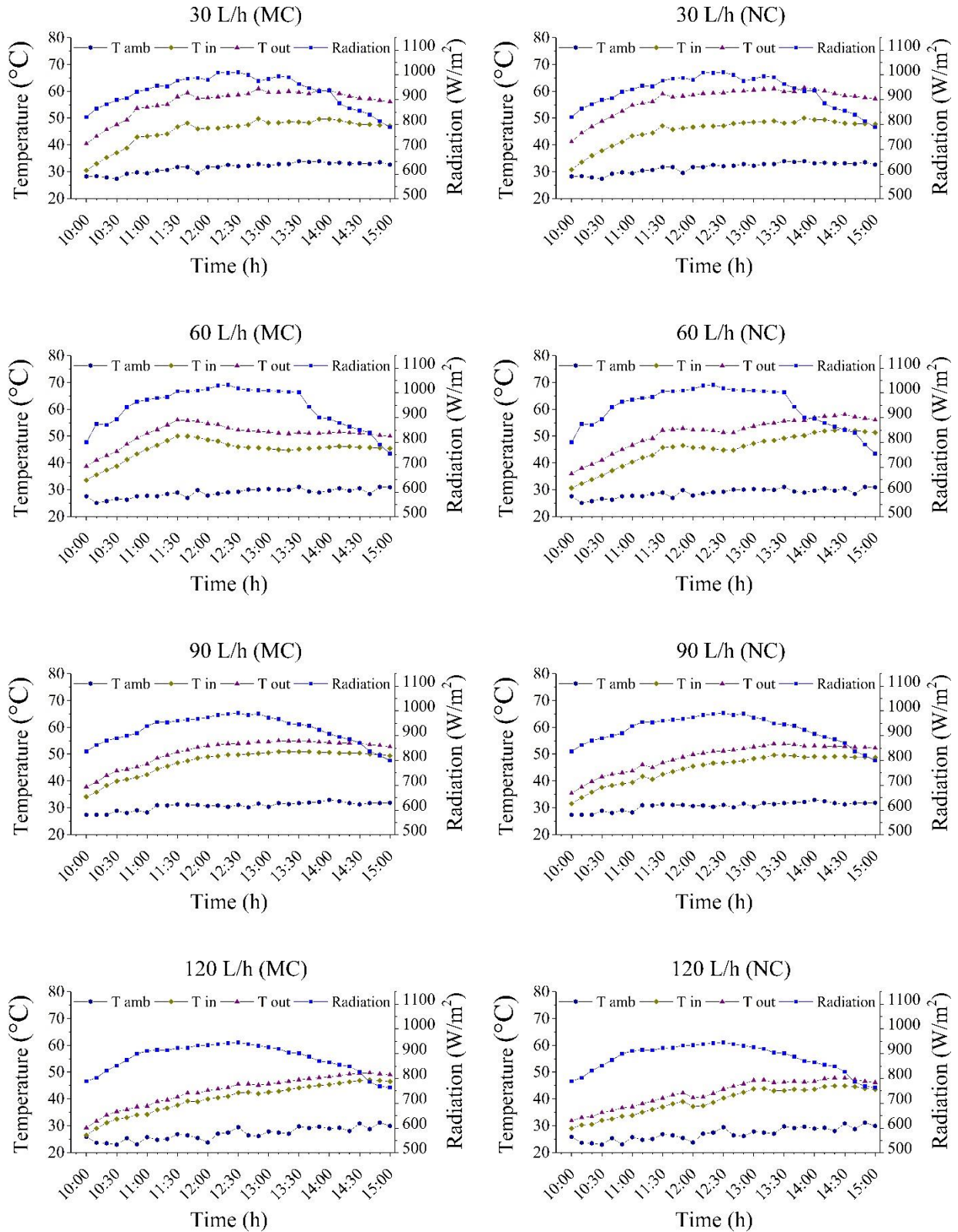


Fig. 4.7. Solar direct irradiance, ambient temperature, inlet temperature, and outlet temperature for MC and NC

The heat removal factor is represented by the ratio of the actual to the maximum heat transfer through the PTSC. The heat removal factor of water increased as the mass flow rate increased,



## 4. Results

as shown in Fig. 4.8. Thus, the amount of heat removal factor obtained for NC is equal to 52.7%, 51.1%, 49%, and 46.2% for 120, 90, 60, and 30 L/h mass flow rates, respectively. Moreover, the amount of heat removal factor obtained for MC equals 50.3%, 49%, 48.1%, and 43.8% for 120, 90, 60, and 30 L/h mass flow rates, respectively. Table 4.2 presents thermal efficiency equations, and their heat removal factors for NC and MC with different mass flow rates.

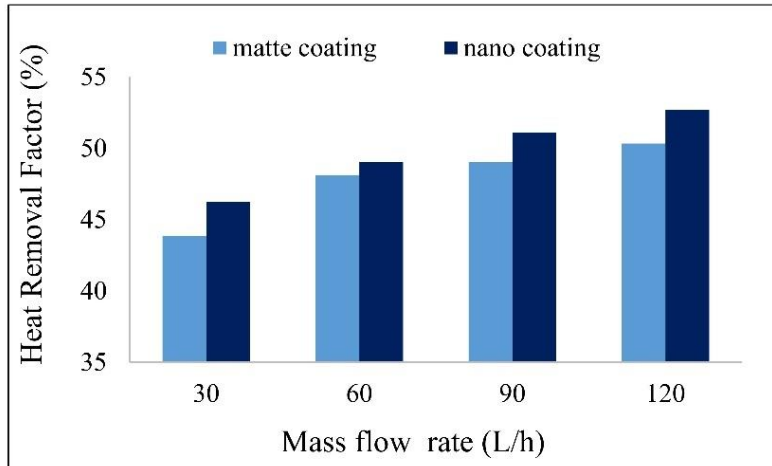


Fig. 4.8. Heat removal factor for NC and MC

Table 4.2. Model equations of PTSC efficiency for NC and MC at different mass flow rates

Mass Flow Rate (L/h)	Equation of efficiency	R <sup>2</sup>	F <sub>r</sub>
30 (MC)	$\eta_{th} = 35.27 - 101.7 \left( \frac{T_{in} - T_{amb}}{I_b} \right)$	0.995	43.8
30 (NC)	$\eta_{th} = 37.18 - 98.046 \left( \frac{T_{in} - T_{amb}}{I_b} \right)$	0.99	46.2
60 (MC)	$\eta_{th} = 38.706 - 184.1 \left( \frac{T_{in} - T_{amb}}{I_b} \right)$	0.997	48.1
60 (NC)	$\eta_{th} = 39.431 - 109.55 \left( \frac{T_{in} - T_{amb}}{I_b} \right)$	0.99	49.1
90 (MC)	$\eta_{th} = 39.485 - -131.57 \left( \frac{T_{in} - T_{amb}}{I_b} \right)$	0.996	49
90 (NC)	$\eta_{th} = 41.11 - 100.08 \left( \frac{T_{in} - T_{amb}}{I_b} \right)$	0.993	51.1
120 (MC)	$\eta_{th} = 40.474 - 72.322 \left( \frac{T_{in} - T_{amb}}{I_b} \right)$	0.98	50.3
120 (NC)	$\eta_{th} = 42.395 - 117.7 \left( \frac{T_{in} - T_{amb}}{I_b} \right)$	0.989	52.7

## 4. Results

The useful heat from the PTSC can be calculated using Eq. (3.8) based on the temperature difference in the fluid that flows through the receiver tube. At the beginning of the experiment, the useful heat gain is low because the solar radiation is low, then it starts to increase as time passes until reaching the peak values at noon; and then started to decrease. Therefore, the solar irradiation rate affects the energy collected. In addition, the useful heat gain increases with an increased mass flow rate. Fig. 4.9 shows the useful energy with time in all MC cases. Fig. 4.10 shows the useful energy with time in all NC cases.

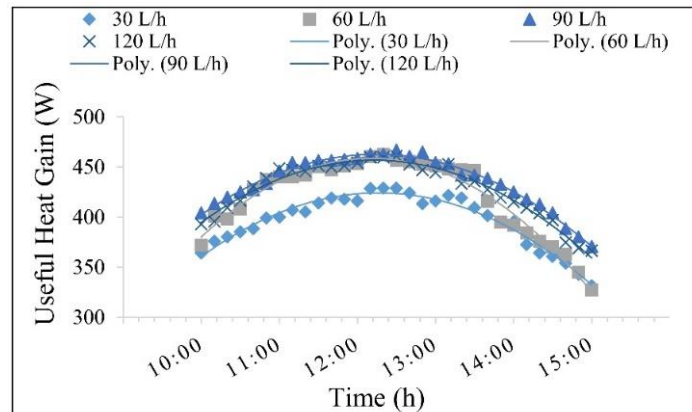


Fig. 4.9. Useful heat gain for MC

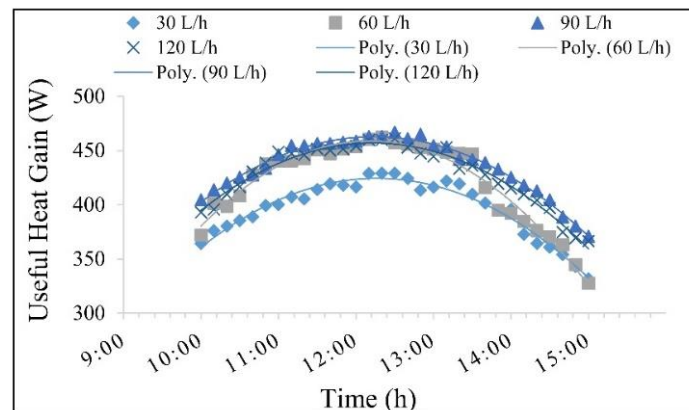


Fig. 4.10. Useful heat gain for NC

The experiments were carried out at four mass flow rates ranging from 30 L/h to 120 L/h. The collector's efficiency for each mass flow rate is presented as a function of  $T^*$ . Fig. 4.11 compares MC thermal efficiencies with different flow rates. Obviously, TE values obtained had increased as the mass flow rate increased. According to the experiment results, the maximum TE with MC was obtained for 120, 90, 60, and 30 L/h mass flow rates and reached 40.37%, 38.39%, 37.27%, and 34.98%, respectively. Fig. 4.12 presents the thermal efficiencies obtained using NC with different flow rates as a function of  $T^*$ . The maximum TE with NC was obtained for 120, 90, 60, and 30 L/h mass flow rates and reached 41.58%, 40.6%, 39%, and 36.88%, respectively. Furthermore, coatings should be thermally stable because they experience rapid and cyclic temperature variations during operation. According to the results, the thermal performance of the PTSC using NC is better than MC. NC showed a remarkable

enhancement of TE by decreasing thermal losses. Finally, the NC is more effective at improving system performance.

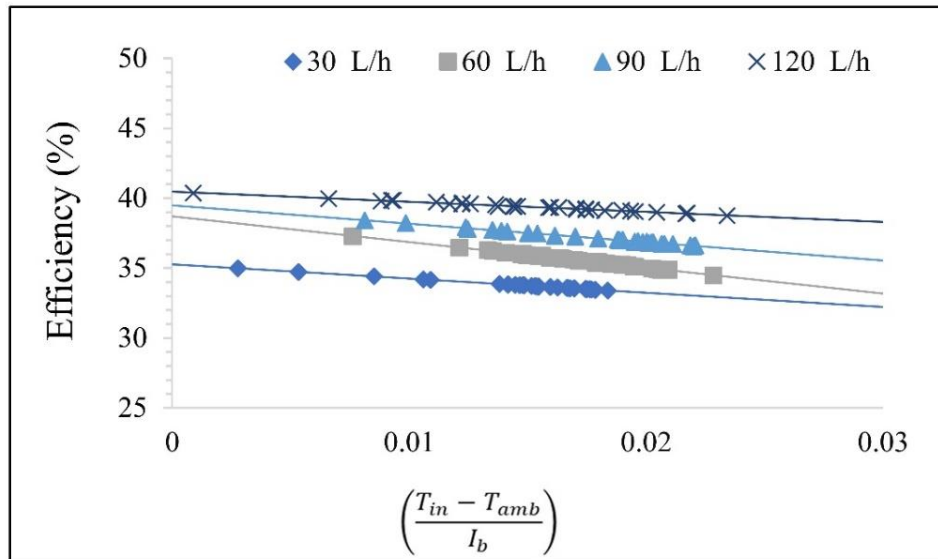


Fig. 4.11. TE and heat loss parameter at different mass flow rates of MC

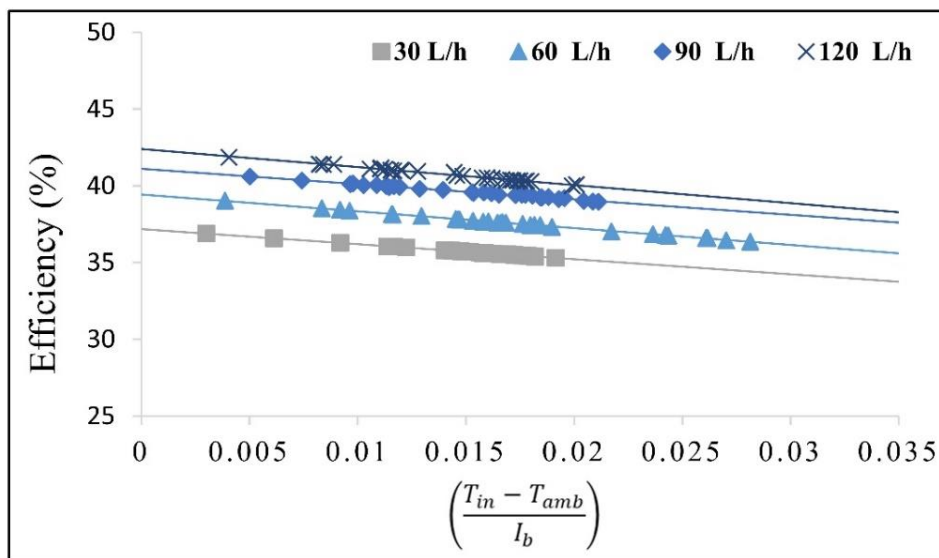


Fig. 4.12. TE and the heat loss parameter at different mass flow rates of NC

#### 4.4. Test case hybrid nanofluid

This study involved manufacturing a prototype of PTSC that would be used to determine the efficiency of a working fluid made of graphene and  $\text{Fe}_3\text{O}_4$  nanoparticles suspended in a water as based nanofluid. Before the experiment, a similarity test is done to make sure that the two collectors give the same results. Two identical PTSCs at a 120 L/h flow rate were examined with water under the same conditions. The average efficiencies for the lower and upper collectors were 39.798% and 39.842%, respectively. As a result, the two collectors perform similarly in the same weather conditions. The experiments were carried out with graphene– $\text{Fe}_3\text{O}_4$ /water HNFs in different concentrations (0.01%, 0.05%, 0.1%, and 0.2%) with a mass

## 4. Results

flow rate of 120 L/h. Furthermore, the TE of PTSC will be evaluated and examined at different concentrations. The test was performed at a mass flow rate of 120 L/h, and the required measurements were obtained and recorded. Experiments were carried out at the solar lab of the Hungarian University of Agriculture and Life Sciences from around 10:00 to 15:00 in the summer of 2022. Fig. 4.13 represents the experimental data that were recorded for temperatures and solar radiation.

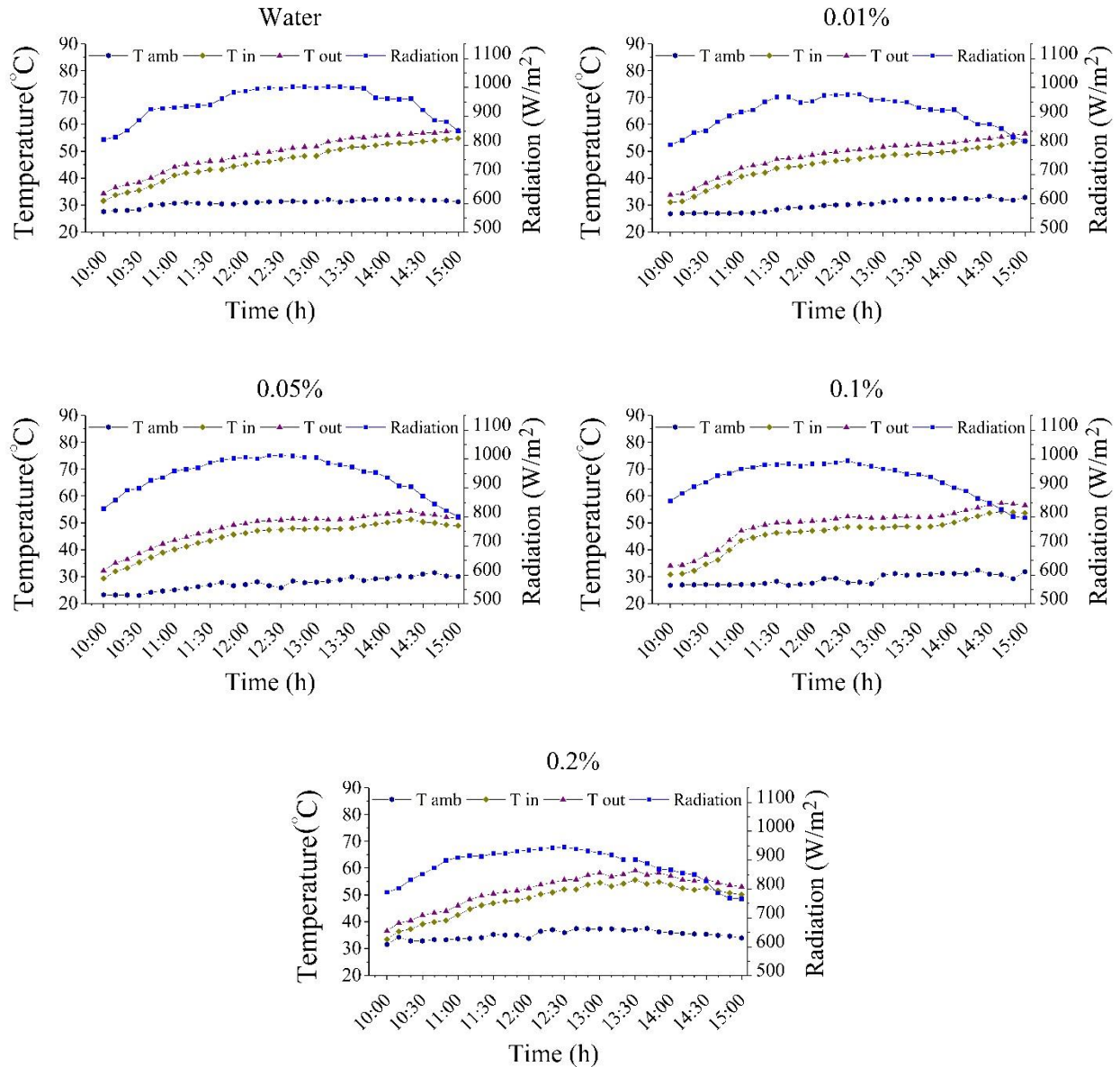


Fig. 4.13. Test results for water, 0.01% HNF, 0.05% HNF, 0.1% HNF and 0.2% HNF

The heat removal factor represents the ratio of the actual useful energy to the maximum useful gain. Fig. 4.14 shows that the heat removal factor of HNF was higher than that of water. As observed, the heat removal factor increased as the concentration of nanoparticles increased. According to the results, the heat removal factor of the graphene-Fe<sub>3</sub>O<sub>4</sub> HNF was 57.7%, 56.3%, 53.9%, and 52.2% for 0.2%, 0.1%, 0.05%, and 0.01% VCs, respectively, while the heat removal factor with water was 51.4%. Table 4.3 shows the TE equations, and heat removal

## 4. Results

factors for water and HNF at different concentrations. At a 0.2% volume concentration of graphene-Fe<sub>3</sub>O<sub>4</sub>/water HNF, the heat removal factor reached the maximum value of 57.763%. In addition, the overall heat loss coefficient ( $U_L$ ) reached 3.886 W/m<sup>2</sup>K. For the base fluid (water), the heat removal factor reaches the minimum value of 51.4%. It's clear that the heat removal factors for graphene- Fe<sub>3</sub>O<sub>4</sub>/water HNF are higher than those for water for all examined volume concentrations. The increase in heat removal factor with increasing concentrations is due to the increased TC resulting from the increase in nanoparticle concentration.

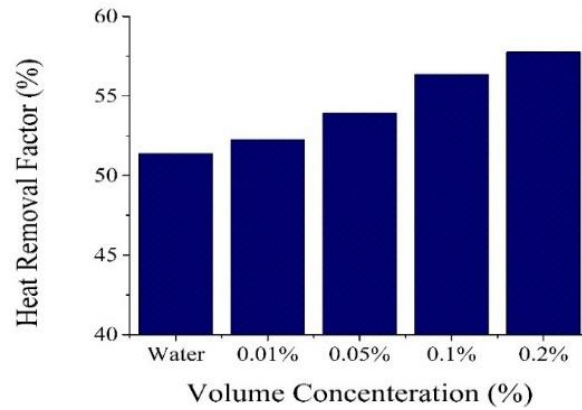


Fig. 4.14. Heat removal factors at different VCs and water

Table 4.3. Collector efficiency equations for W and HNFs

VCs	Equation of efficiency	R <sup>2</sup>	F <sub>r</sub>
Water	$\eta_{th} = 40.461 - 7.9912 \left( \frac{T_{in} - T_{amb}}{I_b} \right)$	0.9497	51.4
0.01%	$\eta_{th} = 41.131 - 29.888 \left( \frac{T_{in} - T_{amb}}{I_b} \right)$	0.9723	52.2
0.05%	$\eta_{th} = 42.46 - 54.534 \left( \frac{T_{in} - T_{amb}}{I_b} \right)$	0.9621	53.9
0.1%	$\eta_{th} = 44.373 - 19.443 \left( \frac{T_{in} - T_{amb}}{I_b} \right)$	0.9535	56.3
0.2%	$\eta_{th} = 45.471 - 13.548 \left( \frac{T_{in} - T_{amb}}{I_b} \right)$	0.9610	57.7

The useful heat from the PTSC can be calculated using Eq. (3.8) based on the temperature difference in the fluid that flows through the receiver tube. At the beginning of the experiment, the useful heat gain is low since the solar radiation is low, then it started to increase with time until reaching the peak values at noon; after that, it was decreasing. Therefore, the solar irradiation rate affects the energy collected. In addition, the useful heat gain increased with an increased volume concentration. Fig. 4.15 shows the useful energy with time in all cases.

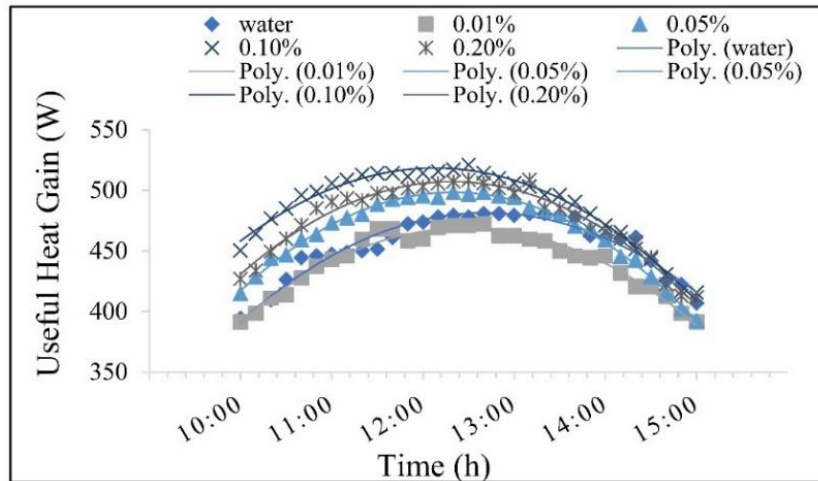


Fig. 4.15. Useful heat gain for HNF

The collector efficiency is presented in Fig. 4.16 according to the terms of inlet temperature, ambient temperature and solar radiation, which can be expressed using Eq. (3.11). Fig. 4.16 shows the efficiency of collector changes as a function of  $T^*$  using different VCs. The collector's efficiency increased with increasing volume concentration. According to the experimental results, the maximum TE of graphene- $\text{Fe}_3\text{O}_4$  HNF was obtained for 0.2%, 0.1%, 0.05% and 0.01% VCs and reached 45.46%, 44.3%, 42.04% and 41.02%, respectively, while the collector efficiency with W was 40.41%. To validate the experimental results with the simulation results, a modelling analysis and simulation using ANSYS Fluent software was used.

According to the simulation, the maximum TE of graphene- $\text{Fe}_3\text{O}_4$  HNF was obtained for 0.2%, 0.1%, 0.05% and 0.01% VCs and reached 45.44%, 44.36%, 42.32% and 42.37%, respectively, while the collector efficiency with water was 40.97%. It was observed that thermal efficiencies using NFs at all operating conditions was higher than base fluid. Fig. 4.17 shows the results of the experimental and simulation work with W and a 0.2% volume concentration of hybrid nanofluid, the efficiencies were close to each other. Fig. 4.18 shows the temperature distribution and inlet and outlet temperatures on the absorber pipe for water and HNF at  $\text{RE} = 7690$ .

The results obtained from the numerical and experimental work were in good agreement, so they could be utilised to validate the numerical analysis. Finally, mixing of nanoparticles to the working fluid is an effective method to increase the thermal energy collected and nanofluid's thermophysical properties such as enthalpy, specific heat capacity, TC, and density.



## 4. Results

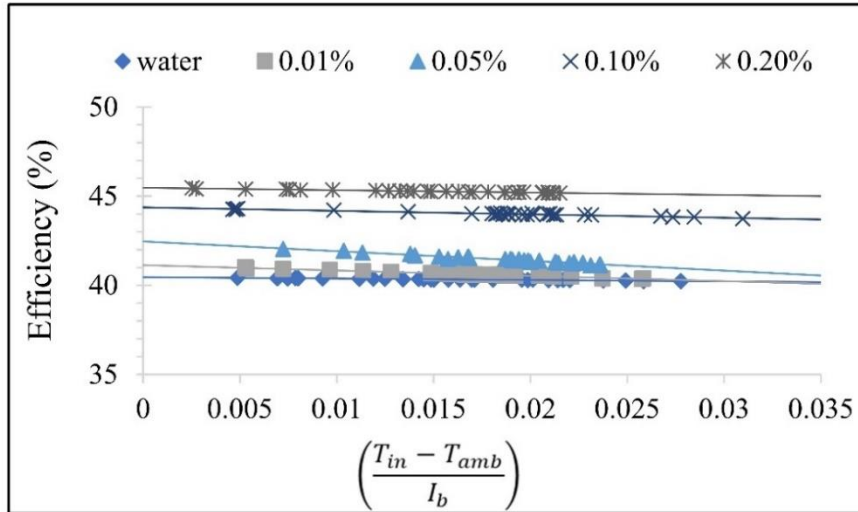


Fig. 4.16. TE versus heat loss parameter at different VCs of graphene-Fe<sub>3</sub>O<sub>4</sub> HNF

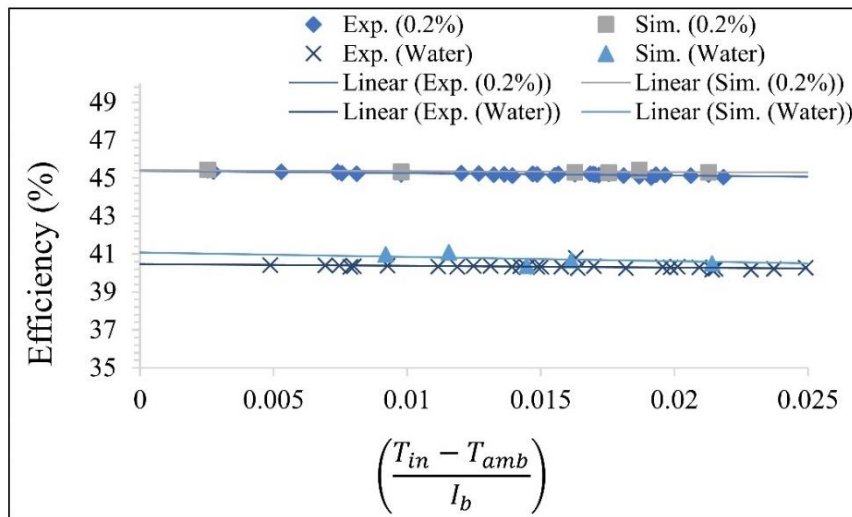
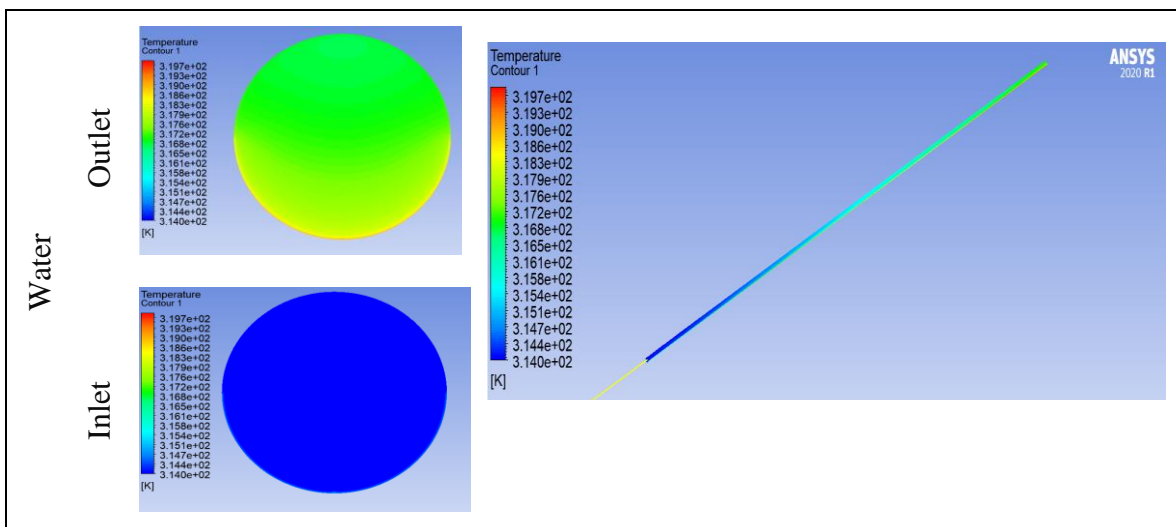
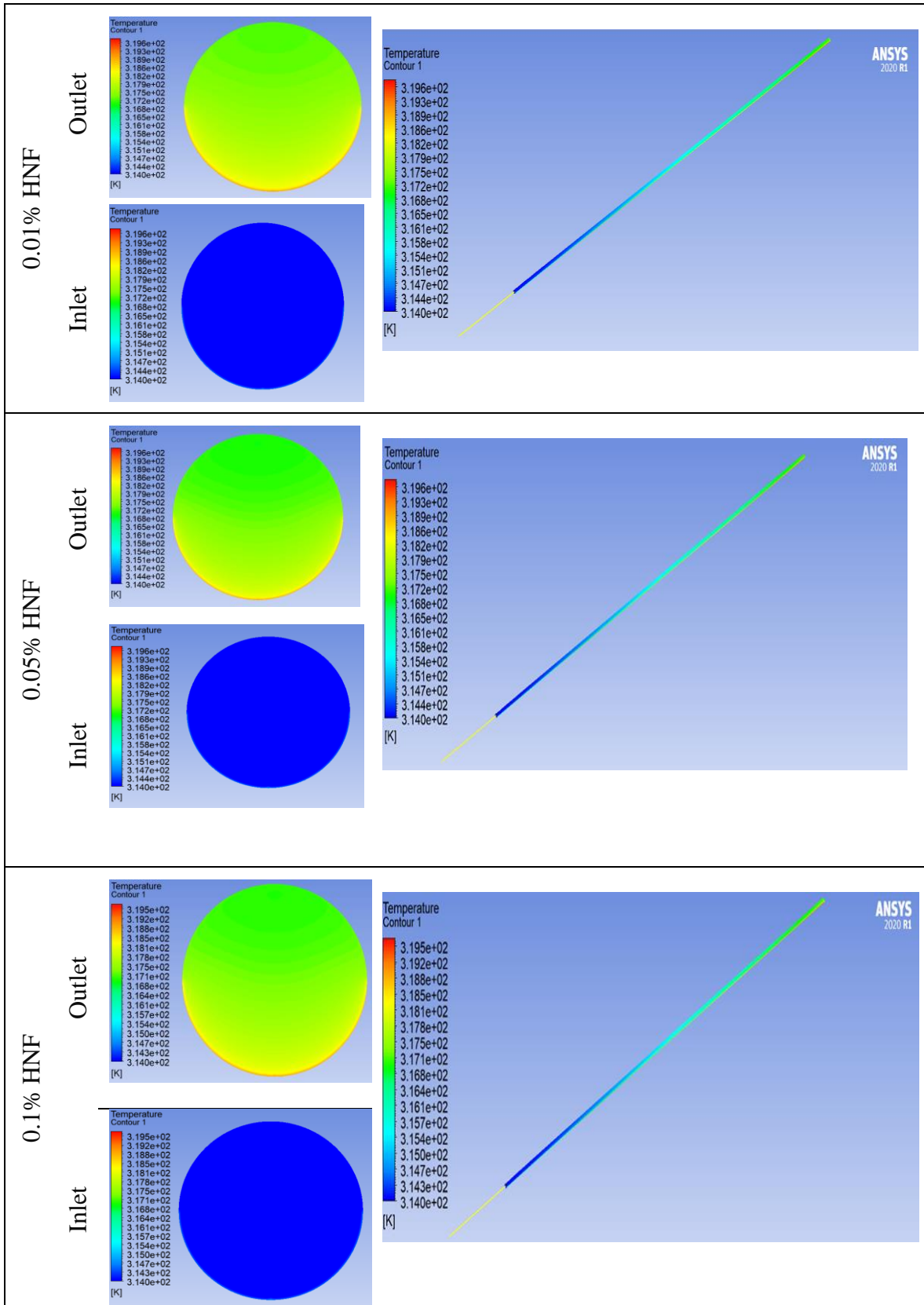


Fig. 4.17. Validation results of the numerical model with experimental data for the HNF and water



## 4. Results





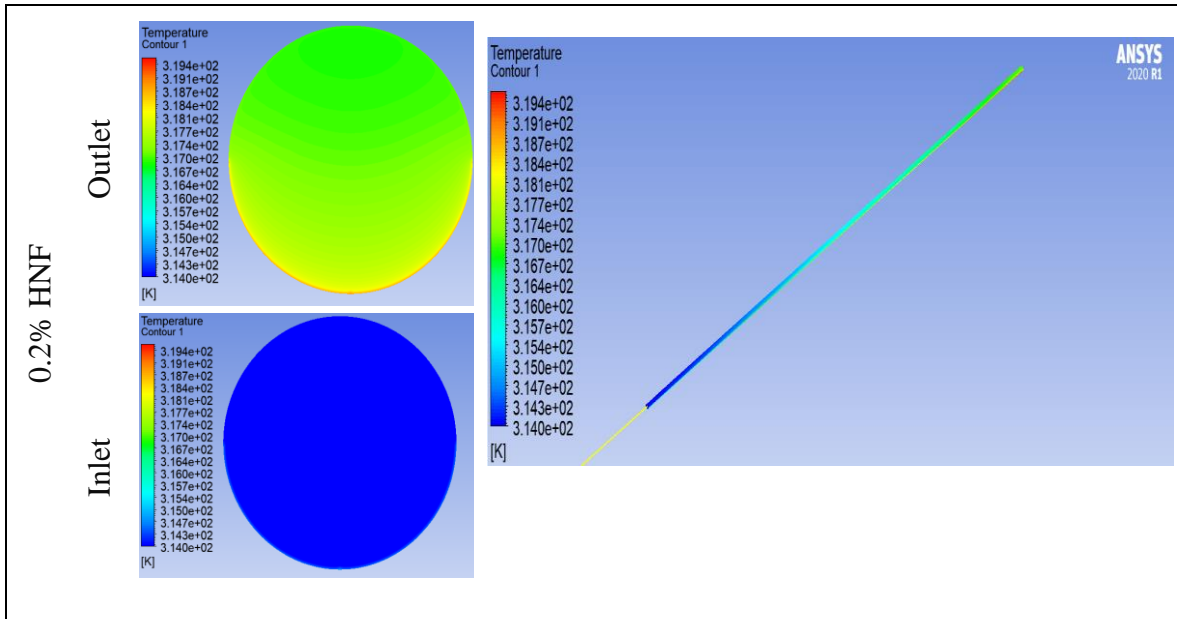
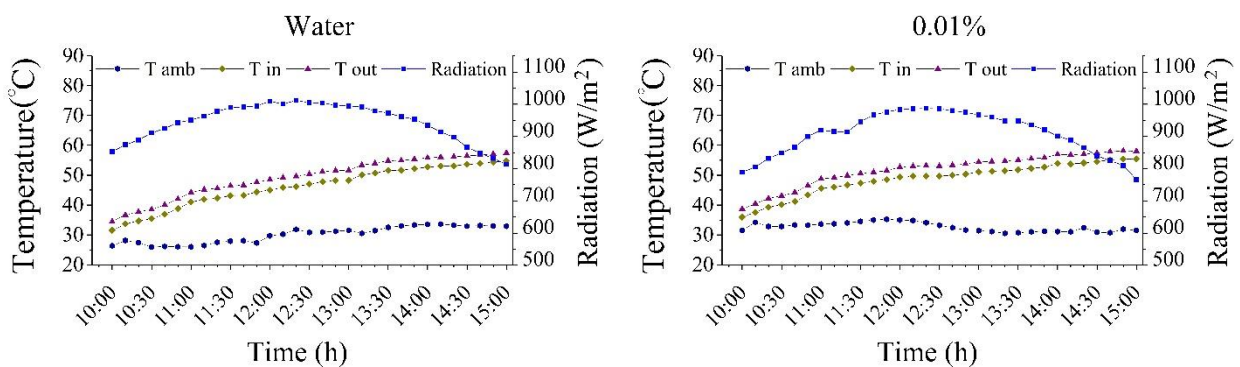


Fig. 4.18. Temperature contours of water and different HNFs

#### 4.5. Test case graphene nanofluid

This study involved using the PTSC to determine the efficiency of a working fluid made of graphene nanoparticles suspended in a water as based nanofluid. Before the experiment, a similarity test is done to make sure that the two collectors give the same results.

The experiments were carried out with G/water NFs in different concentrations (0.01%, 0.05%, 0.1%, and 0.2%) with a mass flow rate of 120 L/h. Furthermore, the TE of PTSC will be evaluated and examined at different concentrations. The test was performed at a mass flow rate of 120 L/h, and the required measurements were obtained and recorded. The experiments were carried out at the solar lab of the Hungarian University of Agriculture and Life Sciences from around 10:00 to 15:00 in the summer of 2022. Fig. 4.19 represents the experimental data that were recorded for temperatures and solar radiation.



## 4. Results

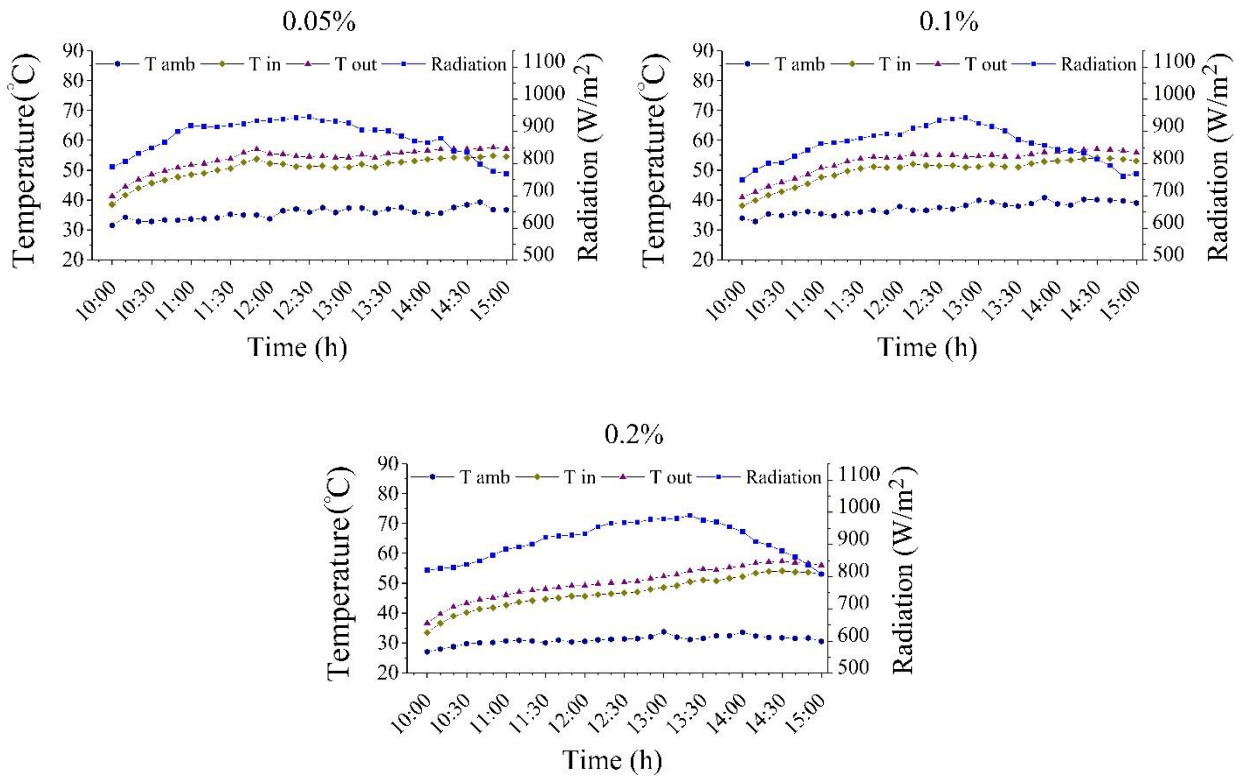


Fig. 4.19. Test results for water, 0.01% NF, 0.05% NF, 0.1% NF and 0.2% NF

Fig. 4.20 shows that the heat removal factor of NF was higher than the water. As observed, the heat removal factor increased as the concentration of nanoparticles increased. According to the results, the heat removal factor of the G–NF was 58%, 56%, 54% and 52.8% for 0.2%, 0.1%, 0.05% and 0.01% VCs, respectively, while the heat removal factor with W was 51.7%. Table 4.4 shows the TE equations, heat removal factors and heat loss coefficients for W and NF at different concentrations. At 0.2% volume concentration of graphene/water NF, the heat removal factor reached the maximum value of 58.07%. In addition, the overall heat loss coefficient ( $U_L$ ) reached 32.68 W/m<sup>2</sup>K. For base fluid (water), the heat removal factor reaches the minimum value of 51.78%. It's clear that the heat removal factors for graphene/water NF are more than water for all examined volume concentrations. The increase in heat removal factor with increasing concentrations is due to the increased TC resulting from the increase in nanoparticle concentration.

The useful heat from the PTSC can be calculated using Eq. (3.8) based on the temperature difference in the fluid that flows through the receiver tube. At the beginning of the experiment, the useful heat gain is low since the solar radiation is low, then it starts to increase as time passes until reaching the peak values at noon; after that, it was decreased. Therefore, the solar irradiation rate affects the energy collected. In addition, the useful heat gain increased with an increased volume concentration. Fig. 4.21 shows the useful energy with time in all cases.

## 4. Results

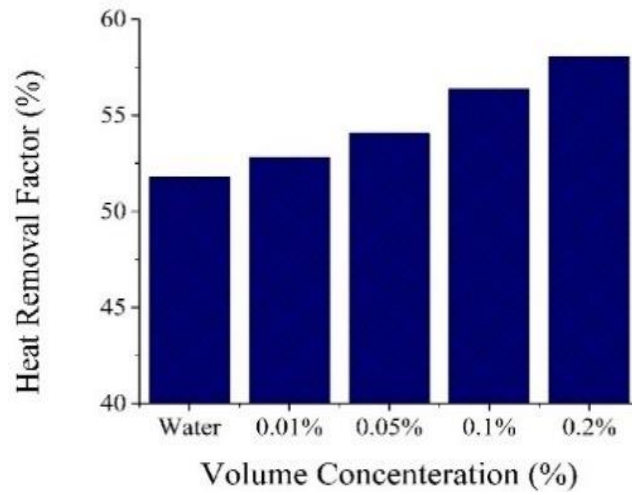


Fig. 4.20. Heat removal factors at different VCs and water

Table 4.4. represents the collector efficiency equations for W and G-NF

VCs	Equation of efficiency	R <sup>2</sup>	F <sub>r</sub>
Water	$\eta_{th} = 40.766 - 71.884 \left( \frac{T_{in} - T_{amb}}{I_b} \right)$	0.9816	51.7
0.01%	$\eta_{th} = 41.567 - 58.337 \left( \frac{T_{in} - T_{amb}}{I_b} \right)$	0.9798	52.8
0.05%	$\eta_{th} = 42.554 - 64.708 \left( \frac{T_{in} - T_{amb}}{I_b} \right)$	0.9238	54
0.1%	$\eta_{th} = 44.381 - 70.887 \left( \frac{T_{in} - T_{amb}}{I_b} \right)$	0.9643	56.3
0.2%	$\eta_{th} = 45.713 - 114.56 \left( \frac{T_{in} - T_{amb}}{I_b} \right)$	0.985	58

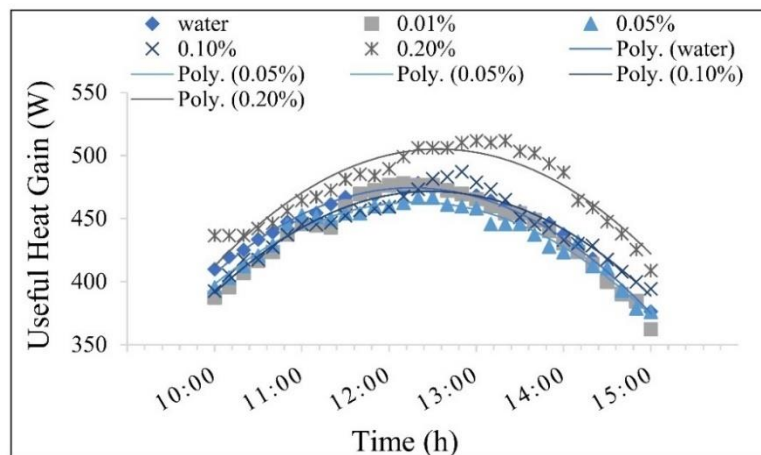


Fig. 4.21. Useful heat gain for NF

## 4. Results

The collector efficiencies were presented according to the inlet temperature, ambient temperature and solar radiation, which can be expressed using Eq. (3.11). Fig. 4.22 shows the efficiency of collector changes as a function of  $T^*$  using different VCs. The collector's efficiency has increased with increasing volume concentration. According to the experiment, the maximum TE of graphene/water NF was obtained for 0.2%, 0.1%, 0.05%, and 0.01% VCs and reached 44.73%, 43.97%, 42.06%, and 41.23%, respectively, while the collector efficiency with water was 40.36%. To validate the experimental results with the simulation results, a modelling analysis and simulation using ANSYS Fleunt software is used.

According to the simulation, the maximum TE of NF was obtained for 0.2%, 0.1%, 0.05%, and 0.01% VCs and reached 45.75%, 44.31%, 42.26%, and 42.3%, respectively, while the collector efficiency with water was 40.45%. It was observed that thermal efficiencies using NF at all operating conditions was higher than water.

Fig. 4.23 shows the results of the experimental and simulation work with water and a 0.2% VCs of NF, and the efficiencies were close to each other.

Fig. 4.24 shows the temperature distribution and inlet and outlet temperatures on the absorber pipe for water and NF at  $RE = 7690$ .

The results obtained from the numerical and experimental work were in good agreement, so they could be utilised to validate the numerical analysis. Finally, mixing of nanoparticles to the working fluid is an effective method to increase the thermal energy collected and nanofluid's thermophysical properties such as enthalpy, specific heat capacity, thermal conductivity, and density.

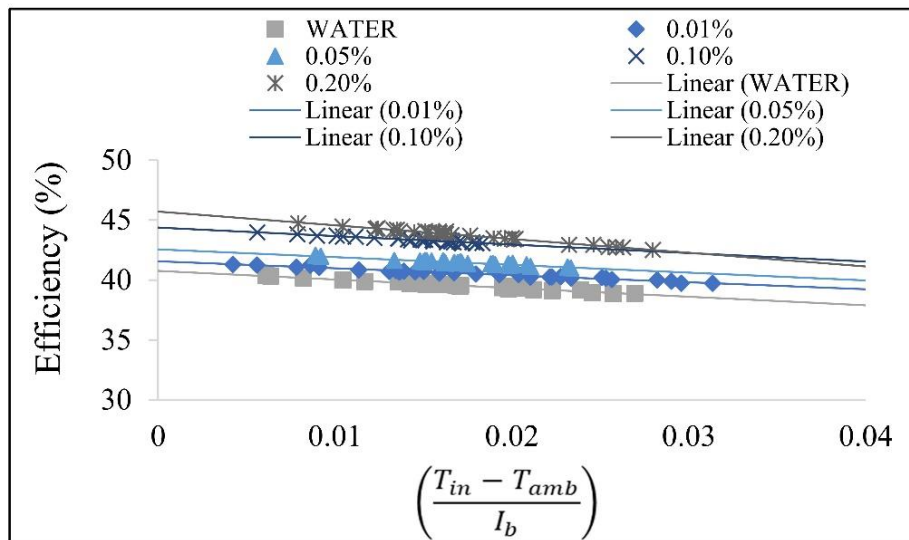


Fig. 4.22. TE versus heat loss parameter at different VCs of graphene/water NF

## 4. Results

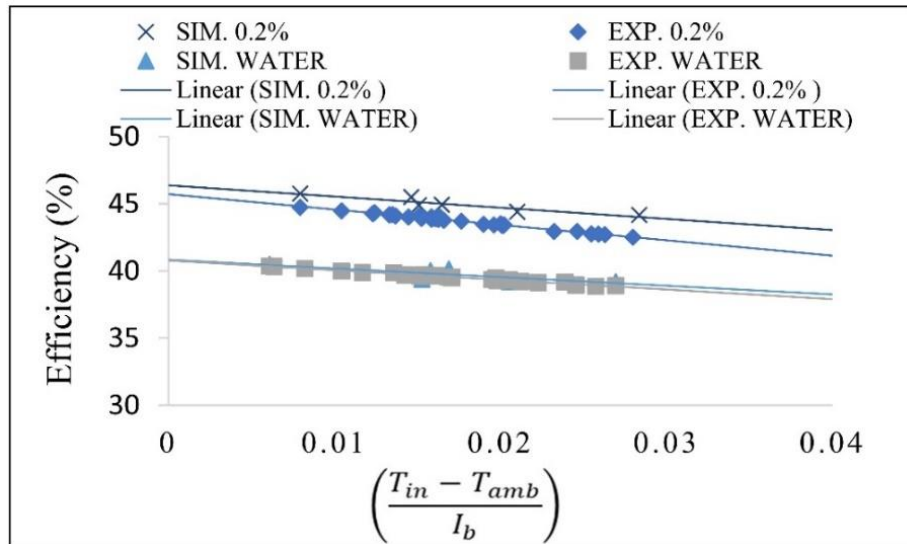
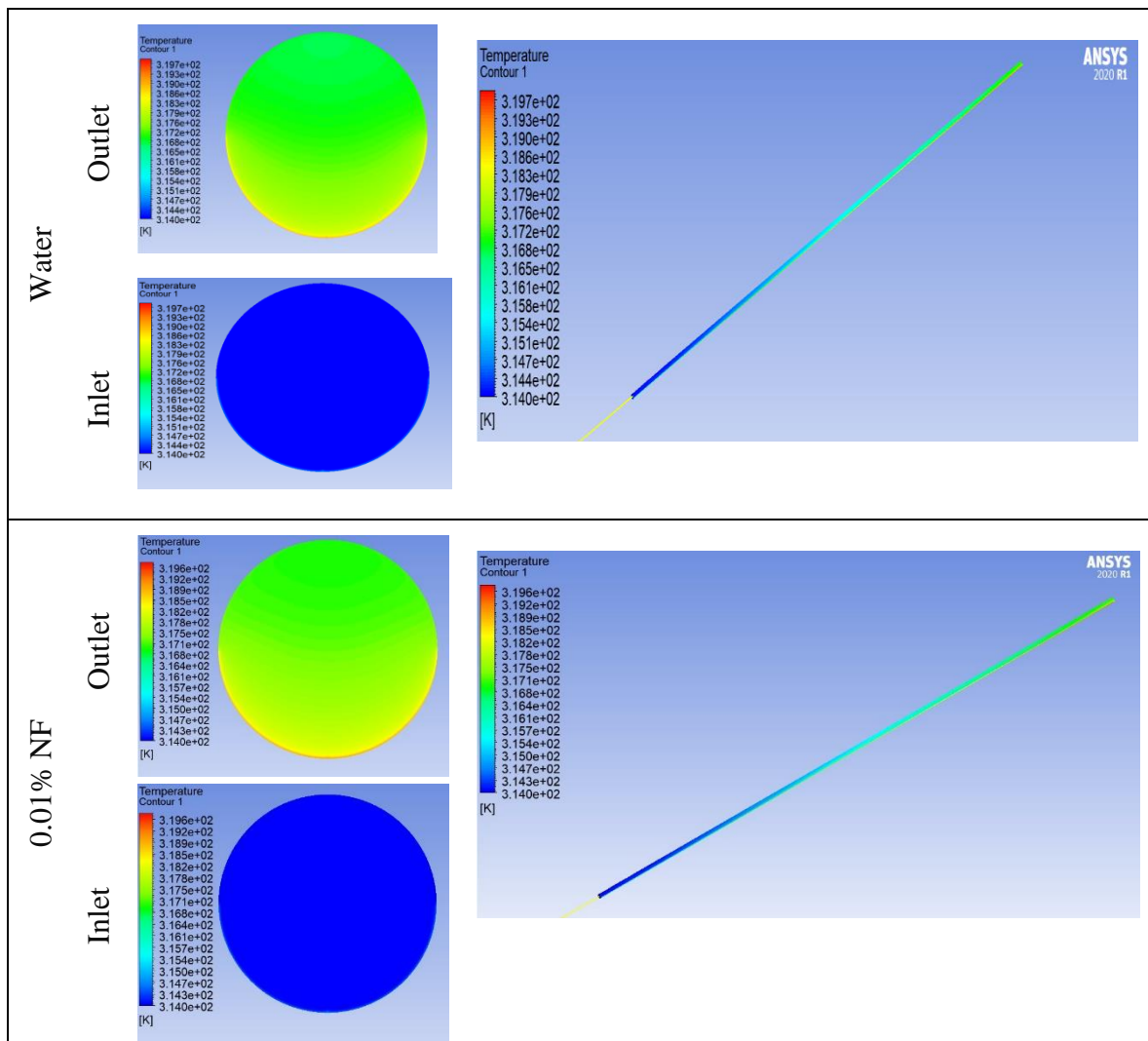


Fig. 4.23. Validation results of the numerical model with experimental data for the NF and water



## 4. Results

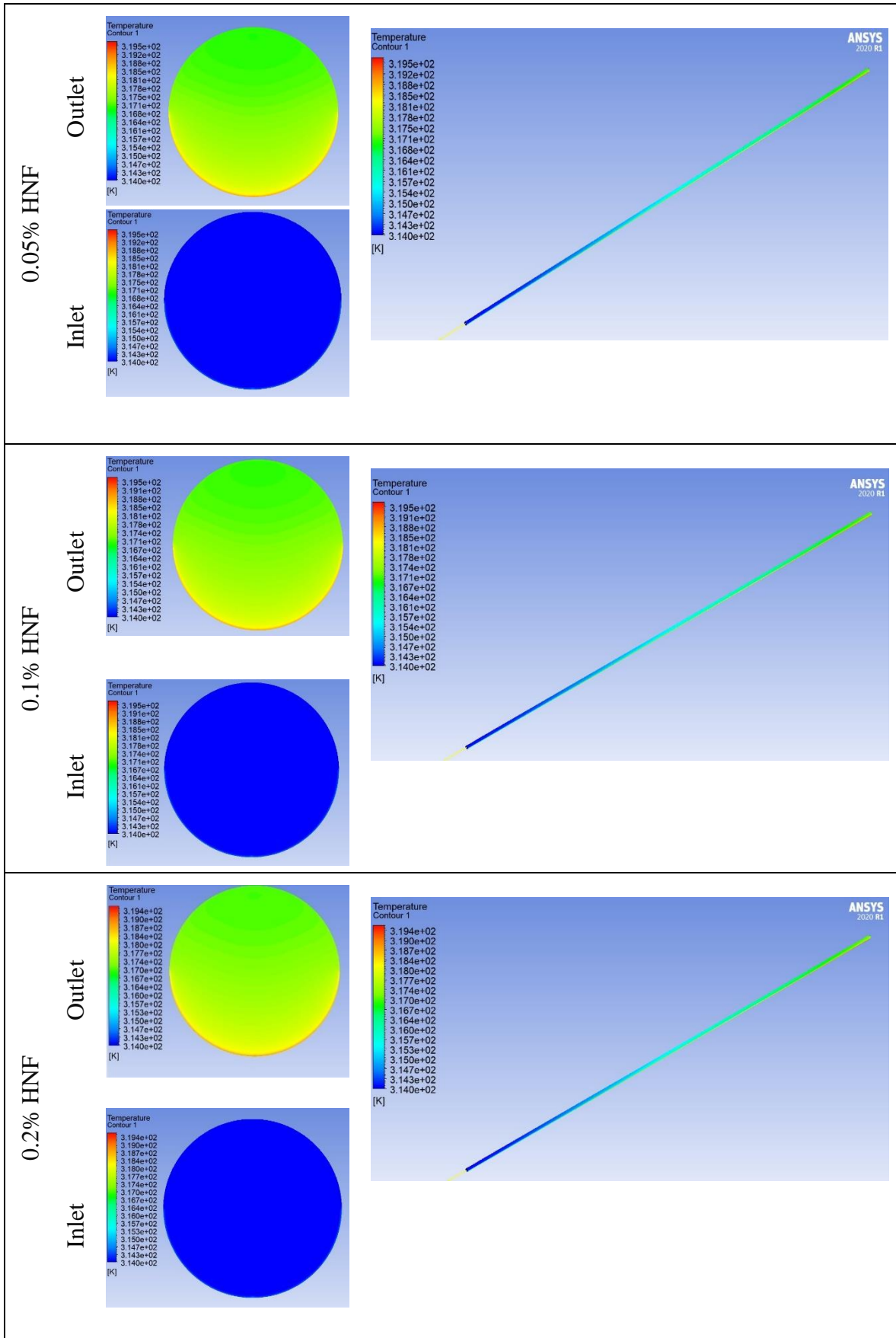


Fig. 4.24. Temperature contours of water and different graphene/water NF



#### 4.6. The receiver geometry

The receiver geometry has influence on the optical efficiency by increasing the absorbed radiation or decreasing collector heat loss. Enhancing the thermal performance of the receiver is essential for PTSC efficiency improvement. This increases the heat transfer from the receiver's inside surface to the thermal fluid, resulting in lower heat losses and improved thermal performance. The absorber tubes were manufactured as described in the Materials and Methods chapter, and an evacuated absorber tube was used in the experiment. The experiments were done at the Hungarian University of Agriculture and Life Sciences from 10:00 to 15:00 on August 22. Different receivers were designed from copper material; four different cases are investigated, as they are described in Fig. 4.25. In addition, all cases used water as the base fluid to determine which was better for applications of PTSC. Furthermore, the comparison is made with two different mass flow rates (60 and 120 L/h), and the required measurements were obtained and recorded. Figs. 4.26 and 4.27 represent the experimental data that were recorded for temperatures and solar radiation.

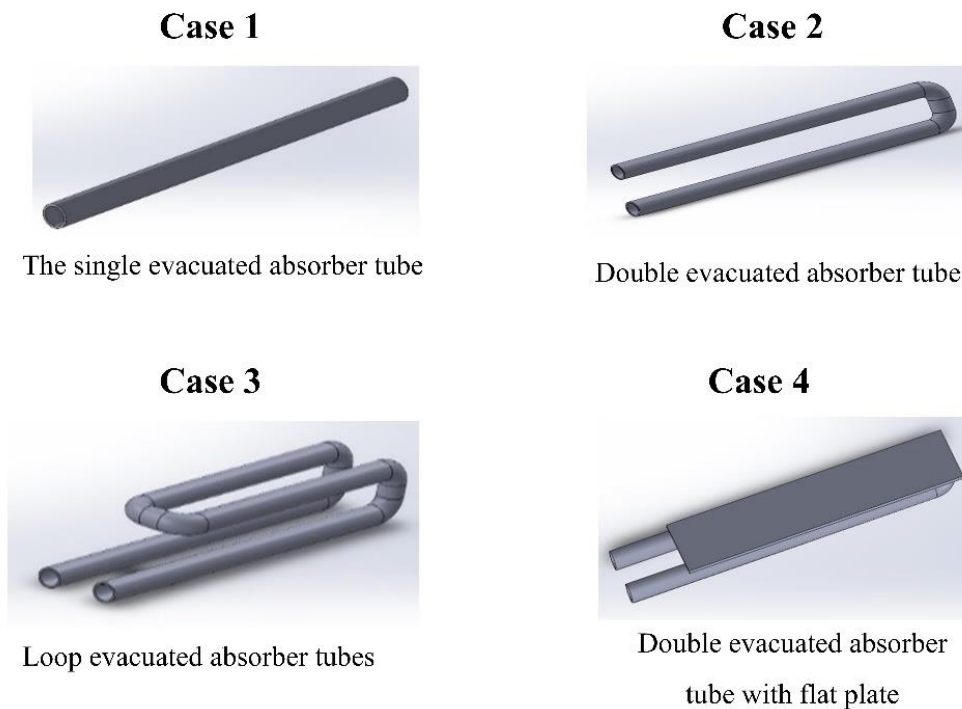


Fig. 4.25. The four examined cases in the PTSC module

## 4. Results

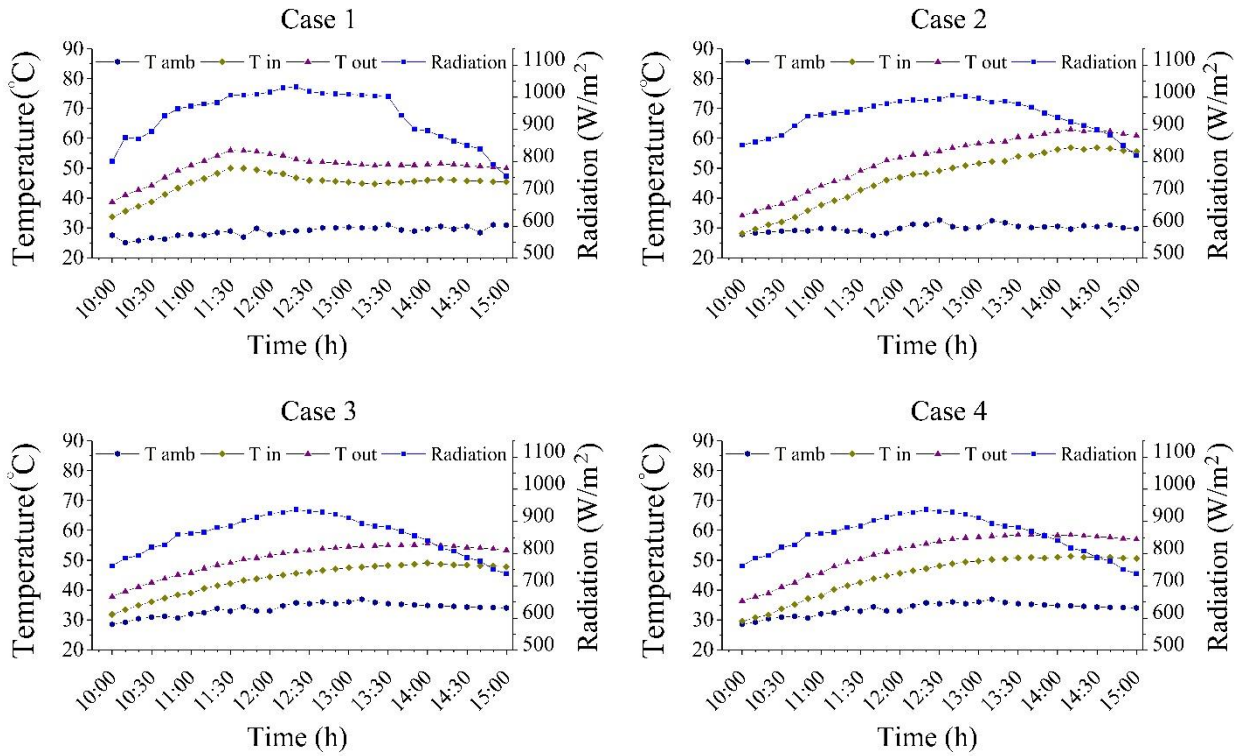


Fig. 4.26. Test results of water in different cases of 60 L/h

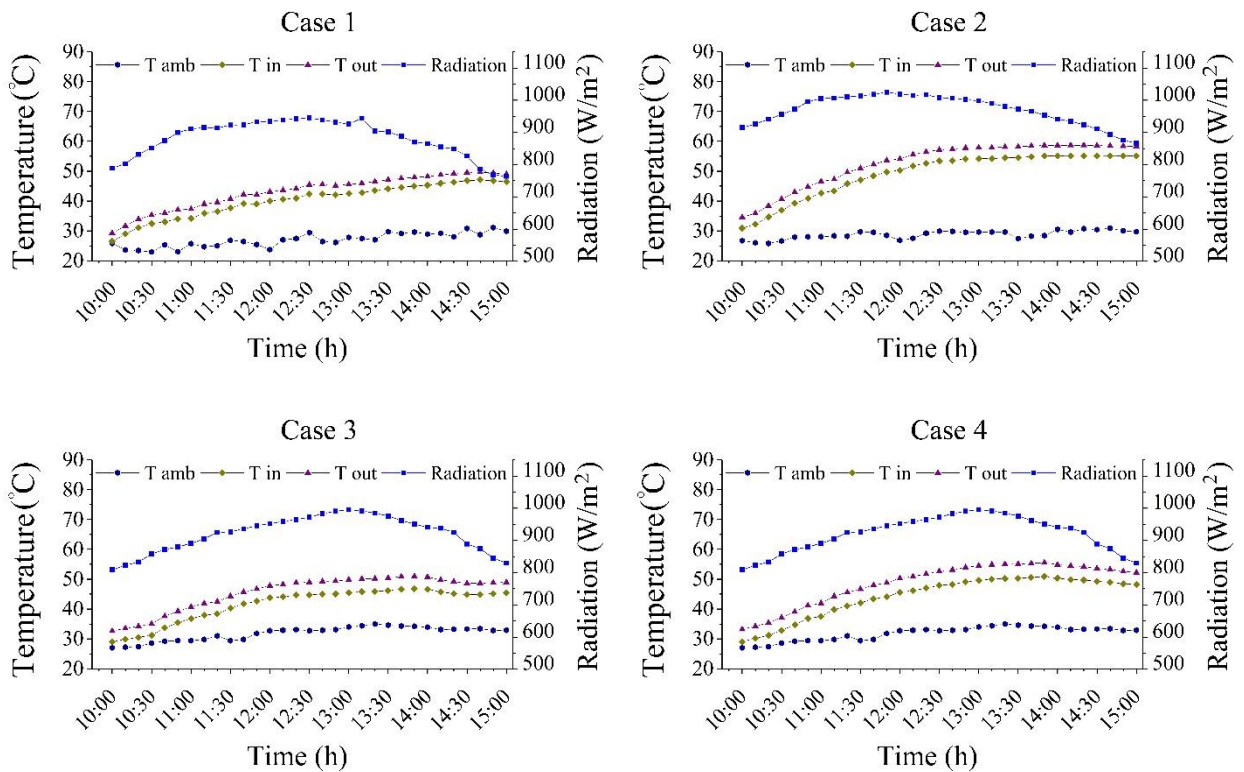


Fig. 4.27. Test results of water in different cases of 120 L/h



## 4. Results

The heat removal factor is represented by the ratio of the actual to the maximum heat transfer through the PTSC. The heat removal factor of water was changed according to the absorber design, as shown in Figs. 4.28 and 4.29. Thus, the amount of heat removal factor obtained for a 60 L/h mass flow rate is equal to 65.7%, 58.1%, 50.1%, and 48.1% for cases 4, 3, 2, and 1, respectively.

The amount of heat removal factor obtained for a 120 L/h mass flow rate is equal to 73.4%, 65.8%, 58.5%, and 50.3% for cases 4, 3, 2, and 1, respectively.

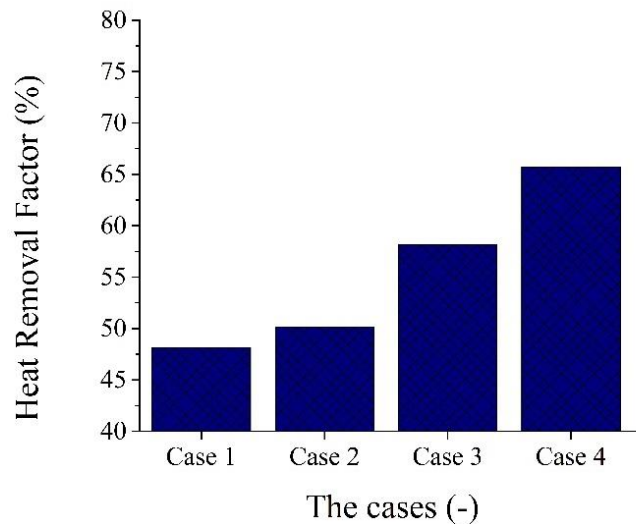


Fig. 4.28. Heat removal factors in different cases of 60 L/h

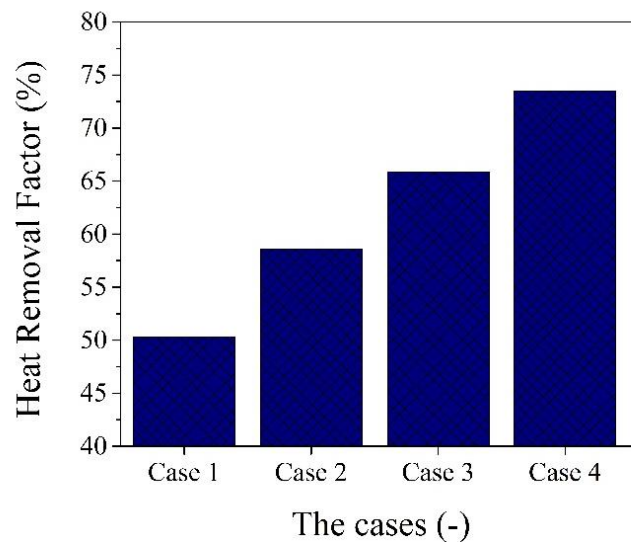


Fig. 4.29. Heat removal factors in different cases 120 L/h

## 4. Results

Tables 4.5 and 4.6 show the thermal efficiency equations and the heat removal factors for a 60 and 120 L/h mass flow rate in different situations.

Table 4.5. Model equations of PTSC efficiency for different cases in 60L/h mass flow rates

VCs	Equation of efficiency	R <sup>2</sup>	F <sub>r</sub>
Case 1	$\eta_{th} = 38.706 - 184.1 \left( \frac{T_{in} - T_{amb}}{I_b} \right)$	0.99	48.1
Case 2	$\eta_{th} = 40.301 - 65.26 \left( \frac{T_{in} - T_{amb}}{I_b} \right)$	0.99	50.1
Case 3	$\eta_{th} = 46.778 - 153.75 \left( \frac{T_{in} - T_{amb}}{I_b} \right)$	0.969	58.1
Case 4	$\eta_{th} = 52.853 - 80.447 \left( \frac{T_{in} - T_{amb}}{I_b} \right)$	0.9768	65.7

Table 4.6. Model equations of PTSC efficiency for different cases in 120 L/h mass flow rates

VCs	Equation of efficiency	R <sup>2</sup>	F <sub>r</sub>
Case 1	$\eta_{th} = 40.474 - 72.332 \left( \frac{T_{in} - T_{amb}}{I_b} \right)$	0.98	50.3
Case 2	$\eta_{th} = 47.11 - 130.97 \left( \frac{T_{in} - T_{amb}}{I_b} \right)$	0.99	58.5
Case 3	$\eta_{th} = 52.947 - 180.14 \left( \frac{T_{in} - T_{amb}}{I_b} \right)$	0.943	65.8
Case 4	$\eta_{th} = 59.086 - 101.4 \left( \frac{T_{in} - T_{amb}}{I_b} \right)$	0.9426	73.4

The useful heat from the PTSC can be calculated using Eq. (3.8) based on the temperature difference in the fluid flows through the receiver tube. At the beginning of the experiment, the useful heat gain is low as the solar radiation is low, then it started to increase with the time until reaching the peak values at noon; after that, it was decreased. Therefore, the solar irradiation rate affects the energy collected. Figs. 4.30 and 4.31 show the useful energy with time in all cases of 60 and 120 L/h mass flow rate.

## 4. Results

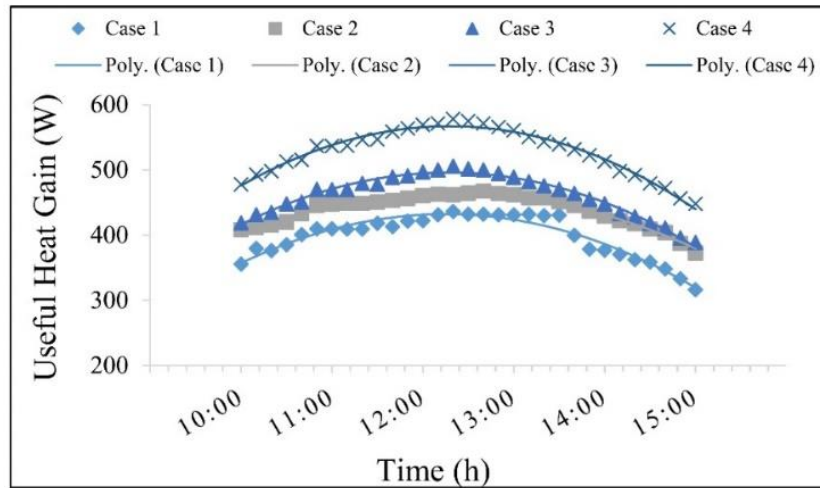


Fig. 4.30. Useful heat gain in different cases of 60 L/h

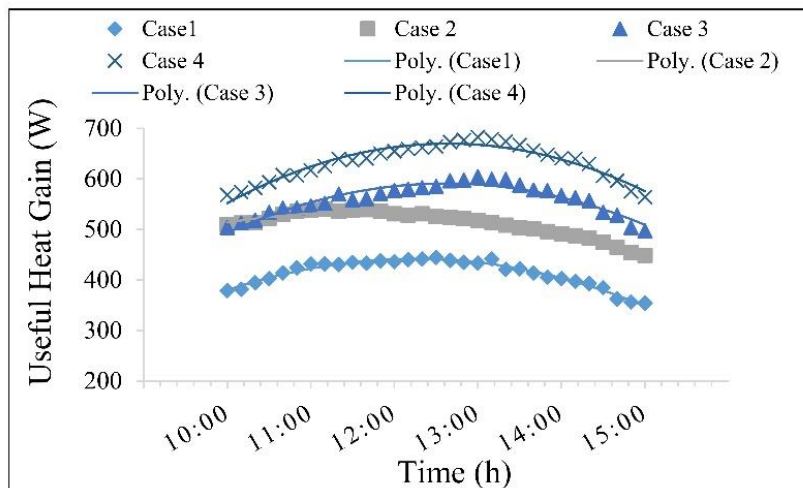


Fig. 4.31. Useful heat gain in different cases 120 L/h

The collector's efficiency for each case is presented as a function of  $T^*$ . Figs. 4.32 and 4.33 compare thermal efficiencies in four cases at a 60 and 120 L/h mass flow rate. Obviously, TE values obtained differ according to the design of the absorber tube.

According to the experiment results, the maximum TE for a 60 L/h mass flow rate is equal to 52.7%, 46.17%, 40.26%, and 37.27% for cases 4, 3, 2, and 1, respectively. According to the experiment results, the maximum TE for a 120 L/h mass flow rate was equal to 59.05%, 52.39%, 46.84%, and 40.37% for cases 4, 3, 2, and 1, respectively.

According to the results, the thermal performance of the PTSC using a double-evacuated absorber tube with a flat plate is better than in other cases. The receiver tube showed a remarkable enhancement of TE by decreasing thermal losses. Finally, the absorber tube is a more effective part for improving system performance.

## 4. Results

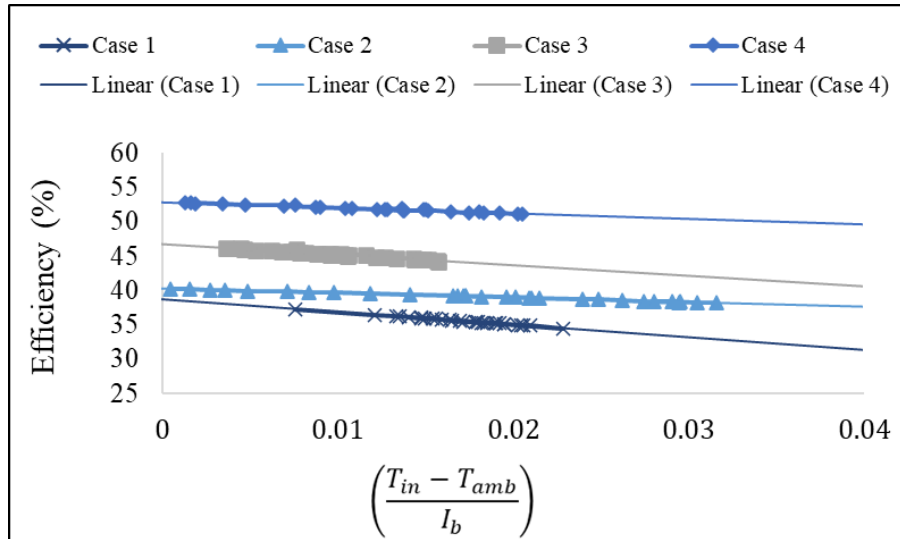


Fig. 4.32. TE versus heat loss parameter at different cases of 60 L/h

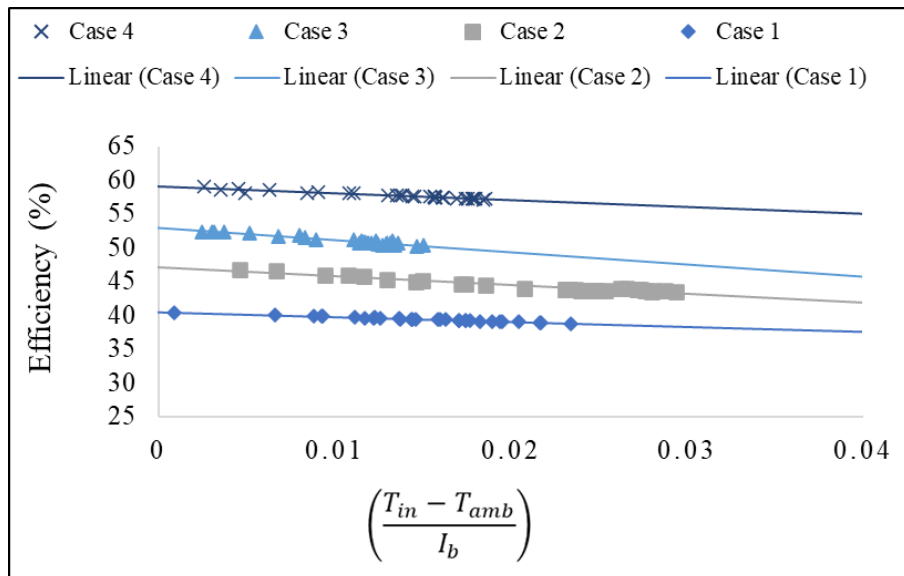


Fig. 4.33. TE versus heat loss parameter in different cases 120 L/h

#### 4.7. New scientific results

The experimental and numerical heat transfer performance of a parabolic trough collector was investigated in this research. This section presents the new scientific findings from this research work as follows:

##### 1. Thermal conductivity of mono and hybrid nanofluid

Based on experimental results, I have identified a new proposed correlation for graphene/water and graphene-Fe<sub>3</sub>O<sub>4</sub>/water nanofluids (with GA surfactant) thermal conductivity enhancement ratios. This correlation is valid for volume concentrations ranging from 0.01% to 0.2% and temperatures ranging from 20 °C to 60 °C.

For graphene/water:

$$TCR = 0.9965 + 0.7082 \varphi + 0.000518 T - 1.835 \varphi^2 + 0.006788 \varphi T, R^2=0.9881.$$

For graphene-Fe<sub>3</sub>O<sub>4</sub>/water:

$$TCR = 0.9994 + 0.05436\varphi + 0.00012T - 0.4568\varphi^2 + 0.01178\varphi T, R^2=0.9791.$$

According to experimental results, the thermal conductivity of 0.2% graphene-Fe<sub>3</sub>O<sub>4</sub>/water was evaluated at 60 °C and observed it was 14.4% higher than the thermal conductivity of the base fluid. And graphene/water nanofluid, I have observed that the thermal conductivity of 0.2% graphene/water at 60 °C was 17% higher than the thermal conductivity of the base fluid.

##### 2. Viscosity of mono and hybrid nanofluid

Based on experimental results, I have identified a new proposed correlation for measuring the relative viscosity of graphene/water and graphene-Fe<sub>3</sub>O<sub>4</sub>/water nanofluids with GA surfactant. This correlation is valid for volume concentrations ranging from 0.01% to 0.2% and temperatures ranging from 20 °C to 60 °C.

For graphene /water:

$$RV = 1.059 + 3.647\varphi - 0.0005436T - 5.19\varphi^2 - 0.003709\varphi T, R^2=0.9744.$$

For graphene-Fe<sub>3</sub>O<sub>4</sub>/water:

$$RV = 1.044 + 1.889\varphi - 0.0006066T - 0.6786\varphi^2 - 0.001685\varphi T, R^2=0.99.$$

##### 3. Effect of mono and hybrid nanofluid with surfactant on the PTSC efficiency

I have developed and evaluated a new test rig of two identical PTSC collectors: one uses water as a working fluid, and the other uses graphene/water and graphene-Fe<sub>3</sub>O<sub>4</sub>/water nanofluids with Gum Arabic surfactant with different concentrations (0.01%, 0.05%, 0.1%, and 0.2%) and a mass flow rate of 120 L/h.

Based on experimental results, I identified that all cases investigated under the same conditions showed that the performance of mono- and hybrid-nanofluids is preferable to use in parabolic collector systems than the water, increasing efficiency and the output temperature of the PTSC.

Based on experimental results, the maximum thermal efficiency of PTSC for graphene-Fe<sub>3</sub>O<sub>4</sub>/water hybrid nanofluid was obtained for 0.2% volume concentration, reaching 45.46%, and the maximum thermal efficiency of PTSC for graphene/water nanofluid was obtained for 0.2% volume concentration, reaching 44.73%.

#### *4. Numerical analysis of PTSC performance*

I have developed an appropriate ANSYS Fluent Simulation Model like the experiment model in dimensions in order to investigate the convection heat transfer coefficient and hydrodynamic behaviours of mono and hybrid nanofluids by calculating the output temperature and efficiency of PTSC. The heat transfer coefficient results showed a notable increase by increasing the concentrations.

The ANSYS Fluent numerical analysis was validated using theoretical results that accounted for Nusselt and friction factor correlations. It has been found that the results of the experimental and simulation work with water and a 0.2% volume concentration of both the graphene-Fe<sub>3</sub>O<sub>4</sub>/water and graphene/water nanofluids had efficiencies that were close to each other.

#### *5. Effect of the receiver geometry on the PTSC performance*

I have developed two novel geometry of the receiver tubes (loop evacuated absorber tube, and a double evacuated absorber tube with a flat plate) and compared them with the traditional tubes used in solar collectors. The results showed that the optical efficiency was enhanced by increasing the absorbed radiation or decreasing collector heat loss. In addition, all cases used water as the base fluid.

Based on the experimental findings, I have observed that the maximum heat removal factor obtained for 120 L/h mass flow rate was about 73.4% for the case of a double evacuated absorber tube with a flat plate, and the maximum thermal efficiency of the PTSC with double-evacuated absorber tube with flat plate at 120 L/h was 59.05%. Conclusively, the PTSC's thermal performance using loop-evacuated and double-evacuated absorbers with flat plates was more effective than that of traditional tubes, regardless of mass flow rate.

#### *6. Effect of the absorber coating*

I have developed and prepared a novel nanocoating by adding iron oxide and graphene nanoparticles to the matte acrylic coating at a 0.2% volume concentration. Based on experimental results, the PTSC thermal performance using nanocoating film is preferable to use in parabolic collector systems than the matte acrylic coating, regardless of mass flow rate.

Based on experimental results, I have observed that the heat removal factor of water increased as the mass flow rate increased and the maximum heat removal factor of PTSC for nanocoating at 120 L/h was 52.7%, and the maximum thermal efficiency of PTSC for nanocoating at 120L/h was 41.58%.

### *7. Effect of the reflective surface on the PTSC performance*

I have proposed a novel reflective surface for two identical PTSC collectors: one based on silver chrome film and the other on aluminium sheet. According to the experimental results, I have observed that the maximum heat removal factor and maximum thermal efficiency of PTSC for silver chrome film were, respectively, 58.5% and 46.84% at 120 L/h.

Based on experimental results, I found out that the PTSC thermal performance of silver chrome film is preferable to that of aluminium sheet in parabolic collector systems, regardless of working fluid mass flow rates.

## 5. CONCLUSIONS AND SUGGESTIONS

An experimental evaluation has been conducted to determine the performance of a novel parabolic trough solar collector using different reflecting surfaces, coating, tube designs, mono nanofluid, and hybrid nanofluid. Two identical PTSC systems were designed, manufactured, installed, and tested under the climatic conditions of at the Hungarian University of Agriculture and Life Sciences in Hungary.

In the beginning, similarity tests of the two collectors were carried out using aluminium reflective surfaces for each one with a mass flow rate of 90 L/h. It was found that the average thermal efficiency between collectors did not exceed 0.3%. During the experimental periods, the data was collected for solar radiation and temperatures (ambient, inlet, and outlet temperatures) for use them in the boundary conditions in the ANSYS software. Further, the temperature difference decreased as the flow rate through the absorber tube increased.

The reflective surface material of the PTSC greatly influenced its performance and efficiency. The silver chrome film has superior optical properties compared to regular aluminium reflective surfaces. The maximum thermal efficiency of PTSC for silver chrome film at 120 L/h was 46.84%.

Adding iron oxide and graphene nanoparticles to the matte acrylic coating has increased the amount of radiation absorption. Thus improved the optical and thermal efficiency of PTSC.

Four different receivers were designed from copper material, and four different cases were investigated. According to the results, the maximum thermal efficiency of PTSC for cases 4, 3, 2, and 1 at 120 L/h was 59.05%, 52.39%, 46.84%, and 40.37%, respectively. Furthermore, the receiver tube has increased the optical efficiency by increasing the absorbed radiation and decreasing collector heat loss.

Nanofluids significantly improved the thermophysical properties of working fluids. The NFs improved the heat transfer performance of the absorber. In addition, increasing the volume concentration of hosted nanoparticles has enhanced the collector's thermal performance and increasing the concentration and temperature of nanofluids had improved their thermal conductivity. In all cases investigated under the same conditions, the performance of nanofluids were found to be higher than that of water, increasing the efficiency and the output temperature of the PTSC.

There are numerous recommendations for future works that can be made. Further studies can be conducted with variations in physical geometries to improve the collector and passive convective heat transfer for the absorber tube in PTSC. Studies on different shapes of absorber tubes (e.g., elliptical cross section) and their effects on thermal efficiency and distribution of heat flux are recommended. Many areas still need to be investigated using HNFs and mono-nanofluids. To support their efficient application in PTSCs, the economic effects of the price and expense of nanoparticles of nanofluid preparation synchronizing with thermal performance enhancement may be investigated. In addition, different coatings need to be mixed with other materials for better properties. Furthermore, comparing the performance of the PTSC system using different diameters of absorber tubes could be conducted.



## 6. SUMMARY

### PERFORMANCE ANALYSIS OF A PARABOLIC TROUGH SOLAR COLLECTOR

A comprehensive performance analysis of a novel parabolic trough solar collector (PTSC) for thermal applications has been conducted. Two identical PTSC systems were manufactured, installed, and tested at the Hungarian University of Agriculture and Life Sciences in Hungary. The PTSCs were tested in the local climate of Gödöllő, Hungary in summer months. The PTSC consists of a reflecting surface, an absorber tube, and the working fluid passing through the tube. Therefore, the material of the absorber tube affects the heat transfer between the metal and the working fluid, which impacts the performance of PTSC. In addition, an evacuated glass tube is used to reduce heat losses and enhance the performance of PTSC by improving the greenhouse effect between the glass and tube. Furthermore, the performance of PTSCs can be improved either by modifying their thermal properties or optical design.

To achieve the aim of the research, the focus was on the reflecting surface, absorber tube coating, tube design, and working fluid because they are regarded as the most important factors influencing PTSC performance. Experiments were carried out at the solar lab of the Hungarian University of Agriculture and Life Sciences from around 10:00 to 15:00.

According to the findings, surface reflectance is critical to the thermal efficiency of PTSC. The maximum thermal efficiency of PTSC with AS was obtained for a 120 l/h mass flow rate, reaching 27%. The maximum thermal efficiency of PTSC with SCF was obtained at a mass flow rate of 120 L/h, which was 46.84%. The addition of graphene-Fe<sub>3</sub>O<sub>4</sub> nanoparticles to matte acrylic coatings resulted in a significant increase in the thermal efficiency of PTSC. The maximum thermal efficiency with NC was obtained for a 120 L/h mass flow rate and reached 41.58%. According to the results, the thermal performance of the PTSC using nanocoating is better than matte acrylic coating. Moreover, the thermal modifications in the absorber tube are able to enhance efficiency and increase the useful output. The maximum thermal efficiency for a 120 L/h mass flow rate is equal to 59.05%, 52.39%, 46.84%, and 40.37% for the four examined cases of Double evacuated absorber tube with flat plate; Loop evacuated absorber tube; Double evacuated absorber tube and Single evacuated absorber tube, respectively. Accordingly, the absorber tube is a more effective part for improving system performance.

The addition of nanoparticles to the working fluid is an effective method to increase the thermal energy collected and the nanofluid's thermophysical properties such as viscosity, specific heat capacity, thermal conductivity, and density. HNFs bear excellent physical characteristics as compared to mono nanofluids. The maximum TE of graphene-Fe<sub>3</sub>O<sub>4</sub> HNF was obtained for 0.2% VCs and reached 45.46%. The maximum TE of graphene-NF was obtained for 0.2% VCs and reached 44.73%, while the collector efficiency with water was 40.41%. A numerical model is presented to predict the thermal behaviour of a PTSC with water and nanofluid. ANSYS Fluent numerical analysis was validated using theoretical results that accounted for Nusselt and friction factor correlations. Finally, the results obtained from the numerical and experimental work were in good agreement, so they could be used to validate the numerical analysis.

## 7. ÖSSZEFOGLALÁS (SUMMARY IN HUNGARIAN)

### PARABOLAVÁLYÚS NAPKOLLEKTOR TELJESÍTMÉNYÉNEK VIZSGÁLATA

Hőenergia célú alkalmazások során egy átfogó elemzés készült egy újszerű parabolavályús napkollektor (PTSC) teljesítményviszonyiról. Két azonos PTSC rendszer került legyártásra, telepítésre és tesztelésre a Magyar Agrár- és Élettudományi Egyetem (MATE) Gödöllői kampuszán. A PTSC-k vizsgálatára magyarországi (Gödöllő) éghajlati viszonyok között került sor a nyári hónapokban. A PTSC egy tükröző felületből, egy elnyelő csőből és a csövön áthaladó munkaközegből áll. Az elnyelő cső anyaga befolyásolja a hőátadást a fém és a munkaközeg között, amely hatással van a PTSC teljesítményére. Emellett, az üvegházhatás kihasználásával egy kétrétegű, belül vákuumos üvegcső szolgált a hőveszteségek csökkentésére és a PTSC teljesítményének növelésére. Ugyanakkor a PTSC-k teljesítményét a hőtechnikai tulajdonságaik vagy az optikai tervezésük módosításával is növelni lehet.

A kutatás céljának elérése érdekében a vizsgálatok a tükröző felületre, az elnyelő cső bevonatára, a cső tervezésére és a munkaközegre összpontosultak, mivel ezek a legfontosabb tényezőknek, amelyek befolyásolják a PTSC teljesítményét. Az kísérletek a MATE napenergia laboratóriumában történtek, naponta 10 és 15 óra között.

A vizsgálatok szerint a felület fényvisszaverő képessége kulcsfontosságú a PTSC termikus hatásfokát illetően. A legnagyobb hatásfok az alumínium tükröző felület esetén a 120 l/h tömegáram mellett érhető el, aminek értéke 27% volt. A legnagyobb hatásfok a jobb optikai paraméterekkel rendelkező ezüst-krom felületi réteg alkalmazása esetén 120 L/h tömegáramnál érhető el, aminek értéke 46,84% volt. A grafén-Fe<sub>3</sub>O<sub>4</sub> nanorészecskék hozzáadása a matt akril bevonatokhoz jelentős növekedést eredményezett a PTSC hatásfokában. A legnagyobb hatásfok nanoréteg alkalmazása esetén a 120 L/h tömegáramnál érhető el, ennek értéke 41,58% volt. Az eredmények szerint a nanoréteg bevonatú PTSC hőteljesítménye jobb, mint a matt akril bevonatúé. Emellett, a termikus jellemzők módosítása az elnyelő csőben képes növelni a hatásfokot és a hasznos teljesítményt. A legnagyobb hatásfok a 120 L/h tömegáramnál 59,05%, 52,39%, 46,84% és 40,37% volt a négy vizsgált esetben: Lemezes dupla vákuumcső; Hurkos vákuumcső; Dupla vákuumcső és egy Egyszerű vákuumcső. A kapott eredmények igazolták, hogy az elnyelő cső nagyon fontos részegység a rendszer teljesítményének javításában.

A nanorészecskéknek a munkaközeghez való hozzáadása szintén hatékony módszer a hőenergia és az energiatermelés növelésére, a nanofluid kedvezőbb termofizikai tulajdonságai (mint pl. a viszkozitás, a fajhő, a hővezető képesség és a sűrűség) miatt. A hibrid nanofluidok kiváló fizikai jellemzőkkel rendelkeznek a mono nanofluidokhoz képest. A grafén-Fe<sub>3</sub>O<sub>4</sub> hibrid nanofluid legnagyobb hatásfoka 0,2% térfogat koncentráció esetén eléri a 45,46%-ot. Grafén nanofluid esetén, 0,2% térfogati koncentrációnál, a legnagyobb hatásfok eléri a 44,73%-ot, míg a hatásfok víz szállító közeg esetén a 40,41%-t. Egy numerikus modell is kidolgozásra került a PTSC hatásfokának meghatározására tiszta víz és nanofluid hőszállító közeg esetén. Az ANSYS Fluent numerikus számításokat a Nusselt és a frakció tényező korrelációkat figyelembe vevő elméleti eredmények igazolták. A numerikus és a kísérleti eredmények jó egyezést mutattak, így alkalmazhatók a kidolgozott modell validálására.

## 8. APPENDICES

### A1: Bibliography

1. Abdelhady, S., Borello, D., and Tortora, E., (2014): Design of a small scale stand-alone solar thermal co-generation plant for an isolated region in Egypt, *Energy Conversion and Management*, 88, pp. 872–882. <https://doi.org/10.1016/j.enconman.2014.08.066>
2. Abdulhamed, A.J., Adam, N.M., Ab-Kadir, M.Z.A., and Hairuddin, A.A., (2018): Review of solar parabolic-trough collector geometrical and thermal analyses, performance, and applications, *Renewable and Sustainable Energy Reviews*, 91, pp. 822–831. <https://doi.org/10.1016/j.rser.2018.04.085>
3. Actin, A., (2013): *Cholinesterases—Advances in Research and Application: 2013 Edition*. ScholarlyEditions. Available at: [https://books.google.com/books?id=Z\\_ProivwaxgC&pgis=1](https://books.google.com/books?id=Z_ProivwaxgC&pgis=1)
4. Agagna, B., Smaili, A., and Falcoz, Q., (2017): Coupled simulation method by using MCRT and FVM techniques for performance analysis of a parabolic trough solar collector, *Energy Procedia*, 141, pp. 34–38. <https://doi.org/10.1016/j.egypro.2017.11.007>
5. Agagna, B., Smaili, A., Falcoz, Q., and Behar, O., (2018): Experimental and numerical study of parabolic trough solar collector of MicroSol-R tests platform, *Experimental Thermal and Fluid Science*, 98, pp. 251–266. <https://doi.org/10.1016/j.expthermflusci.2018.06.001>
6. Ajay, K., and Kundan, L., (2016): Combined experimental and CFD investigation of the parabolic shaped solar collector utilizing nanofluid (CuO-H<sub>2</sub>O and SiO<sub>2</sub>-H<sub>2</sub>O) as a working fluid, *Journal of Engineering (United Kingdom)*, 2016. <https://doi.org/10.1155/2016/5729576>
7. Akbarzadeh, S., and Valipour, M.S., (2018): Heat transfer enhancement in parabolic trough collectors: A comprehensive review, *Renewable and Sustainable Energy Reviews*, 92, pp. 198–218. <https://doi.org/10.1016/j.rser.2018.04.093>
8. Akbulut, M., Alig, A.R.G., Min, Y., Belman, N., Reynolds, M., Golan, Y., and Israelachvili, J., (2007): Forces between surfaces across nanoparticle solutions: Role of size, shape, and concentration, *Langmuir*, 23(7), pp. 3961–3969. <https://doi.org/10.1021/la062613g>
9. Al-Ansary, H., and Zeitoun, O., (2011): Numerical study of conduction and convection heat losses from a half-insulated air-filled annulus of the receiver of a parabolic trough collector, *Solar Energy*, 85(11), pp. 3036–3045. <https://doi.org/10.1016/j.solener.2011.09.002>
10. Al-Oran, O., A'saf, A., and Lezsovits, F., (2022): Experimental and modelling investigation on the effect of inserting ceria-based distilled water nanofluid on the thermal performance of parabolic trough collectors at the weather conditions of Amman: A case study, *Energy Reports*, 8, pp. 4155–4169. <https://doi.org/10.1016/j.egypr.2022.03.030>
11. Al-Oran, Otabeh, and Lezsovits, F., (2020): Enhance thermal efficiency of parabolic trough collector using tungsten oxide/syltherm 800 nanofluid, *Pollack Periodica*, 15(2), pp. 187–198. <https://doi.org/10.1556/606.2020.15.2.17>
12. Al-Oran, O., and Lezsovits, F., (2020): Recent experimental enhancement techniques applied in the receiver part of the parabolic trough collector – A review, *International Review of Applied Sciences and Engineering*, 11(3), pp. 209–219. <https://doi.org/10.1556/1848.2020.00055>
13. Al-Oran, O., Lezsovits, F., and Aljawabrah, A., (2020): Exergy and energy amelioration for parabolic trough collector using mono and hybrid nanofluids, *Journal of Thermal*

- Analysis and Calorimetry, 140(3), pp. 1579–1596. <https://doi.org/10.1007/s10973-020-09371-x>
14. Al-Rabeeah, A.Y., Seres, I., and Farkas, I., (2021): Experimental Investigation and Performance Evaluation of Parabolic Trough Solar Collector for Hot Water Generation, *Journal of Engineering Thermophysics*, 30(3), pp. 420–432. <https://doi.org/10.1134/S1810232821030073>
  15. Al-Rabeeah, A.Y., Seres, I., and Farkas, I., (2022): Recent Improvements of the Optical and Thermal Performance of the Parabolic Trough Solar Collector Systems, *Facta Universitatis, Series: Mechanical Engineering*, 20(1), pp. 73–94. <https://doi.org/10.22190/FUME201106030A>
  16. Al-Rabeeah, A.Y., Seres, I., and Farkas, I., (2022): Thermal Improvement in Parabolic Trough Solar Collector Using Receiver Tube Design and Nanofluid, in *Mechanisms and Machine Science*. Springer, pp. 30–40. [https://doi.org/10.1007/978-3-030-87383-7\\_4](https://doi.org/10.1007/978-3-030-87383-7_4)
  17. AL-Rjoub, A., Rebouta, L., Costa, P., Cunha, N. F., Lanceros-Mendez, S., Barradas, N. P., and Alves, E., (2019): The effect of increasing Si content in the absorber layers ( $\text{CrAlSiN}_x/\text{CrAlSiO}_y\text{N}_x$ ) of solar selective absorbers upon their selectivity and thermal stability, *Applied Surface Science*, 481, pp. 1096–1102. <https://doi.org/10.1016/j.apsusc.2019.03.208>
  18. AL-Rjoub, A., Rebouta, L., Costa, P., and Vieira, L.G., (2018): Multi-layer solar selective absorber coatings based on  $\text{W}/\text{WSiAlN}_x/\text{WSiAlO}_y\text{N}_x/\text{SiAlO}_x$  for high temperature applications, *Solar Energy Materials and Solar Cells*, 186, pp. 300–308. <https://doi.org/10.1016/j.solmat.2018.07.001>
  19. Alsaady, M., Fu, R., Yan, Y., Liu, Z., Wu, S., and Boukhanouf, R., (2019): An Experimental Investigation on the Effect of Ferrofluids on the Efficiency of Novel Parabolic Trough Solar Collector Under Laminar Flow Conditions, *Heat Transfer Engineering*, 40(9–10), pp. 753–761. <https://doi.org/10.1080/01457632.2018.1442309>
  20. Ambrosini, A., Lambert, T.N., Boubault, A., Hunt, A., Davis, D.J., Adams, D., and Hall, A.C., (2015): Thermal stability of oxide-based solar selective coatings for CSP central receivers, in *ASME 2015 9th International Conference on Energy Sustainability, ES 2015*, collocated with the ASME 2015 Power Conference, the ASME 2015 13th International Conference on Fuel Cell Science, Engineering and Technology, and the ASME 2015 Nuclear Forum. American Society of Mechanical Engineers Digital Collection. <https://doi.org/10.1115/ES2015-49706>
  21. Antonaia, A., Castaldo, A., Addonizio, M.L., and Esposito, S., (2010): Stability of  $\text{W-Al}_2\text{O}_3$  cermet based solar coating for receiver tube operating at high temperature, *Solar Energy Materials and Solar Cells*, 94(10), pp. 1604–1611. <https://doi.org/10.1016/j.solmat.2010.04.080>
  22. Atkinson, C., Sansom, C.L., Almond, H.J., and Shaw, C.P., (2015): Coatings for concentrating solar systems - A review, *Renewable and Sustainable Energy Reviews*, 45, 113–122. <https://doi.org/10.1016/j.rser.2015.01.015>
  23. Bader, R., Pedretti, A., Barbato, M., and Steinfeld, A., (2015): An air-based corrugated cavity-receiver for solar parabolic trough concentrators, *Applied Energy*, 138, pp. 337–345. <https://doi.org/10.1016/j.apenergy.2014.10.050>
  24. Bannerot, R.B., and Guven, H.M., (1984): Optical and thermal Analysis of Parabolic Trough Solar Collectors for technically Less Developed Countries, *Texas: Mechanical Engineering Department University of Houston*, 1–148
  25. Behar, O., Khellaf, A., and Mohammedi, K., (2015): A novel parabolic trough solar collector model - Validation with experimental data and comparison to Engineering Equation Solver (EES), *Energy Conversion and Management*, 106, pp. 268–281. <https://doi.org/10.1016/j.enconman.2015.09.045>

26. Bellos, E., Korres, D., Tzivanidis, C., and Antonopoulos, K.A., (2016): Design, simulation and optimization of a compound parabolic collector, *Sustainable Energy Technologies and Assessments*, 16, pp. 53–63. <https://doi.org/10.1016/j.seta.2016.04.005>
27. Bellos, E., and Tzivanidis, C., (2017): Parametric analysis and optimization of an Organic Rankine Cycle with nanofluid based solar parabolic trough collectors, *Renewable Energy*, 114, pp. 1376–1393. <https://doi.org/10.1016/j.renene.2017.06.055>
28. Bellos, E., and Tzivanidis, C., (2018): Enhancing the performance of evacuated and non-evacuated parabolic trough collectors using twisted tape inserts, perforated plate inserts and internally finned absorber, *Energies*, 11(5), 1129. <https://doi.org/10.3390/en11051129>
29. Bellos, E., and Tzivanidis, C., (2019): Alternative designs of parabolic trough solar collectors, *Progress in Energy and Combustion Science*, 71, pp. 81–117. <https://doi.org/10.1016/j.pecs.2018.11.001>
30. Bellos, E., Tzivanidis, C., Antonopoulos, K.A., and Gkinis, G., (2016): Thermal enhancement of solar parabolic trough collectors by using nanofluids and converging-diverging absorber tube, *Renewable Energy*, 94, pp. 213–222. <https://doi.org/10.1016/j.renene.2016.03.062>
31. Bellos, E., Tzivanidis, C., and Tsimpoukis, D., (2017): Thermal enhancement of parabolic trough collector with internally finned absorbers, *Solar Energy*, 157, pp. 514–531. <https://doi.org/10.1016/j.solener.2017.08.067>
32. Benoit, H., Spreafico, L., Gauthier, D., and Flamant, G., (2016): Review of heat transfer fluids in tube-receivers used in concentrating solar thermal systems: Properties and heat transfer coefficients, *Renewable and Sustainable Energy Reviews*, 55, pp. 298–315. <https://doi.org/10.1016/j.rser.2015.10.059>
33. Bermel, P., Lee, J., Joannopoulos, J.D., Celanovic, I., and Soljacic, M., (2012): Selective Solar Absorbers, *Annual Review of Heat Transfer*, 15(15), 231–254. <https://doi.org/10.1615/annualrevheattransfer.2012004119>
34. Birch, W. R. (2004): Cleaning Glass Surfaces, in *Sol-Gel Technologies for Glass Producers and Users*. Springer, pp. 19–34. [https://doi.org/10.1007/978-0-387-88953-5\\_2](https://doi.org/10.1007/978-0-387-88953-5_2)
35. Blasius, H. (1913): Das Aehnlichkeitsgesetz bei Reibungsvorgängen in Flüssigkeiten, in *Mitteilungen über Forschungsarbeiten auf dem Gebiete des Ingenieurwesens*. Springer, pp. 1–41. [https://doi.org/10.1007/978-3-662-02239-9\\_1](https://doi.org/10.1007/978-3-662-02239-9_1)
36. Braham, R.J., and Harris, A.T., (2009): Review of major design and scale-up considerations for solar photocatalytic reactors, *Industrial and Engineering Chemistry Research*, 48(19), pp. 8890–8905. <https://doi.org/10.1021/ie900859z>
37. Bretado de los Rios, M.S., Rivera-Solorio, C.I., and García-Cuéllar, A.J., (2018): Thermal performance of a parabolic trough linear collector using Al<sub>2</sub>O<sub>3</sub>/H<sub>2</sub>O nanofluids, *Renewable Energy*, 122, pp. 665–673. <https://doi.org/10.1016/j.renene.2018.01.094>
38. Brogren, M., Karlsson, B., Roos, A., and Werner, A., (2004): Analysis of the effects of outdoor and accelerated ageing on the optical properties of reflector materials for solar energy applications, *Solar Energy Materials and Solar Cells*, 82(4), 491–515. <https://doi.org/10.1016/j.solmat.2004.02.011>
39. Cao, F., McEnaney, K., Chen, G., and Ren, Z., (2014): A review of cermet-based spectrally selective solar absorbers, *Energy and Environmental Science*, 7(5), pp. 1615–1627. <https://doi.org/10.1039/c3ee43825b>
40. Cengel, Y.A., (2011): Ghajar, Heat and Mass Transfer-Fundamentals and applications. Mc Graw Hill, fourth edition
41. Cengel, Y.A., and Ghajar, A. J., (2011): Heat and mass transfer (a practical approach, SI version), McGraw-700 Hill Education, 701, 52

42. Céspedes, E., Wirz, M., Sánchez-García, J. A., Alvarez-Fraga, L., Escobar-Galindo, R., and Prieto, C., (2014): Novel Mo-Si<sub>3</sub>N<sub>4</sub> based selective coating for high temperature concentrating solar power applications, *Solar Energy Materials and Solar Cells*, 122, pp. 217–225. <https://doi.org/10.1016/j.solmat.2013.12.005>
43. Chafie, M., Ben Aissa, M.F., Bouadila, S., Balghouthi, M., Farhat, A., and Guizani, A., (2016): Experimental investigation of parabolic trough collector system under Tunisian climate: Design, manufacturing and performance assessment, *Applied Thermal Engineering*, 101, pp. 273–283. <https://doi.org/10.1016/j.applthermaleng.2016.02.073>
44. Chandrika, V.S., Attia, M.E. H., Manokar, A. M., Marquez, F.P.G., Driss, Z., and Sathyamurthy, R., (2021): Performance enhancements of conventional solar still using reflective aluminium foil sheet and reflective glass mirrors: energy and exergy analysis, *Environmental Science and Pollution Research*, 28(25), pp. 32508–32516. <https://doi.org/10.1007/s11356-021-13087-2>
45. Cheng, Z.D., He, Y.L., and Cui, F.Q., (2012): Numerical study of heat transfer enhancement by unilateral longitudinal vortex generators inside parabolic trough solar receivers, *International Journal of Heat and Mass Transfer*, 55(21–22), pp. 5631–5641. <https://doi.org/10.1016/j.ijheatmasstransfer.2012.05.057>
46. Cheng, Z.D., He, Y.L., Wang, K., Du, B.C., and Cui, F.Q., (2014): A detailed parameter study on the comprehensive characteristics and performance of a parabolic trough solar collector system, *Applied Thermal Engineering*, 63(1), pp. 278–289. <https://doi.org/10.1016/j.applthermaleng.2013.11.011>
47. Coccia, G., Di Nicola, G., Colla, L., Fedele, L., and Scattolini, M., (2016): Adoption of nanofluids in low-enthalpy parabolic trough solar collectors: Numerical simulation of the yearly yield, *Energy Conversion and Management*, 118, pp. 306–319. <https://doi.org/10.1016/j.enconman.2016.04.013>
48. Dan, A., Biswas, A., Sarkar, P., Kashyap, S., Chattopadhyay, K., Barshilia, H. C., and Basu, B., (2018): Enhancing spectrally selective response of W/WAIN/WAION/Al<sub>2</sub>O<sub>3</sub> – Based nanostructured multilayer absorber coating through graded optical constants, *Solar Energy Materials and Solar Cells*, 176, pp. 157–166. <https://doi.org/10.1016/j.solmat.2017.11.013>
49. Demagh, Y., Bordja, I., Kabar, Y., and Benmoussa, H., (2015): A design method of an S-curved parabolic trough collector absorber with a three-dimensional heat flux density distribution, *Solar Energy*, 122, pp. 873–884. <https://doi.org/10.1016/j.solener.2015.10.002>
50. Dimens, N., (2014): International Journal of Nano Dimension Numerical analysis of performance of solar parabolic trough collector with Cu-Water nanofluid, *International Journal of Nano Dimension*, 5(3), pp. 233–240
51. Duffie, J. A., Beckman, W. A., and McGowan, J., (1985): *Solar Engineering of Thermal Processes*, American Journal of Physics. USA, 382–382. <https://doi.org/10.1119/1.14178>
52. Eck, M., Feldhoff, J.F., and Uhlig, R., (2010): Thermal modelling and simulation of parabolic trough receiver tubes, in *ASME 2010 4th International Conference on Energy Sustainability, ES 2010*, pp. 659–666. <https://doi.org/10.1115/ES2010-90402>
53. Edenburn, M. W. (1976): Performance analysis of a cylindrical parabolic focusing collector and comparison with experimental results, *Solar Energy*, 18(5), pp. 437–444. [https://doi.org/10.1016/0038-092X\(76\)90010-4](https://doi.org/10.1016/0038-092X(76)90010-4)
54. Ehtiwesh, I.A. S., Neto Da Silva, F., and Sousa, A.C.M. (2019): Deployment of parabolic trough concentrated solar power plants in North Africa—a case study for Libya, *International Journal of Green Energy*, 16(1), pp. 72–85. <https://doi.org/10.1080/15435075.2018.1533474>



55. Esposito, S., D'Angelo, A., Antonaia, A., Castaldo, A., Ferrara, M., Addonizio, M. L., and Guglielmo, A., (2016): Optimization procedure and fabrication of highly efficient and thermally stable solar coating for receiver operating at high temperature, *Solar Energy Materials and Solar Cells*, 157, pp. 429–437. <https://doi.org/10.1016/j.solmat.2016.06.047>
56. Estellé, P., Halelfadl, S., and Maré, T., (2015): Thermal conductivity of CNT water based nanofluids: Experimental trends and models overview, *Journal of Thermal Engineering*, 1(2), pp. 381–390. <https://doi.org/10.18186/jte.92293>
57. Fernández-Abia, A.I., Barreiro, J., Fernández-Larrinoa, J., López de Lacalle, L.N., Fernández-Valdivielso, A., and Pereira, O.M., (2013): Behaviour of PVD coatings in the turning of austenitic stainless steels, *Procedia Engineering*, 63, pp. 133–141. <https://doi.org/10.1016/j.proeng.2013.08.241>
58. Fernández-García, A., Zarza, E., Valenzuela, L., and Pérez, M., (2010): Parabolic-trough solar collectors and their applications, *Renewable and Sustainable Energy Reviews*, 14(7), pp. 1695–1721. <https://doi.org/10.1016/j.rser.2010.03.012>
59. Ferraro, V., Settino, J., Cucumo, M.A., and Kaliakatsos, D., (2016): Parabolic Trough System Operating with Nanofluids: Comparison with the Conventional Working Fluids and Influence on the System Performance, *Energy Procedia*, 101, pp. 782–789. <https://doi.org/10.1016/j.egypro.2016.11.099>
60. Fuqiang, W., Ziming, C., Jianyu, T., Yuan, Y., Yong, S., and Linhua, L., (2017): Progress in concentrated solar power technology with parabolic trough collector system: A comprehensive review, *Renewable and Sustainable Energy Reviews*, 79, pp. 1314–1328. <https://doi.org/10.1016/j.rser.2017.05.174>
61. Gao, X. H., Qiu, X.L., Li, X.T., Theiss, W., Chen, B.H., Guo, H.X., Zhou, T.H., and Liu, G., (2019): Structure, thermal stability and optical simulation of ZrB<sub>2</sub> based spectrally selective solar absorber coatings, *Solar Energy Materials and Solar Cells*, 193, pp. 178–183. <https://doi.org/10.1016/j.solmat.2018.12.040>
62. Ghasemi, S.E., and Ranjbar, A.A., (2017): Effect of using nanofluids on efficiency of parabolic trough collectors in solar thermal electric power plants, *International Journal of Hydrogen Energy*, 42(34), pp. 21626–21634. <https://doi.org/10.1016/j.ijhydene.2017.07.087>
63. Günther, M., Joemann, M., and Csambor, S., (2011): *Advanced CSP Teaching Materials Chapter 5 Parabolic Trough Technology Authors*, 2011, pp. 1–43
64. Güven, H.M., and Bannerot, R.B., (1986): Derivation of universal error parameters for comprehensive optical analysis of parabolic troughs, *Journal of Solar Energy Engineering, Transactions of the ASME*, 108(4), pp. 275–281. <https://doi.org/10.1115/1.3268106>
65. Hachicha, A.A., Rodríguez, I., Capdevila, R., and Oliva, A., (2013): Heat transfer analysis and numerical simulation of a parabolic trough solar collector, *Applied Energy*, 111, pp. 581–592. <https://doi.org/10.1016/j.apenergy.2013.04.067>
66. He, Y.L., Xiao, J., Cheng, Z.D., and Tao, Y.B., (2011): A MCRT and FVM coupled simulation method for energy conversion process in parabolic trough solar collector, *Renewable Energy*, 36(3), pp. 976–985. <https://doi.org/10.1016/j.renene.2010.07.017>
67. Hermoso, J. L. N., and Sanz, N. M. (2015): Receiver Tube Performance Depending on Cleaning Methods, *Energy Procedia*, 69, pp. 1529–1539. <https://doi.org/10.1016/j.egypro.2015.03.104>
68. Hernández-Pinilla, D., Rodríguez-Palomo, A., Álvarez-Fraga, L., Céspedes, E., Prieto, J. E., Muñoz-Martín, A., and Prieto, C., (2016): MoSi<sub>2</sub>-Si<sub>3</sub>N<sub>4</sub> absorber for high temperature solar selective coating, *Solar Energy Materials and Solar Cells*, 152, pp. 141–146. <https://doi.org/10.1016/j.solmat.2016.04.001>

69. Heyhat, M.M., Valizade, M., Abdolazhade, S., and Maerefat, M., (2020): Thermal efficiency enhancement of direct absorption parabolic trough solar collector (DAPTSC) by using nanofluid and metal foam, *Energy*, 192, p. 116662. <https://doi.org/10.1016/j.energy.2019.116662>
70. Ho, C.K., and Iverson, B.D. (2014): Review of high-temperature central receiver designs for concentrating solar power, *Renewable and Sustainable Energy Reviews*, 29, pp. 835–846. <https://doi.org/10.1016/j.rser.2013.08.099>
71. Ho, C.K., Sims, C.A., and Christian, J.M., (2015): Evaluation of Glare at the Ivanpah Solar Electric Generating System, *Energy Procedia*, 69, pp. 1296–1305. <https://doi.org/10.1016/j.egypro.2015.03.150>
72. Huang, Z., Li, Z.Y., Yu, G.L., and Tao, W.Q., (2017): Numerical investigations on fully-developed mixed turbulent convection in dimpled parabolic trough receiver tubes, *Applied Thermal Engineering*, 114, pp. 1287–1299. <https://doi.org/10.1016/j.applthermaleng.2016.10.012>
73. Jaramillo, O.A., Borunda, M., Velazquez-Lucho, K.M., and Robles, M., (2016): Parabolic trough solar collector for low enthalpy processes: An analysis of the efficiency enhancement by using twisted tape inserts, *Renewable Energy*, 93, pp. 125–141. <https://doi.org/10.1016/j.renene.2016.02.046>
74. Jebasingh, V.K., and Herbert, G.M.J., (2016): A review of solar parabolic trough collector, *Renewable and Sustainable Energy Reviews*, 54, pp. 1085–1091. <https://doi.org/10.1016/j.rser.2015.10.043>
75. Jian-ping, M., Rui-rui, G., Li, H., Lu-ming, Z., Xiao-peng, L., and Zhou, L., (2018): Microstructure and thermal stability of Cu/Zr<sub>0.3</sub>Al<sub>10.7</sub>N/Zr<sub>0.2</sub>Al<sub>10.8</sub>N/ Al<sub>34</sub>O<sub>60</sub>N<sub>6</sub> cermet-based solar selective absorbing coatings, *Applied Surface Science*, 440, pp. 932–938
76. Kakaç, S., and Pramuanjaroenkij, A., (2016): Single-phase and two-phase treatments of convective heat transfer enhancement with nanofluids - A state-of-the-art review, *International Journal of Thermal Sciences*, 100, pp. 75–97. <https://doi.org/10.1016/j.ijthermalsci.2015.09.021>
77. Karas, D.E., Byun, J., Moon, J., and Jose, C., (2018): Copper-oxide spinel absorber coatings for high-temperature concentrated solar power systems, *Solar Energy Materials and Solar Cells*, 182, 321–330. <https://doi.org/10.1016/j.solmat.2018.03.025>
78. Kasaeian, A., Daneshazarian, R., and Pourfayaz, F., (2017): Comparative study of different nanofluids applied in a trough collector with glass-glass absorber tube, *Journal of Molecular Liquids*, 234, pp. 315–323. <https://doi.org/10.1016/j.molliq.2017.03.096>
79. Kasaeian, A., Daviran, S., Azarian, R. D., and Rashidi, A., (2015): Performance evaluation and nanofluid using capability study of a solar parabolic trough collector, *Energy Conversion and Management*, 89, pp. 368–375. <https://doi.org/10.1016/j.enconman.2014.09.056>
80. Kennedy, C.E., (2007): *Advances in concentrating solar power collectors: Mirrors and solar-selective coatings*, Association of Industrial Metallizers, Coaters and Laminators - Fall Technical Conf. of the Association of Industrial Metallizers, Coaters and Laminators 2007 and 21st Int. Vacuum Web Coating Conf. National Renewable Energy Lab. (NREL), Golden, CO (United States)
81. Kennedy, C.E., and Terwilliger, K., (2005a): Optical durability of candidate solar reflectors, *Journal of Solar Energy Engineering, Transactions of the ASME*, 127(2), pp. 262–269. <https://doi.org/10.1115/1.1861926>
82. Kennedy, C.E., and Terwilliger, K., (2005b): *Optical durability of candidate solar reflectors*, *Journal of Solar Energy Engineering, Transactions of the ASME*. National Renewable Energy Lab.(NREL), Golden, CO (United States).



- <https://doi.org/10.1115/1.1861926>
83. Khakrah, H., Shamloo, A., and Kazemzadeh Hannani, S., (2018): Exergy analysis of parabolic trough solar collectors using Al<sub>2</sub>O<sub>3</sub>/synthetic oil nanofluid, *Solar Energy*, 173, pp. 1236–1247. <https://doi.org/10.1016/j.solener.2018.08.064>
  84. Khan, J., and Arsalan, M. H., (2016): Solar power technologies for sustainable electricity generation - A review, *Renewable and Sustainable Energy Reviews*, 55, pp. 414–425. <https://doi.org/10.1016/j.rser.2015.10.135>
  85. Khan, M.A., and Kleine, T.O., (1977): *Histochemical and biochemical investigations of adenosine triphosphatase in vertebrate mixed muscles.*, Acta histochemica. Supplementband. National Renewable Energy Lab. (NREL), Golden, CO (United States). Available at: <http://www.nrel.gov/docs/fy09osti/45633.pdf>
  86. Khan, U., Zaib, A., and Mebarek-Oudina, F., (2020): Mixed Convective Magneto Flow of SiO<sub>2</sub>–MoS<sub>2</sub>/C<sub>2</sub>H<sub>6</sub>O<sub>2</sub> Hybrid Nanoliquids Through a Vertical Stretching/Shrinking Wedge: Stability Analysis, *Arabian Journal for Science and Engineering*, 45(11), pp. 9061–9073. <https://doi.org/10.1007/s13369-020-04680-7>
  87. Kotilainen, M., Honkanen, M., Mizohata, K., and Vuoristo, P. (2016): Influence of temperature-induced copper diffusion on degradation of selective chromium oxy-nitride solar absorber coatings, *Solar Energy Materials and Solar Cells*, 145, pp. 323–332. <https://doi.org/10.1016/j.solmat.2015.10.034>
  88. Kotilainen, M., and Vuoristo, P., (2016): Aluminium and tantalum nitride barriers against copper diffusion in solar absorbers, *Surface Engineering*, 32(8), pp. 615–623. <https://doi.org/10.1080/02670844.2015.1121314>
  89. Krüger, D., Pandian, Y., Hennecke, K., and Schmitz, M., (2008): Parabolic trough collector testing in the frame of the REACT project, *Desalination*, 220(1–3), pp. 612–618. <https://doi.org/10.1016/j.desal.2007.04.062>
  90. Krüger, M., Schmelzer, J., Smokovych, I., Lopez Barrilao, J., and Hasemann, G., (2019): Processing of Mo silicide powders as filler particles in polymer-derived ceramic coatings for Mo-Si-B substrates, *Powder Technology*, 352, pp. 381–385. <https://doi.org/10.1016/j.powtec.2019.04.082>
  91. Li, M., and Wang, L.L., (2006): Investigation of evacuated tube heated by solar trough concentrating system, *Energy Conversion and Management*, 47(20), pp. 3591–3601. <https://doi.org/10.1016/j.enconman.2006.03.003>
  92. Li, Z.Y., Huang, Z., and Tao, W.Q., (2016): Three-dimensional numerical study on fully-developed mixed laminar convection in parabolic trough solar receiver tube, *Energy*, 113, pp. 1288–1303. <https://doi.org/10.1016/j.energy.2016.07.148>
  93. Liu, H.D., Wan, Q., Lin, B.Z., Wang, L.L., Yang, X.F., Wang, R.Y., Gong, D.Q., Wang, Y.B., Ren, F., Chen, Y.M., Cheng, X.D., and Yang, B., (2014): The spectral properties and thermal stability of CrAlO-based solar selective absorbing nanocomposite coating, *Solar Energy Materials and Solar Cells*, 122, pp. 226–232. <https://doi.org/10.1016/j.solmat.2013.12.010>
  94. Malan, A., and Kumar, K.R., (2021): A comprehensive review on optical analysis of parabolic trough solar collector, *Sustainable Energy Technologies and Assessments*, 46, p. 101305
  95. Malekan, M., Khosravi, A., and Syri, S., (2019): Heat transfer modeling of a parabolic trough solar collector with working fluid of Fe<sub>3</sub>O<sub>4</sub> and CuO/Therminol 66 nanofluids under magnetic field, *Applied Thermal Engineering*, 163, 114435. <https://doi.org/10.1016/j.applthermaleng.2019.114435>
  96. Manikandan, G.K., Iniyar, S., and Goic, R., (2019): Enhancing the optical and thermal efficiency of a parabolic trough collector – A review, *Applied Energy*, 235, pp. 1524–1540. <https://doi.org/10.1016/j.apenergy.2018.11.048>

97. McCord, K.M., Klinglesmith, D.A., Jurgenson, C.A., Bakker, E.J., Schmill, Reed A., Schmill, Rodney A., Gartner, D., Jaramillo, A., Romero, K., Rael, A., and Lewis, J., (2009): Characterization of silver and aluminum custom mirror coatings for the MRO interferometric telescopes, in *Optical Materials and Structures Technologies IV*. International Society for Optics and Photonics, 74250V. <https://doi.org/10.1117/12.826044>
98. Mebarek-Oudina, F., Aissa, A., Mahanthesh, B., and Öztop, H.F., (2020): Heat transport of magnetized Newtonian nanoliquids in an annular space between porous vertical cylinders with discrete heat source, *International Communications in Heat and Mass Transfer*, 117, 104737. <https://doi.org/10.1016/j.icheatmasstransfer.2020.104737>
99. Menbari, A., Alemrajabi, A. A., and Rezaei, A., (2017): Experimental investigation of thermal performance for direct absorption solar parabolic trough collector (DASPTC) based on binary nanofluids, *Experimental Thermal and Fluid Science*, 80, pp. 218–227. <https://doi.org/10.1016/j.expthermflusci.2016.08.023>
100. Mills, D., (2004): Advances in solar thermal electricity technology, *Solar Energy*, 76(1–3), pp. 19–31. [https://doi.org/10.1016/S0038-092X\(03\)00102-6](https://doi.org/10.1016/S0038-092X(03)00102-6)
101. Mohammad Zadeh, P., Sokhansefat, T., Kasaeian, A. B., Kowsary, F., and Akbarzadeh, A. (2015): Hybrid optimization algorithm for thermal analysis in a solar parabolic trough collector based on nanofluid, *Energy*, 82, pp. 857–864. <https://doi.org/10.1016/j.energy.2015.01.096>
102. Mokheimer, E.M.A., Dabwan, Y.N., Habib, M.A., Said, S.A.M., and Al-Sulaiman, F.A., (2014): Techno-economic performance analysis of parabolic trough collector in Dhahran, Saudi Arabia, *Energy Conversion and Management*, 86, pp. 622–633. <https://doi.org/10.1016/j.enconman.2014.06.023>
103. Montesa, I.E.P., Beniteza, A.M., Chaveza, O.M., and Herrera, A.E.L., (2014): Design and construction of a parabolic trough solar collector for process heat production, *Energy Procedia*, 57, pp. 2149–2158. <https://doi.org/10.1016/j.egypro.2014.10.181>
104. Muñoz, J., and Abánades, A. (2011): Analysis of internal helically finned tubes for parabolic trough design by CFD tools, *Applied Energy*, 88(11), pp. 4139–4149. <https://doi.org/10.1016/j.apenergy.2011.04.026>
105. Mwesigye, A., Bello-Ochende, T., and Meyer, J.P., (2013): Numerical investigation of entropy generation in a parabolic trough receiver at different concentration ratios, *Energy*, 53, pp. 114–127. <https://doi.org/10.1016/j.energy.2013.03.006>
106. Mwesigye, A., Bello-Ochende, T., and Meyer, J.P., (2014): Heat transfer and thermodynamic performance of a parabolic trough receiver with centrally placed perforated plate inserts, *Applied Energy*, 136, pp. 989–1003. <https://doi.org/10.1016/j.apenergy.2014.03.037>
107. Mwesigye, A., Bello-Ochende, T., and Meyer, J.P., (2016): Heat transfer and entropy generation in a parabolic trough receiver with wall-detached twisted tape inserts, *International Journal of Thermal Sciences*, 99, pp. 238–257. <https://doi.org/10.1016/j.ijthermalsci.2015.08.015>
108. Mwesigye, A., and Meyer, J.P., (2017): Optimal thermal and thermodynamic performance of a solar parabolic trough receiver with different nanofluids and at different concentration ratios, *Applied Energy*, 193, pp. 393–413. <https://doi.org/10.1016/j.apenergy.2017.02.064>
109. Ning, Y., Wang, C., Wang, W., Tomasella, E., Sun, Y., Song, P., Hao, W., and Bousquet, A., (2020): Improvement of thermal stability of ZrSiON based solar selective absorbing coating, *Journal of Materiomics*, 6(4), pp. 760–767. <https://doi.org/10.1016/j.jmat.2020.06.006>
110. Noman, M., Wasim, A., Ali, M., Jahanzaib, M., Hussain, S., Ali, H. M.K., and Ali, H.M.,

- (2019): An investigation of a solar cooker with parabolic trough concentrator, *Case Studies in Thermal Engineering*, 14, 100436. <https://doi.org/10.1016/j.csite.2019.100436>
111. Noor, N., and Muneer, S., (2009): Concentrating Solar Power (CSP) and its prospect in Bangladesh, in *Proceedings of 1st International Conference on the Developments in Renewable Energy Technology, ICDRET 2009*. IEEE, pp. 69–73. <https://doi.org/10.1109/icdret.2009.5454207>
112. Norouzi, A.M., Siavashi, M., and Khaliji Oskouei, M.H., (2020): Efficiency enhancement of the parabolic trough solar collector using the rotating absorber tube and nanoparticles, *Renewable Energy*, 145, pp. 569–584. <https://doi.org/10.1016/j.renene.2019.06.027>
113. Notter, R.H., and Sleicher, C.A., (1972): A solution to the turbulent Graetz problem-III Fully developed and entry region heat transfer rates, *Chemical Engineering Science*, 27(11), pp. 2073–2093. [https://doi.org/10.1016/0009-2509\(72\)87065-9](https://doi.org/10.1016/0009-2509(72)87065-9)
114. Nuru, Z.Y., Arendse, C.J., Muller, T.F., Khamlich, S., and Maaza, M., (2014): Thermal stability of electron beam evaporated Al<sub>x</sub>O<sub>y</sub>/Pt/Al<sub>x</sub>O<sub>y</sub> multilayer solar absorber coatings, *Solar Energy Materials and Solar Cells*, 120(PART B), pp. 473–480. <https://doi.org/10.1016/j.solmat.2013.09.027>
115. Okonkwo, E.C., Essien, E.A., Akhayere, E., Abid, M., Kavaz, D., and Ratlamwala, T.A.H., (2018): Thermal performance analysis of a parabolic trough collector using water-based green-synthesized nanofluids, *Solar Energy*, 170, pp. 658–670. <https://doi.org/10.1016/j.solener.2018.06.012>
116. Okonkwo, E.C., Wole-Osho, I., Kavaz, D., Abid, M., and Al-Ansari, T., (2020): Thermodynamic evaluation and optimization of a flat plate collector operating with alumina and iron mono and hybrid nanofluids, *Sustainable Energy Technologies and Assessments*, 37, 100636. <https://doi.org/10.1016/j.seta.2020.100636>
117. Pak, B.C., and Cho, Y.I., (1998): Hydrodynamic and heat transfer study of dispersed fluids with submicron metallic oxide particles, *Experimental Heat Transfer*, 11(2), pp. 151–170. <https://doi.org/10.1080/08916159808946559>
118. Patil, R.G., Kale, D.M., Panse, S.V., and Joshi, J.B., (2014): Numerical study of heat loss from a non-evacuated receiver of a solar collector, *Energy Conversion and Management*, 78, pp. 617–626. <https://doi.org/10.1016/j.enconman.2013.11.034>
119. Patil, R.G., Panse, S.V., and Joshi, J.B., (2014): Optimization of non-evacuated receiver of solar collector having non-uniform temperature distribution for minimum heat loss, *Energy Conversion and Management*, 85, pp. 70–84. <https://doi.org/10.1016/j.enconman.2014.05.047>
120. Petukhov, B.S., (1970): Heat Transfer and Friction in Turbulent Pipe Flow with Variable Physical Properties, in *Advances in Heat Transfer*. Elsevier, pp. 503–564. [https://doi.org/10.1016/S0065-2717\(08\)70153-9](https://doi.org/10.1016/S0065-2717(08)70153-9)
121. Potenza, M., Milanese, M., Colangelo, G., and de Risi, A., (2017): Experimental investigation of transparent parabolic trough collector based on gas-phase nanofluid, *Applied Energy*, 203, pp. 560–570. <https://doi.org/10.1016/j.apenergy.2017.06.075>
122. Prasad, M.S., Mallikarjun, B., Ramakrishna, M., Joarder, J., Sobha, B., and Sakthivel, S., (2018): Zirconia nanoparticles embedded spinel selective absorber coating for high performance in open atmospheric condition, *Solar Energy Materials and Solar Cells*, 174, pp. 423–432. <https://doi.org/10.1016/j.solmat.2017.09.032>
123. Price, H., Lüpfer, E., Kearney, D., Zarza, E., Cohen, G., Gee, R., and Mahoney, R., (2002): Advances in parabolic trough solar power technology, *Journal of Solar Energy Engineering, Transactions of the ASME*, 124(2), pp. 109–125. <https://doi.org/10.1115/1.1467922>
124. Qiu, X.L., Gao, X.H., Zhou, T.H., Chen, B.H., Lu, J.Z., Guo, H.X., Li, X.T., and Liu, G., (2019): Structure, thermal stability and chromaticity investigation of TiB<sub>2</sub> based high

- temperature solar selective absorbing coatings, *Solar Energy*, 181, pp. 88–94. <https://doi.org/10.1016/j.solener.2019.01.068>
125. Qiu, Y., Li, M. J., He, Y.L., and Tao, W.Q., (2017): Thermal performance analysis of a parabolic trough solar collector using supercritical CO<sub>2</sub> as heat transfer fluid under non-uniform solar flux, *Applied Thermal Engineering*, 115, pp. 1255–1265. <https://doi.org/10.1016/j.applthermaleng.2016.09.044>
126. Ravi Kumar, K., and Reddy, K.S., (2009): Thermal analysis of solar parabolic trough with porous disc receiver, *Applied Energy*, 86(9), pp. 1804–1812. <https://doi.org/10.1016/j.apenergy.2008.11.007>
127. Razmmand, F., Mehdipour, R., and Mousavi, S.M., (2019): A numerical investigation on the effect of nanofluids on heat transfer of the solar parabolic trough collectors, *Applied Thermal Engineering*, 152, pp. 624–633. <https://doi.org/10.1016/j.applthermaleng.2019.02.118>
128. Reddy, K.S., Kumar, K. R., and Satyanarayana, G.V., (2008): Numerical investigation of energy-efficient receiver for solar parabolic trough concentrator, *Heat Transfer Engineering*, 29(11), pp. 961–972. <https://doi.org/10.1080/01457630802125757>
129. Reddy, K.S., Ravi Kumar, K., and Ajay, C.S., (2015): Experimental investigation of porous disc enhanced receiver for solar parabolic trough collector, *Renewable Energy*, 77, pp. 308–319. <https://doi.org/10.1016/j.renene.2014.12.016>
130. Rehan, M. A., Ali, M., Sheikh, N. A., Khalil, M. S., Chaudhary, G. Q., Rashid, T. ur, and Shehryar, M. (2018): Experimental performance analysis of low concentration ratio solar parabolic trough collectors with nanofluids in winter conditions, *Renewable Energy*, 118, pp. 742–751. <https://doi.org/10.1016/j.renene.2017.11.062>
131. Reoyo-Prats, R., Carling Plaza, A., Faugeroux, O., Claudet, B., Soum-Glaude, A., Hildebrandt, C., Binyamin, Y., Agüero, A., and Meißner, T., (2019): Accelerated aging of absorber coatings for CSP receivers under real high solar flux – Evolution of their optical properties, *Solar Energy Materials and Solar Cells*, 193, pp. 92–100. <https://doi.org/10.1016/j.solmat.2018.12.030>
132. Rodríguez-Palomo, A., Céspedes, E., Hernández-Pinilla, D., and Prieto, C., (2018): High-temperature air-stable solar selective coating based on MoSi<sub>2</sub>–Si<sub>3</sub>N<sub>4</sub> composite, *Solar Energy Materials and Solar Cells*, 174, pp. 50–55. <https://doi.org/10.1016/j.solmat.2017.08.021>
133. Rubin, E.B., Chen, Y., and Chen, R., (2019): Optical properties and thermal stability of Cu spinel oxide nanoparticle solar absorber coatings, *Solar Energy Materials and Solar Cells*, 195, pp. 81–88. <https://doi.org/10.1016/j.solmat.2019.02.032>
134. Safaei, M.R., Ahmadi, G., Goodarzi, M.S., Shadloo, M.S., Goshayeshi, H.R., and Dahari, M., (2016): Heat transfer and pressure drop in fully developed turbulent flows of graphene nanoplatelets-silver/water nanofluids, *Fluids*, 1(3), pp. 20. <https://doi.org/10.3390/fluids1030020>
135. Sahin, A.Z., Uddin, M.A., Yilbas, B.S., and Al-Sharafi, A., (2020): Performance enhancement of solar energy systems using nanofluids: An updated review, *Renewable Energy*, 145, pp. 1126–1148. <https://doi.org/10.1016/j.renene.2019.06.108>
136. Saito, T., Iba, R., Ono, S., Imada, G., and Yasui, K., (2019): Growth characteristics of ZnO thin films produced via catalytic reaction-assisted chemical vapor deposition, *Journal of Vacuum Science & Technology A*, 37(3), p. 030904. <https://doi.org/10.1116/1.5079526>
137. Sandá, A., Moya, S.L., and Valenzuela, L., (2019): Modelling and simulation tools for direct steam generation in parabolic-trough solar collectors: A review, *Renewable and Sustainable Energy Reviews*, 113, p. 109226. <https://doi.org/10.1016/j.rser.2019.06.033>
138. Sarbolookzadeh Harandi, S., Karimipour, A., Afrand, M., Akbari, M., and D’Orazio, A.,



- (2016): An experimental study on thermal conductivity of F-MWCNTs-Fe<sub>3</sub>O<sub>4</sub>/EG hybrid nanofluid: Effects of temperature and concentration, *International Communications in Heat and Mass Transfer*, 76, pp. 171–177. <https://doi.org/10.1016/j.icheatmasstransfer.2016.05.029>
139. Selvakumar, N., and Barshilia, H.C., (2012): Review of physical vapor deposited (PVD) spectrally selective coatings for mid- and high-temperature solar thermal applications, *Solar Energy Materials and Solar Cells*, 98, pp. 1–23. <https://doi.org/10.1016/j.solmat.2011.10.028>
140. Selvakumar, N., Barshilia, H.C., Rajam, K.S., and Biswas, A., (2010): Structure, optical properties and thermal stability of pulsed sputter deposited high temperature HfO<sub>x</sub>/Mo/HfO<sub>2</sub> solar selective absorbers, *Solar Energy Materials and Solar Cells*, 94(8), pp. 1412–1420. <https://doi.org/10.1016/j.solmat.2010.04.073>
141. Sharma, P., Guler, Z., and Jackson, N., (2021): Development and characterization of confocal sputtered piezoelectric zinc oxide thin film, *Vacuum*, 184, 109930. <https://doi.org/10.1016/j.vacuum.2020.109930>
142. Shiva Prasad, M., Chandra Sekhar Reddy, K., and Sakthivel, S. (2016): Development of cost efficient solar receiver tube with a novel tandem absorber system, *Applied Thermal Engineering*, 109, pp. 988–996. <https://doi.org/10.1016/j.applthermaleng.2016.05.163>
143. Subramani, J., Nagarajan, P. K., Mahian, O., and Sathyamurthy, R. (2018): Efficiency and heat transfer improvements in a parabolic trough solar collector using TiO<sub>2</sub> nanofluids under turbulent flow regime, *Renewable Energy*, 119, pp. 19–31. <https://doi.org/10.1016/j.renene.2017.11.079>
144. Sutter, F., Fernández-García, A., Heller, P., Anderson, K., Wilson, G., Schmücker, M., and Marvig, P., (2015): Durability Testing of Silvered-Glass Mirrors, *Energy Procedia*, 69, pp. 1568–1577. <https://doi.org/10.1016/j.egypro.2015.03.110>
145. Teixeira, V., Sousa, E., Costa, M. F., Nunes, C., Rosa, L., Carvalho, M. J., Collares-Pereira, M., Roman, E., and Gago, J. (2001): Spectrally selective composite coatings of Cr-Cr<sub>2</sub>O<sub>3</sub> and Mo-Al<sub>2</sub>O<sub>3</sub> for solar energy applications, *Thin Solid Films*, 392(2), pp. 320–326. [https://doi.org/10.1016/S0040-6090\(01\)01051-3](https://doi.org/10.1016/S0040-6090(01)01051-3)
146. Thuné-Boyle, I.C., Stygall, J.A., Keshtgar, M.R., and Newman, S.P., (2006): Do religious/spiritual coping strategies affect illness adjustment in patients with cancer? A systematic review of the literature, *Social Science and Medicine*, 63(1), pp. 151–164. <https://doi.org/10.1016/j.socscimed.2005.11.055>
147. Tian, Y., and Zhao, C.Y., (2013): A review of solar collectors and thermal energy storage in solar thermal applications, *Applied Energy*, 104, pp. 538–553. <https://doi.org/10.1016/j.apenergy.2012.11.051>
148. Toppin-Hector, A., and Singh, H., (2016): Development of a nano-heat transfer fluid carrying direct absorbing receiver for concentrating solar collectors, *International Journal of Low-Carbon Technologies*, 11(2), pp. 199–204. <https://doi.org/10.1093/ijlct/ctt072>
149. Tsai, T.K., Hsueh, S.J., and Fang, J.S., (2014): Optical properties of Al<sub>x</sub>O<sub>y</sub>/Ni/Al<sub>x</sub>O<sub>y</sub> multilayered absorber coatings prepared by reactive DC magnetron sputtering, *Journal of Electronic Materials*, 43(1), pp. 229–235. <https://doi.org/10.1007/s11664-013-2829-z>
150. Usmani, B., and Dixit, A., (2016): Spectrally selective response of ZrO<sub>x</sub>/ZrC-ZrN/Zr absorber-reflector tandem structures on stainless steel and copper substrates for high temperature solar thermal applications, *Solar Energy*, 134, pp. 353–365. <https://doi.org/10.1016/j.solener.2016.05.014>
151. Valleti, K., Krishna, D.M., Reddy, P.M., and Joshi, S.V., (2016): High temperature stable solar selective coatings by cathodic arc PVD for heat collecting elements, *Solar Energy Materials and Solar Cells*, 145, pp. 447–453. <https://doi.org/10.1016/j.solmat.2015.11.012>

152. Verma, V.K., (2017): Numerical Study of Porous Parabolic-Finned Receiver for Solar Parabolic-Trough Concentrator
153. Wang, F., Tan, J., Ma, L., and Wang, C., (2015): Effects of glass cover on heat flux distribution for tube receiver with parabolic trough collector system, *Energy Conversion and Management*, 90, pp. 47–52. <https://doi.org/10.1016/j.enconman.2014.11.004>
154. Wang, Q., Hu, M., Yang, H., Cao, J., Li, J., Su, Y., and Pei, G., (2019): Performance evaluation and analyses of novel parabolic trough evacuated collector tubes with spectrum-selective glass envelope, *Renewable Energy*, 138, pp. 793–804. <https://doi.org/10.1016/j.renene.2019.02.025>
155. Wang, X., Yu, X., Fu, S., Lee, E., Kekalo, K., and Liu, J., (2018): Design and optimization of nanoparticle-pigmented solar selective absorber coatings for high-temperature concentrating solar thermal systems, *Journal of Applied Physics*, 123(3), p. 33104. <https://doi.org/10.1063/1.5009252>
156. Wirz, M., Petit, J., Haselbacher, A., and Steinfeld, A., (2014): Potential improvements in the optical and thermal efficiencies of parabolic trough concentrators, *Solar Energy*, 107, pp. 398–414. <https://doi.org/10.1016/j.solener.2014.05.002>
157. Xiao, X., Zhang, P., Shao, D.D., and Li, M., (2014): Experimental and numerical heat transfer analysis of a V-cavity absorber for linear parabolic trough solar collector, *Energy Conversion and Management*, 86, pp. 49–59. <https://doi.org/10.1016/j.enconman.2014.05.001>
158. Xin, C., Peng, C., Xu, Y., and Wu, J., (2013): A novel route to prepare weather resistant, durable antireflective films for solar glass, *Solar Energy*, 93, pp. 121–126. <https://doi.org/10.1016/j.solener.2013.04.006>
159. Xu, C., Chen, Z., Li, M., Zhang, P., Ji, X., Luo, X., and Liu, J., (2014): Research on the compensation of the end loss effect for parabolic trough solar collectors, *Applied Energy*, 115, pp. 128–139. <https://doi.org/10.1016/j.apenergy.2013.11.003>
160. Xu, K., Du, M., Hao, L., Mi, J., Yu, Q., and Li, S., (2020): A review of high-temperature selective absorbing coatings for solar thermal applications, *Journal of Materiomics*, 6(1), pp. 167–182. <https://doi.org/10.1016/j.jmat.2019.12.012>
161. Xuan, Y., Li, Q., and Hu, W., (2003): Aggregation structure and thermal conductivity of nanofluids, *AIChE Journal*, 49(4), pp. 1038–1043. <https://doi.org/10.1002/aic.690490420>
162. Yilmaz, S., Riza Ozcalik, H., and Dincer, F., (2017): Modeling and designing of the solar thermal parabolic trough concentrator and its *environmental* effects, *Environmental Progress and Sustainable Energy*, 36(3), pp. 967–974. <https://doi.org/10.1002/ep.12536>
163. Yilmaz, İ. H., and Mwesigye, A., (2018): Modeling, simulation and performance analysis of parabolic trough solar collectors: A comprehensive review, *Applied Energy*, 225, pp. 135–174. <https://doi.org/10.1016/j.apenergy.2018.05.014>
164. Zaaoumi, A., Asbik, M., Hafs, H., Bah, A., and Alaoui, M., (2021): Thermal performance simulation analysis of solar field for parabolic trough collectors assigned for ambient conditions in Morocco, *Renewable Energy*, 163, pp. 1479–1494. <https://doi.org/10.1016/j.renene.2020.08.151>
165. Zhao, S., (2007): Spectrally Selective Solar Absorbing Coatings Prepared by dc Magnetron Sputtering, *Science and Technology. Acta Universitatis Upsaliensis*, 86
166. Zhu, G., Kearney, D., and Mehos, M., (2014): On characterization and measurement of average solar field mirror reflectance in utility-scale concentrating solar power plants, *Solar Energy*, 99, pp. 185–202. <https://doi.org/10.1016/j.solener.2013.11.009>
167. Zhu, G., Wendelin, T., Wagner, M.J., and Kutscher, C., (2014): History, current state, and future of linear Fresnel concentrating solar collectors, *Solar Energy*, 103, pp. 639–652. <https://doi.org/10.1016/j.solener.2013.05.021>

168. Zou, B., Yang, H., Yao, Y., and Jiang, Y., (2017): A detailed study on the effects of sunshape and incident angle on the optical performance of parabolic trough solar collectors, *Applied Thermal Engineering*, 126, pp. 81–91. <https://doi.org/10.1016/j.applthermaleng.2017.07.149>
169. Zou, C., Xie, W., and Shao, L., (2016): Functional multi-layer solar spectral selective absorbing coatings of AlCrSiN/AlCrSiON/AlCrO for high temperature applications, *Solar Energy Materials and Solar Cells*, pp. 153, 9–17. <https://doi.org/10.1016/j.solmat.2016.04.007>

**A2: Publications related to the dissertation***Refereed papers in foreign languages:*

1. **Al-Rabeeah Asaad Yasseen**, Farkas I., Seres I. (2019): Design and experimental investigation of parabolic trough solar collector, *Mechanical Engineering Letters*, Gödöllő, Hungary, 19, pp. 26-32., HU ISSN 2060-3789.
2. **Al-Rabeeah Asaad Yasseen**, Seres I., Farkas I. (2021): Experimental investigation and performance evaluation of parabolic trough solar collector for hot water generation, *Journal of Engineering Thermophysics*, 30(3), 420–432.  
<https://doi.org/10.1134/S1810232821030073> (IF: 2.038)
3. **Al-Rabeeah Asaad Yasseen**, Seres I., Farkas I. (2022): Recent improvements of the optical and thermal performance of the parabolic trough solar collector systems, *Facta Universitatis, Series: Mechanical Engineering*, 20(1), 73–94.  
<https://doi.org/10.22190/FUME201106030A> (Scopus: Q1, IF: 7.9)
4. **Al-Rabeeah Asaad Yasseen**, Seres I., Farkas I. (2022): Selective absorber coatings and technological advancements in performance enhancement for parabolic trough solar collector, *Journal of Thermal Science*, 31(6), 1990–2008.  
<https://doi.org/10.1007/s11630-022-1634-5> (Scopus: Q2, IF: 2.5)
5. **Al-Rabeeah Asaad Yasseen**, Seres I., Farkas I. (2022): Effects of concentration and temperature on the viscosity and thermal conductivity of graphene–Fe<sub>3</sub>O<sub>4</sub>/water Hybrid nanofluid and development of new correlation, *Journal of Engineering Thermophysics*, 31(2), 328–339. <https://doi.org/10.1134/S1810232822020138> (IF: 2.4)
6. **Al-Rabeeah Asaad Yasseen**, Seres I., Farkas I. (2023): Experimental investigation of improved parabolic trough solar collector thermal efficiency using novel receiver geometry design, *International Journal of Thermofluids*, p. 100344.  
<https://doi.org/10.1016/j.ijft.2023.100344> (Scopus: D1)
7. **Al-Rabeeah Asaad Yasseen**, Seres I., Farkas I. (2023): Experimental investigation of parabolic trough solar collector thermal efficiency enhanced with different absorber coatings, *International Journal of Thermofluids*, p. 100386.  
<https://doi.org/10.1016/j.ijft.2023.100386> (Scopus: D1)
8. **Al-Rabeeah Asaad Yasseen**, Seres I., Farkas I. (2023): Experimental investigation of parabolic trough solar collector thermal efficiency enhanced by different reflective materials, *Journal of Engineering Thermophysics*, Vol. 32 (3), pp. xx-xx. (IF: 2.4, accepted)
9. **Al-Rabeeah Asaad Yasseen**, Seres I., Farkas I. (2023): Experimental and numerical investigation of parabolic trough solar collector thermal efficiency enhanced by graphene–Fe<sub>3</sub>O<sub>4</sub>/water hybrid nanofluid, *International Journal of Thermofluids*, Vol. xx, No xx, pp. xx-xx., ISSN 2451-9049 (under review)

*International conference proceedings:*

10. **Al-Rabeeah Asaad Yasseen**, Seres I., Farkas I. (2022): Thermal improvement in parabolic trough solar collector using receiver tube design and nanofluid, in *Mechanisms and Machine Science*. Springer, 30–40. [https://doi.org/10.1007/978-3-030-87383-7\\_4](https://doi.org/10.1007/978-3-030-87383-7_4)



11. **Al-Rabeeah Asaad Yasseen**, Seres I., Farkas I. (2023): Performance enhancement of PTSC by using mono and hybrid nanofluids, FoITIC, Proceedings of the 3rd Faculty of Industrial Technology International Congress, Bandung, Indonesia, October 28-29, 2021. pp. 67-73., ISSN 2962-1798.

*International conference abstracts:*

12. **Al-Rabeeah Asaad Yasseen**, Farkas I., Seres I.: Modelling aspects of concentrating solar collectors, Book of Abstracts, 25th Workshop on Energy and Environment, Gödöllő, Hungary, November 28-29, 2019, p. 27., ISBN 978-963-9483-95-8.
13. **Al-Rabeeah Asaad Yasseen**, Farkas I., Seres I.: On thermal efficiency of parabolic trough solar collectors, Book of Abstracts, 19th International Workshop for Young Scientists BioPhys Spring 2020, May 19-21, 2020, Prague, Czech Rep., p. 33., ISBN 978-83-89969-64-4.
14. **Al-Rabeeah Asaad Yasseen**, Farkas I., Seres I.: Performance enhancement of PTSC by selective absorber coatings, Book of Abstracts, 26th Workshop on Energy and Environment, Gödöllő, Hungary, December 10-11, 2020, p.17., ISBN 978-963-269-928-8.
15. **Al-Rabeeah Asaad Yasseen**, Farkas I., Seres I.: Thermal enhancement in parabolic trough solar collector using receiver geometry design and nanofluids, Book of Abstracts, International Workshop for Young Scientists BioPhys Spring 18th May 2021, Lublin, Poland, p.x., ISBN 978-83-89969-68-2.
16. **Al-Rabeeah Asaad Yasseen**, Farkas I., Seres I.: Enhancement of thermal efficiency of PTSC by using nanofluid, Book of Abstracts, 27th Workshop on Energy and Environment, Gödöllő, Hungary, December 9-10, 2021, p.11., ISBN 978-963-269-972-1.
17. **Al-Rabeeah Asaad Yasseen**, Farkas I., Seres I.: Heat transfer enhancement of PTSC by using Fe<sub>3</sub>O<sub>4</sub>/water nanofluid, Book of Abstracts, 28th Workshop on Energy and Environment, Gödöllő, Hungary, December 8-9, 2022, p.17-18., ISBN 978-963-623-016-6.
18. **Al-Rabeeah Asaad Yasseen**, Farkas I., Seres I.: Heat transfer enhancement of PTSC by using passive methods, Book of Abstracts, International Workshop for Young Scientists BioPhys Spring 16th June 2023, Gödöllő, Hungary, p.16, ISBN 978-963-623-053-1.

## 9. ACKNOWLEDGEMENTS

The successful completion of any task cannot be achieved without acknowledging the people who made it possible and whose constant guidance and encouragement secured the success.

First of all, I wish to acknowledge the benevolence of an omnipotent God who gave me strength and courage to overcome all obstacles and showed me the silver lining in the dark clouds.

I would like to thank the Stipendium Hungaricum Scholarship Program and the Mechanical Engineering Doctoral School at the Hungarian University of Agriculture and Life Sciences (MATE), Gödöllő, Hungary.

I am grateful to Prof. Farkas for his encouragement and support, which have provided me with an excellent atmosphere for doing research.

I would like to thank Dr. Seres for his support, feedback, encouragement, and immense knowledge.

I want to thank everyone in the Institute of Mechanical Engineering workshop for all the help and support they have given me.

My thanks also to my colleagues in the Mechanical Engineering Doctoral School, who are not mentioned here but helped me in completing this work.

I am deeply indebted to my wife and family for their help, endless encouragement, and prayers all through the formative years of my educational career.

August, 2023

Asaad Yasseen